1-2011

Direct Forcing and Heating Immersed Boundary- Lattice Boltzmann Method for Arterial Wall Thermography

Oluyinka Olugbenga Bamiro
Western Michigan University

Recommended Citation

Bamiro, Oluyinka Olugbenga, "Direct Forcing and Heating Immersed Boundary- Lattice Boltzmann Method for Arterial Wall Thermography" (2011). *Dissertations*. 345.
https://scholarworks.wmich.edu/dissertations/345

A DIRECT FORCING AND HEATING IMMERSED BOUNDARY- LATTICE BOLTZMANN METHOD FOR ARTERIAL WALL THERMOGRAPHY

by

Oluyinka Olugbenga Bamiro

A Dissertation
Submitted to the
Faculty of The Graduate College
in partial fulfillment of the
requirements for the
Degree of Doctor of Philosophy
Department of Mechanical and Aeronautical Engineering
Advisor: Dr. William Liou

Western Michigan University
Kalamazoo, Michigan
December 2011

A DIRECT FORCING AND HEATING IMMERSED BOUNDARY - LATTICE BOLTZMANN METHOD FOR ARTERIAL WALLL THERMOGRAPHY

Oluyinka Olugbenga Bamiro, Ph.D.

Western Michigan University, 2011

Vulnerable atherosclerotic plaques have high probability of rupture and are characterized by non-homogenous temperature along the arterial wall. The non-homogeneous temperature is attributed to the accumulation of heat releasing inflammatory cells in the arterial wall. Rupture of the vulnerable plaque can lead to acute coronary syndrome and sudden cardiac death. Arterial wall thermography (AWT) can be applied to detect the presence of temperature hot spots along the arterial wall by using temperature measurement devices and provide an early detection of a vulnerable atherosclerotic plaque. AWT, however, is invasive in nature.

Computational fluid and heat transport models provide a more efficient and non-intrusive approach to examine the effect of plaque geometry and blood flow parameters on the thermal profile than in-vitro and in-vivo methods. A new thermal immersed boundary method is developed based on the thermal lattice Boltzmann method for the computational simulations of incompressible flows with heat transfer. The new approach is called direct forcing and heating immersed boundary lattice Boltzmann method (IB-LBM). A new and easier method of implementing the Neumann

boundary condition and calculation of the local Nusselt number within the immersed boundary method computational framework was proposed and implemented. The new approach was validated with classical benchmark cases for natural convection and forced convection with Dirichlet and Neumann boundary conditions, there was good agreement between the results obtained using the proposed approach and published results in literature.

The proposed direct forcing and heating IB-LBM was then applied to study the effects of blood flow parameters, plaque geometry (macrophage cell density and fibrous cap thickness), macrophage heat generation rate and arterial lumen stenosis on the surface temperature profile of a vulnerable atherosclerotic plaque.

ProQuest LLC.
789 East Eisenhower Parkway
P.O. Box 1346
Ann Arbor, MI 48106 - 1346

ACKNOWLEDGMENTS

I am grateful to my thesis advisor and committee chair, Dr. William Liou who has provided me with thoughtful guidance and professional assistance during the course of my doctoral studies. I would also like to thank each of my committee members, Dr. Parviz Merati, Dr. Tianshu Liu of Western Michigan University and Dr. May-Fun Liou of NASA Glenn Research Center for their interest and help during the course of my research.

I would also express my profound gratitude to my parents for instilling in me at a young age the virtues of hard work, perseverance and patience which has tremendously helped me during my doctoral studies.

Finally, I would like to express my sincerest gratitude to my lovely wife Yemisi who has been there to support me and take care of the children while I was absent. This accomplishment and journey would have not being possible without you. I am thankful to my children, Oluwatobi and Toluwani for their support and encouragement. Above all I am thankful to the Almighty God for giving me and my family good health and his good blessings throughout my doctoral studies. I dedicate this thesis to my wife Yemisi for your unfailing love and support.

Oluyinka Olugbenga Bamiro

TABLE OF CONTENTS

CHAPTER

Table of Contents—continued

CHAPTER

Table of Contents—continued

CHAPTER

Table of Contents—continued

CHAPTER

LIST OF TABLES

LIST OF FIGURES

List of Figures—continued

List of Figures—continued

List of Figures—continued

List of Figures—continued

NOMENCLATURE

C_d	drag coefficient
C_L	lift coefficient
c_p	specific heat capacity
c_s	lattice speed of sound
D	characteristic length scale
dx	fluid grid spacing
ds	solid grid spacing
e	magnitude of the particle speed
$\mathbf{e}_i$	particle speed
$f_i(\mathbf{x},t)$	momentum particle distribution function
$f_i^{eq}(\mathbf{x},t)$	momentum equilibrium distribution function
$\mathbf{f}(\mathbf{X},t)$	force density at Lagrangian solid nodes
F_i	force density in the ith lattice direction
$\mathbf{F}(\mathbf{x},t)$	force density at Eulerian fluid nodes
$\mathbf{g}$	gravity vector
$h_i(\mathbf{x},t)$	temperature particle distribution function
$h_i^{eq}(\mathbf{x},t)$	temperature equilibrium distribution function
$h(\mathbf{X},t)$	heat density at Lagrangian solid nodes
H_i	heat density in the ith lattice direction
$H(\mathbf{x},t)$	heat density at Eulerian fluid nodes
Kn	Knudsen number
L	characteristic length scale
LU	lattice units
Nu	average Nusselt number
Nu_l	local Nusselt number
P	pressure
$\Pr$	Prandtl number
PU	physical units
q''	surface heat flux
q'''	macrophage layer metabolic or volumetric heat generation rate
Ra	Rayleigh number
Re	Reynolds number
St	Strouhal number

Nomenclature—continued

T	fluid temperature
T_b	immersed solid temperature
$\mathbf{u}$	fluid velocity
$\mathbf{U}_b$	immersed solid velocity
$\mathbf{x}$	position vector of fluid nodes
$\mathbf{X}$	position vector of solid nodes

α	thermal diffusivity
β	coefficient of thermal expansion
$\gamma(\mathbf{X},t)$	local heat transfer coefficient
$\delta(\mathbf{x}-\mathbf{X})$	discrete dirac delta function
κ	thermal conductivity
ν	kinematic viscosity
σ	accommodation coefficient
τ_f	momentum relaxation factor
τ_h	thermal relaxation factor
ρ	density
ω_i	LBM lattice weighting coefficients
Δt	lattice time step
Φ_h	dimensionless fibrous cap thickness
Φ_s	dimensionless arterial lumen stenosis severity
Φ_v	dimensionless macrophage cell density
Ω	collision operator

CHAPTER 1

INTRODUCTION

Cardiovascular disease (CVD) is the major cause of death in developed countries. Statistics have shown that among the 58 million deaths in the world in 2005, CVD was responsible for approximately 30% of all deaths or about 17.5 million people (World Health Organization, 2006). In the United States (US), CVD is the number one killer of both male and female accounting for approximately 2,400 deaths each day in US which is approximately an average of one death every 37 seconds (Rosamond et al. 2007). Researchers have also shown that about 60% of myocardial infarction (MI) and sudden deaths are caused by the plaque disruption or rupture of a vulnerable plaque (Casscells et al. 2003 and Falk et al. 1995). The vulnerable plaque can exhibit symptomatic or asymptomatic behavior in patients. When vulnerable plaques exhibit symptomatic behavior, there are signs and symptoms that show abnormal physiological behavior such as stenosis (narrowing of the arterial lumen), thus can easily be diagnosed by medical practitioners. On the other hand, the asymptomatic vulnerable plaques are dangerous and deadly because it is not easily detected. The first acute manifestation or symptoms for asymptomatic vulnerable plaques are myocardial infarction, sudden cardiac death or a disabling stroke (Alawi et al. 2010). Researchers have also showed that two thirds of patients with acute coronary events due to asymptomatic vulnerable plaque had minimal stenosis (less than 50% reduction in lumen diameter) based on coronary angiography weeks or months prior to the coronary event (Alawi et al. 2010). Stress tests which aid in detecting haemodynamically important or culprit stenosis were not adequate enough to detect the outcome of cardiac events due to asymptomatic vulnerable plaques (Naqvi et al. 1997). In other words, the degree of arterial lumen stenosis which has been the hallmark of diagnosing a patient disposition to CVD is not sufficient but rather other methods have to be sought in order to diagnose a vulnerable plaque. Arterial wall thermography belongs to the class of methods that can be used to diagnose a vulnerable plaque. In the next sections, the concepts of the vulnerable plaque and its relation to arterial wall thermography will be described and the motivation and research objective of the current study will also be addressed.

1.1 Arterial Wall Structure and Composition

The arteries are vessels of the cardiovascular system that transports oxygenated and nutrient rich blood from the heart to other organs of the body. Arteries can be broadly categorized into systemic or pulmonary arteries. Systemic arteries carry oxygenated blood from the heart to other organs of the body while pulmonary artery carries low oxygenated blood to the lungs (Khakpour et al. 2008). The largest of all arteries is the aorta from which stems out other systemic arteries. Examples of systemic arteries are the carotid, subclavian and brachial, iliac and femoral, coronary that supplies the head, arms, legs and the heart with oxygenated blood. Arteries vary in size depending on their location away from the heart. Arteries that are further away from the heart are smaller in diameter and wall thickness, wall thickness to diameter ratio increases and are less elastic compared to arteries that are closer to the heart (Kalita et al. 2008). Large sized arteries have internal diameters that ranges from 4mm to 5mm, medium sized arteries have internal diameter with ranges from 2.5mm to 4mm while smaller arteries have internal diameter that ranges from 1mm to 2.5mm. The aorta which is the largest systemic artery has internal diameter of 1cm to 3cm while the smallest systemic vessels the arterioles have inner diameter of 10μm to 25μm (Solomon et al. 1990).

The structure of the arterial wall is shown in Figure 1.1 (Holzapfel et al. 2000). The arterial wall is a multilayered structure consisting of three major layers namely the intima, media and adventitia. In terms of composition the arterial wall is composed of elastin, collagen, smooth muscle cell and ground substance matrix.

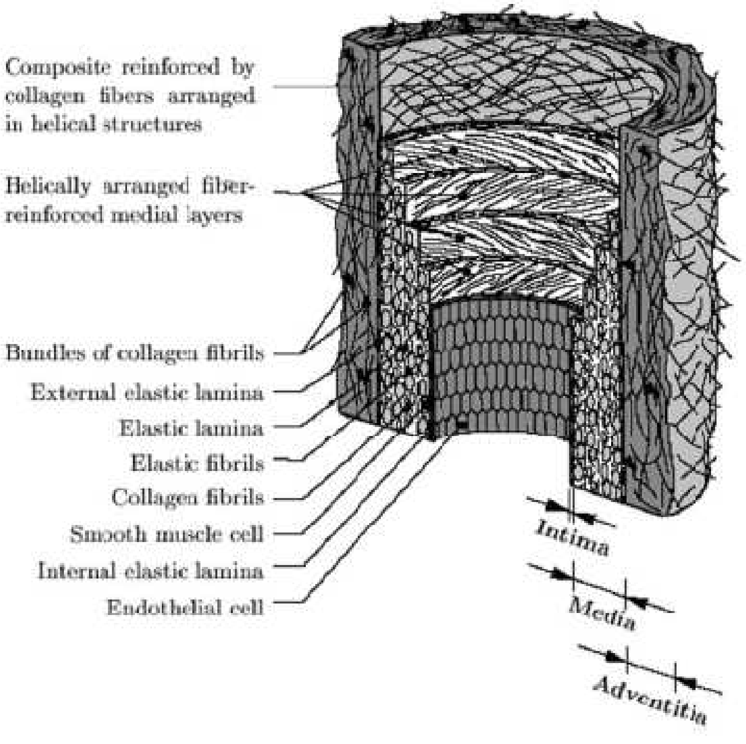

Figure 1.1 Schematic of the structure of an arterial wall (Holzapfel et al. 2000).

The intima is separated from the arterial lumen where blood flows by a thin membrane called endothelium which consists of endothelial cells. The endothelium performs selective filtration and control of nutrients and substances such as proteins, lipids and leukocytes (white blood cells) from the blood into wall. The intima is composed mainly of collagen fibers (Kalita et al. 2008). The internal elastic membrane separates the intima from the media. The media is the largest portion of the arterial wall structure and its material composition varies depending on its location. In muscular arteries, the media is composed of mainly smooth muscle cell. In elastic arteries, the media consists of elastin that is surrounded by smooth muscle cells and collagen that is embedded in ground substance. The media is responsible for majority of the elastic properties of the arterial wall. The external elastic membrane separates the media from the adventitia. The adventitia consists of collagen fibers that are embedded in the ground matrix substance. The adventitia contains lymphatic and vasa vasorum which supplies oxygen and nutrients to the tissues of the wall. The adventitia also provides the function of protecting the artery wall and embedding it in the surrounding connective tissues.

1.2 Atherosclerosis – A Disease of the Arterial Wall

Atherosclerosis is a lesion that occurs in medium and large sized arterial walls which is evidenced by the abnormal thickening of the arterial wall due to accumulation of macromolecules such as lipoproteins (LDL) and monocytes in the intima. The deposition of the fatty substances and macromolecules leads to plaque formation on the arterial wall. They are caused by the dysfunction of the endothelial cells (alteration of the permeability) of the endothelium, the endothelium as mentioned in the previous section is the membrane that regulates the selective filtration and control of nutrients and metabolites into the arterial wall from the blood. The endothelial dysfunction occurs in arterial areas where there are blood flow separation and recirculation zones with low hemodynamic shear stress. These hemodynamic effects are typically localized in regions with sudden change of geometry such as bifurcations or inner bends of artery (Ethier 2002) .

The American Heart Association categorized the atherosclerotic plaque based on histological and sequence of progression of the lesions (Stary et al. 1995). The classification of the plaque starts from Type I to Type VI. The Type I classification is the initial stages of the plaque and is characterized by the accumulation of macrophage foam cells. The infiltrated monocytes are transformed into macrophages or inflamed cells, the inflamed cells engulf the LDL to form foam cells at this stage.

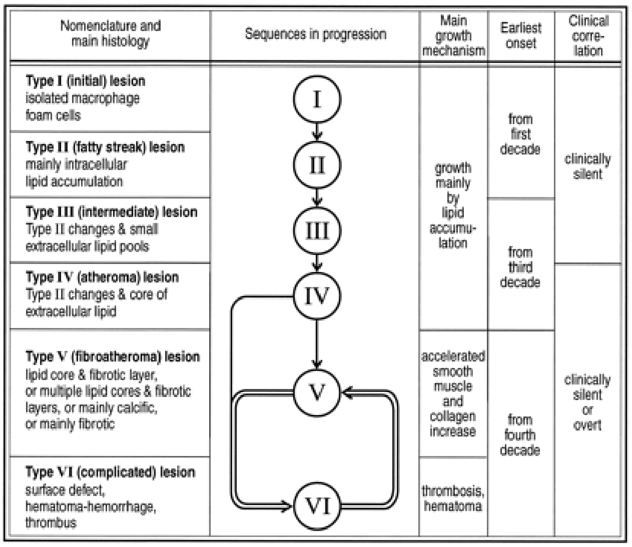

Nomenclature and main histology	Sequences in progression	Main growth mechanism	Earliest onset	Clinical corre-lation
Type I (initial) lesion isolated macrophage foam cells	I	growth mainly by lipid accumu-lation	from first decade	clinically silent
Type II (fatty streak) lesion mainly intracellular lipid accumulation	II			
Type III (intermediate) lesion Type II changes & small extracellular lipid pools	III		from third decade	
Type IV (atheroma) lesion Type II changes & core of extracellular lipid	IV			clinically silent or overt
Type V (fibroatheroma) lesion lipid core & fibrotic layer, or multiple lipid cores & fibrotic layers, or mainly calcific, or mainly fibrotic	V	accelerated smooth muscle and collagen increase	from fourth decade	
Type VI (complicated) lesion surface defect, hematoma-hemorrhage, thrombus	VI	thrombosis, hematoma		

Figure 1.2 Atherosclerotic plaque classification and progression (Stacy et al. 1995).

Intima thickening begins to occur at Type II plaque as evidenced by fatty streak due to lipid accumulation. Type III plaque is an intermediate stage between atheroma type plaques (Type IV). The atheroma type lesions are symptomatic lesions (that is lesions that produces symptoms). The progression from Type II to Type IV plaques are mainly through lipid accumulation in the arterial wall (Stacy et al. 1995). Types IV-VI was categorized as histological advanced lesions (Stacy et al. 1995). Advanced lesions are lesions that affect the structural composition or organization and shape of the arterial wall due to accumulation of lipids and fibrous cells. The advanced lesion compromises the structural integrity of the arterial wall by replacing them the parent material composition with lipid cores or fibrous cells. The advanced lesions might not cause stenosis and can be asymptomatic despite its clinical importance (Stacy et al. 1995).

Type IV lesion is characterized by disorganization of the arterial wall structure by the formation of large extracellular lipid cores. The extracellular lipid core displaces the intima smooth muscle cells from their parent location. Type V lesions are characterized by the formation of fibrous connective tissues or fibrous cap over a necrotic core. The Type V can be further subdivided based on the material composition of the necrotic core, Type Va for lipid necrotic core, Type Vb and Vc for calcified necrotic and fibrous necrotic cores. Type VI plaques are plaques with thrombus, hemorrhage or surface defects.

1.3 What is a Vulnerable Plaque?

The term vulnerable plaque was introduced by Muller et al. 1989 when studying the triggers of acute CVD. The vulnerable plaque was then defined as plaques that are susceptible to rupture and in the event of rupture causes acute thrombosis which eventually leads to total arterial lumen occlusion. The definition for vulnerable plaques have been expanding since then and there is currently no standard definition agreed or associated with vulnerable plaque among researchers and medical practitioners (Alawi et al. 2010). However there are widely accepted biomarkers or physiological features associated with a vulnerable plaque. Among the biomarkers or physiological features of vulnerable plaques are large lipid cores, thin fibrous caps and high concentration of macrophages (Virmani et al 2006; Narula et al. 2008 and Kolodgie et al. 2004). Type IV to Type VI or advanced type plaques belong to the category of plaques that can be vulnerable. The thin fibrous cap atheroma of a vulnerable plaque can be ruptured due to due to the local action of the wall shear stress. The rupture of the vulnerable plaque releases highly thrombogenic lipid pool into the blood stream. In the event of this can lead to thrombosis and arterial lumen occlusion resulting in a cardiac event such as cardiac death.

1.3.1 Methods of Detecting Vulnerable Plaque

The physiological features or biomarkers of vulnerable plaques have been used to detect its presence using imaging or thermography techniques. The methods can be invasive or non-invasive in nature. The biomarkers or physiological features that are used are fibrous cap thickness, presence of lipid core or calcium, evidence of thrombosis or inflammation. The most commonly used invasive imaging methods are X-ray angiography, intravascular ultrasound (IVUS), intracoronary angioscopy (IA), optical coherence tomography (OCT), Raman spectroscopy (RS) and near-infrared spectroscopy(NIS). Common non-invasive imaging methods are magnetic resonance imaging (MRI).

X- ray angiography helps in determining the degree of stenosis of the arterial lumen but does not provide information about the constituents or composition of the atherosclerotic plaque. IVUS based methods uses high frequency sounds to determine the composition of the vulnerable plaque. The different constituents of a vulnerable plaque reflect sound waves to varying degree. IVUS can determine the presence of calcium, fibrosis or lipid region based on the reflection of sound waves. A highly echo reflective sound wave at a region signifies the presence of calcium or calcified tissues, hyper echoic regions signifies the presence of fibrotic region while a hypo echoic region signifies the presence of lipid core region. Other variant of IVUS is the IVUS elastography where IVUS is combined intraluminal pressure readings in order to access the mechanical strength and strains of the walls in addition to material composition. IVUS has the limitation of parasitic reflection from neighboring or surrounding tissues. IA uses optical methods (white light) to map out the color of the arterial wall. IA can resolve colors into red/white, yellow and white regions. The red/white color signifies the presence of thrombus, yellow color signifies presence of lipid rich regions while white regions represent lipid poor regions. The major limitation of IA is that blood flow has to be temporarily stopped during its use. OCT is similar to IVUS but uses the intensity of reflected infrared light. The polarization characteristic of the reflected light can be used to differentiate the arterial composition. Reflected light from regions with high birefringence signifies areas with fibrous and lipid rich areas while regions with low birefringence represent regions with presence of calcium. OCT has a spatial resolution of

10 μm to 30 μm. The limitation of OCT is the reduction in image quality when acquiring images through blood. RS and NIS based methods uses Raman and near infrared spectroscopy to determine the chemical composition of the vulnerable plaque. Thermography based methods uses the non-uniformity of arterial wall temperature when vulnerable plaques are present to detect the presence of a vulnerable plaque. Thermography based methods are called Arterial Wall Thermography (AWT) and will be discussed further in the next section.

1.4 Arterial Wall Thermography

The vulnerable plaque as mentioned previously is characterized by a high concentration of inflamed cells or macrophages. The macrophages have a high metabolic rate that results in heat production. The heat production by the active macrophages results in non-uniform or abnormal temperature distribution along the arterial wall (Nemirovsky 2003 and Casscells et al. 1996). The ischemic event (lack of oxygen) in atherosclerotic plaques further exacerbates the heat production by macrophages since there is inefficiency in nutrient metabolism, energy is wasted and released in terms of heat as opposed to ATP production in normal tissues (Toutouzas et al. 2010). In addition to heat production, the macrophages secrete cytokines, the cytokines promotes production of chemicals (reactive oxygen species and proteolytic enzymes) that negatively affects the stability of the plaque.

Arterial wall thermography (AWT) based methods uses temperature measurement devices to determine temperature hot spots or non-homogeneity at the arterial wall of a vulnerable plaque with heat releasing macrophages or inflamed cells

(Casscells et al. 1996). AWT was first proposed by Casscells et al. 1996 where they used a thermistor to correlate temperature difference (relative to normal blood temperature) to macrophage cell density and the fibrous cap thickness in a carotid artery plaque. The temperature reading correlated positively with the macrophage cell density and negatively with the fibrous cap thickness (Casscells et al. 1996). A temperature difference of about 2.2°C was recorded. After the pioneering effort of Casscells et al. 1996, several in-vivo AWT measurements have been taken to detect the presence of vulnerable plaques (Stefanadis et al. 2001; Stefanadis 1999 and Cuisset et al. 2009).

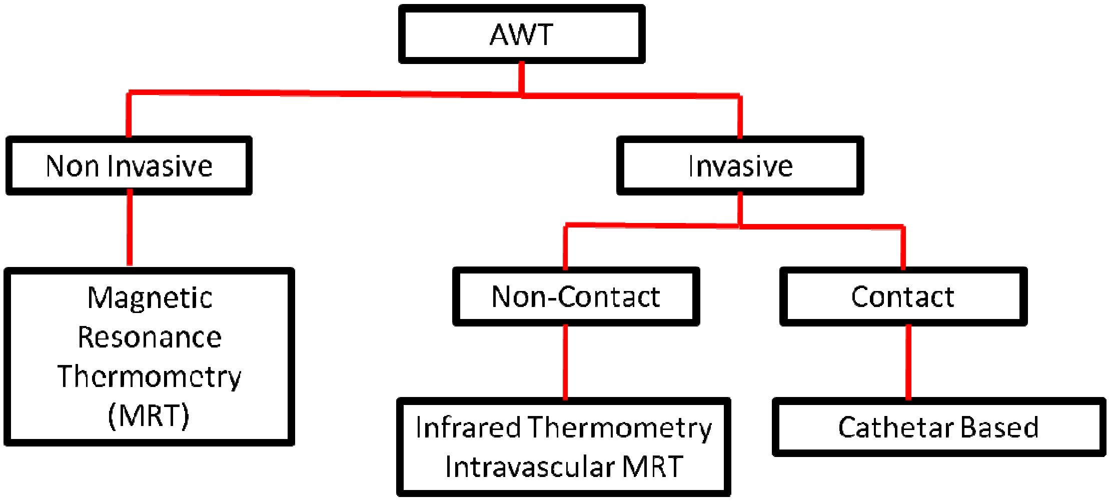

Figure 1.3 Classification of arterial wall thermography (AWT) techniques.

AWT techniques can be categorized into invasive and non-invasive methods as shown in Figure 1.3. The non-invasive methods use magnetic resonance thermometry (MRT) for evaluating the temperature profile of the arterial lumen. MRT have been widely used at the organ or tissue level by medical practitioners with success for imaging temperature distribution in 3D for organs such as brain and liver (Diamantopoulos 2003). MRT lacks the spatial resolution when applied to smaller organs or blood vessels however the limitation is less severe for larger arteries such as the aorta (Diamantopoulos, 2003). The major appeal of MRT is its non-invasiveness. Invasive methods can be contact or non-contact based. Non contact based method uses catheter based infrared sensor to map out the arterial wall temperature profile. The constituents of blood typically scatter IR radiation thereby limiting practical application of IR based methods (Diamantopoulos 2003). One way of circumventing this is limitation is to temporarily remove blood from the area of interest but this can be risky for the patient and also gives spurious temperature readings. The contact based methods requires direct contact of the temperature sensor with the arterial wall. The temperature sensors are catheter based and can either be an array of thermocouples or thermistor based. Thermocouples convert temperature measurements to electrical signals without the requirement for a power input. The generated electrical signal of the thermocouple is then correlated to temperature measurements. On the other hand, thermistor requires power input and the change in its electrical resistance is correlated to temperature measurements. In order to have a three dimensional thermal profile, the sensors must be able to obtain temperature readings circumferential and axial directions. The 3D thermal profile is then reconstructed from the circumferential and axial temperature readings using computational algorithms and interpolation. Figure 1.4 shows a practical application of a thermocouple based basket catheter used for AWT by Naghavi et al. 2003. The basket catheter consists of four expandable nitinol wires with thermocouples placed at the maximum curve of the nitinol wire. Figure 1.4a shows the expandable state of the basket, at the expandable state circumferential temperature readings can be obtained at the arterial wall. In order to move the basket catheter to the next axial location for sampling, the catheter is collapsed to the state shown in Figure 1.4b and then moved to the next sampling location. After reaching the next sampling location, the basket is opened to its expandable state. The thermocouples used had a thermal resolution of 0.0001°C, accuracy of 0.02°C and spatial resolution of 0.5mm (Naghavi et al. 2003). The design was applied to in-vivo temperature measurements at the femoral artery of canine subjects and aorta of rabbits with and without atherosclerotic plaques. The thermocouple basket catheter was able to capture the temperature heterogeneity in the diseased subjects with atherosclerotic plaques.

(a) (b)

Figure 1.4 Thermocouple basket based catheter (a) expanded (b) collapsed (Naghavi et al 2003).

Figure 1.5 shows a thermistor based catheter used by Stefanadis et al. 1999 to take in-vivo temperature measurments with patients with stable angina(SA), unstable angina(UA) and patients with acute myocardial infarction (AMI). The catheter consists of the thermistor Th, hydrofoil HF and a guide wire GW. The hydrofoil HF is designed such that the hydrodynamic forces due to blood pushes the thermistor Th against the arterial wall in order to ensure good contact with the wall.

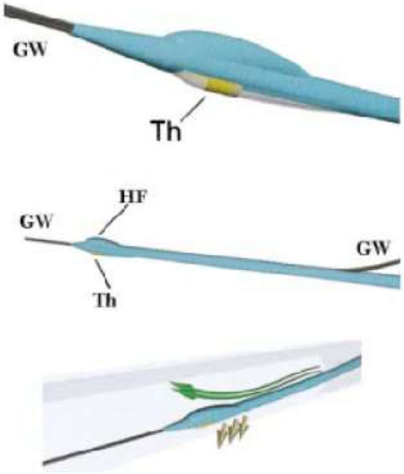

Figure 1.5 Thermistor based catheter with hydrofoil (Stefanadis et al. 1999).

The thermistor used in their study had an accuracy of 0.05°C with spatial resolution of 0.5mm (Stefanadis et al. 1999). The thermistor catheter was able to capture the temperature heterogenity ΔT (temperature difference between atherosclerotic plaque and normal blood temperature) with ΔT being maximum with patients having AMI. Patients with AMI had $\Delta T=1.472\pm0.691^{\circ}C$ (Stefanadis et al. 1999). There is usually discrepancy between the temperature heterogenity ΔT measured between ex-vivo and in-vivo studies. The temperature ΔT measured in ex-vivo studies are typically higher than in-vivo studies and this have been attributed to the cooling effect of blood in in-vivo cases (Stefanadis, 2003 and Casscells, 1996). In order to remove the effects of cooling due to blood flow, Stefanadis et al. 2003 introduced the balloon based catheter as shown in Figure 1.6. The thermistor Th is located opposite to the balloon. The balloon is inflated during temperature measurements in order to block or interrupt blood flow and eliminate the cooling effects of blood.

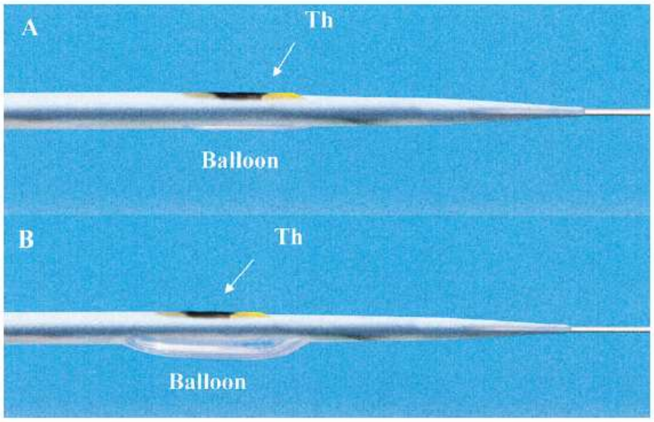

Figure 1.6 Balloon based catheter (Stefanadis et al. 2003).

1.5 Motivation and Research Objectives

The quest to better understand the effects of geometric parameters of vulnerable plaque, composition and other hemodynamic factors on the temperature profile of an atherosclerotic plaque typically requires in-vivo and ex-vivo experiments with human and animal subjects. These efforts in most cases are invasive and expensive. Computational fluid and heat transport models provides more efficient and non-invasive approach to examine the parameter space of interest. The parameter space of interest can be prescribed exactly or in a deterministic manner using computational or numerical methods unlike in-vivo studies where there is randomness in parameter space from one human or animal subject to the other. Computational methods can also aid in the design of efficient thermistor or thermocouple catheter design thereby reducing the number of clinical trials that is needed.

In light of the advantage of the computational or numerical models, it is the intent or objective of the author to develop a computational framework for arterial wall thermography. The computational or numerical implementation requires a multiphysics approach. The multiphysics nature of arterial wall thermography stems from the conjugate heat transfer between the wall and the blood coupled with an elastic or deforming boundary or wall (fluid structure interaction). The computational framework will require a fluid solver to handle the momentum and heat transport, a solid solver to solve the heat transport and structural deformation in the wall and a multiphysics interface coupling scheme for the conjugate heat transfer and fluid structure interaction. A new thermal immersed boundary method based the thermal lattice Boltzmann method was developed for the computational simulations of incompressible flows with heat transfer. The new method was called direct forcing and heating immersed boundary lattice Boltzmann method (IB-LBM). A multiphysics interface coupling scheme within the lattice Boltzmann computational framework was also developed.

1.6 Manuscript Organization

The current manuscript is organized into chapters. Chapter 1 gives background information about vulnerable atherosclerotic plaque and diagnostic methods among which arterial wall thermography falls.

The second chapter describes non continuous approaches to fluid flow modeling to which the lattice Boltzmann method (LBM) belongs. The derivation of the lattice Boltzmann equation from the classical continuous Boltzmann equation was discussed. The multi-scale expansion of the lattice Boltzmann equation to obtain the Navier-Stokes equation was also addressed. Practical implementation of the isothermal LBM was also discussed.

The third chapter describes numerical methods used for fluid structure interaction (FSI) problems. The immersed boundary method (IBM) for handling immersed boundaries in Cartesian based solvers and different variants of IBM were also discussed in the third chapter.

The fourth chapter describes the thermal LBM for solving incompressible flows with heat transfer. The different variants of the thermal LBM were discussed. The chapter also describes the new direct heating IB-LBM developed by the author and its unique advantages over existing thermal IBM based methods. A new and easier method of handling the constant heat flux boundary condition and also estimating the Nusselt number within the IBM computational framework was introduced

The fifth chapter describes the different multiphysics coupling scheme. The chapter also describes the different arterial wall constitutive models available in literature. The finite element discretization of the equation of motion and energy transport in the arterial wall was discussed. The new multiphysics coupling approach was introduced and discussed in the latter sections of the chapter.

The sixth chapter was used for the validation and benchmarking of the developed and the new approach developed by the author. The LBM solver that was developed was benchmarked with classical flows such as Lid driven cavity flow, Couette flows with and without slip boundaries. Secondly the IB-LBM was benchmarked for flows over rigid immersed boundaries such as airfoils and circular cylinders. Thirdly the IB-LBM and the multiphysics coupling scheme were then applied to benchmark flows over a flexible heart valve leaflet. Fourthly the new direct forcing and heating IBM was extensively benchmarked for thermal flows involving forced and natural convection with constant heat flux and temperature boundary conditions. The direct forcing and heating IB-LBM was then applied to a vulnerable plaque to study the effect of plaque geometry, composition and flow properties on the thermal profile of the plaque.

CHAPTER 2

LATTICE BOLTZMANN METHOD

2.1 Non Continuous Approaches to Fluid Flow Modeling

Transport phenomena simulation in fluids can be broadly categorized into continuous and non continuous or molecular approaches (Gad-el-Hak 1999) as shown in Figure 1. In continuous approaches, the fluid is treated as a continuum, examples of continuum modeling approaches are the classical Navier Stokes (NS), Euler and Burnett equations. In non continuous approaches (NCA), the fluid media are not considered as continuum but rather the molecular nature of the fluid is recognized and explicitly considered in the development of methodologies (Liou 2008). NCA represents the fluid as moving particles or molecules interacting with each other via inter-particle collisions. The NCA can be deterministic or statistical. In deterministic approaches such as molecular dynamics (MD), the molecule's trajectory, velocity and intermolecular collision are calculated or simulated in a deterministic manner using classical laws of mechanics. The statistical approaches are governed by the Liouville equation. The Liouville models the temporal and spatial evolution of the probability density function (PDF) of an N-particle system in a 6N dimensional phase space consisting of the velocity and physical spaces. Derivative methods used to solve the Liouville equations are the discrete simulation Monte Carlo (DSMC) and Boltzmann equation. In statistical approaches, such as the DSMC method, randomness is introduced in to the solution variables (Liou 2008). The particle motions are deterministically obtained while the collisions are treated in a statistical manner based on the assumption that particle motion and collision can be uncoupled over small intervals (Oran 1998). The Boltzmann equation is obtained from the Liouville equation under the simplifying assumption that the gas is dilute, "*molecular chaos*" and that range of interaction among the particles are short ranged compared to the mean free path.

The lattice Boltzmann method (LBM) is a specialized finite difference discretization of the Boltzmann equation (He 1997). It was originally proposed by McNamara and Zanetti to circumvent the limitations of statistical noise that plagued Lattice Gas Automata (McNamara 1988). LBM is considered mesoscopic as the simulation particle represents a collection of molecules. The mesoscopic scale is an intermediate scale between the atomistic and continuum scales. The simulation particles is not directly related to the number of molecules like in DSMC or MD hence the computational cost in LBM is less severe when compared with other NCA methods such as DSMC and MD. Due to the kinetic nature of LBM, it can be more readily applied to physical phenomenon that involves molecular interaction or interfacial dynamics than continuum based fluid models. LBM also has the advantage over continuum based fluid models in that convective or streaming term is linear, pressure is determined in LBM via an equation of state unlike the computationally expensive Poisson's equation that has to be solved in continuum based fluid models to obtain pressure (Yu, 2003). In one form or another, LBM has been applied to flows of multiphase and multicomponent (Martys et al. 1996; Swift et al. 1996 and Suppa et al. 2002), in porous media (Succi et al. 1989; Heijs et al. 1995 and Spaid et al. 1997), in droplet dynamics (Raiskinmäki et al. 2000; Schelkle et al. 1995 and Xi et al. 1999) and in microfluidics (Lim et al. 2002; Thamida et al. 2002; Kuksenok et al. 2002).In the following sections, the theoretical concepts of LBM such as the Boltzmann equation (BE), derivation of the Lattice Boltzmann Equation (LBE) from BE and recovery of the macroscopic NS equation from LBE will be discussed. Implementation details such as boundary conditions, transformation of lattice units to physical units and mesh refinement using multi-block within the LBM computational framework will also be discussed

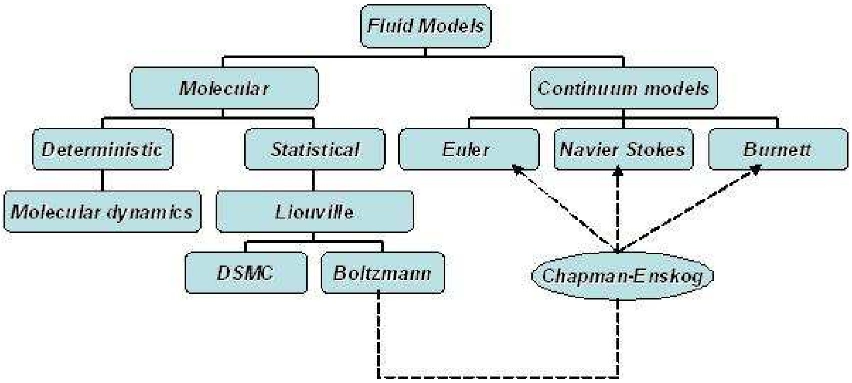

Figure 2.1 Fluid flow modeling approaches (Gad-el-Hak, 1999).

2.2 Boltzmann Equation

The Boltzmann equation is the differential-integral equation that models the time evolution of the particle distribution function (PDF) $f(\mathbf{x},\boldsymbol{\xi},t)$ in phase space as shown in Eq. (2.1).

$$\frac{\partial f}{\partial t} + \boldsymbol{\xi} \bullet \frac{\partial f}{\partial \mathbf{x}} + \mathbf{F} \bullet \frac{\partial f}{\partial \boldsymbol{\xi}} = \Omega \tag{2.1}$$

$$\Omega = \int_{-\infty}^{\infty} \int_{0}^{4\pi} \left(f^{c} f_{1}^{c} - ff_{1} \right) \xi_{r} \sigma \, d\phi \, d\boldsymbol{\xi}_{1} \tag{2.2}$$

The phase space coordinates are the position vector $\mathbf{x}$, momentum vector $\boldsymbol{\xi}$. The PDF $f(\mathbf{x}, \boldsymbol{\xi}, t)$ is defined as the probability of having a fluid particle at position $\mathbf{x}$ with momentum $\boldsymbol{\xi}$ at time t. The first term on the left hand side (LHS) of Eq. (2.1) models the temporal evolution of f, the second term models the convection of the particle in space while the third term models the change of the PDF due to external force **F** acting on the particle. The source term Ω on the right hand side (RHS) of Eq. (2.1) is the collision operator that models the binary collision between particles. The collision operator equation is shown in Eq. (2.2). The quantity σ is the differential collision cross section of two particles during binary collision of molecules with velocity classes $\boldsymbol{\xi}$ and $\boldsymbol{\xi}_1$. The quantity $d\phi$ is the solid angle. f^c and f_1^c are the post collision PDF of f and f_1 respectively. The PDF f_1 and f are for particles moving with velocity $\boldsymbol{\xi}_1$ and $\boldsymbol{\xi}$. ξ_r is a function of the relative velocity between colliding particles. The collision operator in Eq. (2.2) consists of a gain portion $f^c f_1^c$ and the loss term ff_1. The difficulty or major challenge in solving the BE analytical and numerically stems from evaluation of the integral in the collision operator. The integral is complex due to the strong non-linearity of the colliding particles and high dimension required for the integration. Bhatnagar, Gross and Krook (1954) linearized the collision operator by taking an expansion about the equilibrium distribution function (EDF) g^{eq} to obtain the BGK collision operator Ω_{BGK} as shown in Eq. (2.3).

$$\Omega_{BGK} = -\left(\frac{f - g^{eq}}{\lambda} \right) \tag{2.3}$$

where λ is the relaxation time due to collision of fluid particles. The relaxation time controls the rate of approach to equilibrium state. The EDF g^{eq} has a Maxwellian distribution as shown in Eq. (2.4)

$$g^{eq} = \frac{\rho}{(2\pi RT)^{D_o/2}} \exp\left[-\frac{(\boldsymbol{\xi}-\mathbf{u})^2}{2RT} \right] \tag{2.4}$$

where ρ, $\mathbf{u}$ and T are the macroscopic quantities of mass density, velocity and temperature. R and D_o is the ideal gas constant and dimension in space. Inserting the BGK collision operator $\boldsymbol{\Omega}_{BGK}$ into the BE in Eq. (2.1) yields the Boltzmann BGK equation shown in Eq. (2.5).

$$\frac{\partial f}{\partial t} + \xi \bullet \frac{\partial f}{\partial \mathbf{x}} + \mathbf{F} \bullet \frac{\partial f}{\partial \boldsymbol{\xi}} = -\left(\frac{f - g^{eq}}{\lambda} \right) \tag{2.5}$$

The thermo hydrodynamic variables of density ρ, velocity $\mathbf{u}$ and temperature T are determined as moments of the PDF over the particle speed $\boldsymbol{\xi}$ as shown in Eq. (2.6).

$$\rho = \int f \mathbf{d}\boldsymbol{\xi} = \int g^{eq} \mathbf{d}\boldsymbol{\xi} \tag{2.6}$$

$$\rho \mathbf{u} = \int \boldsymbol{\xi} f d\boldsymbol{\xi} = \int \boldsymbol{\xi} g^{eq} d\boldsymbol{\xi} \tag{2.7}$$

$$\frac{D_o \rho RT}{2} = \frac{1}{2} \int (\boldsymbol{\xi}-\mathbf{u})^2 f d\boldsymbol{\xi} = \frac{1}{2} \int (\boldsymbol{\xi}-\mathbf{u})^2 g^{eq} d\boldsymbol{\xi} \tag{2.8}$$

The zero and first order moment with respect to the particle velocity recovers the density and velocity vector.

2.3 Lattice Boltzmann Equation (LBE)

The BE is continuous in phase space and requires discretization in order to solve it numerically. LBE is a discrete finite difference approximation of the BE (He, 1997). The BGK BE can be rewritten in ordinary differential form shown in Eq. (2.9).

$$\frac{df}{dt}+\frac{1}{\lambda}f=\frac{1}{\lambda}g^{eq} \tag{2.9}$$

$$\frac{d}{dt}=\frac{\partial}{\partial t}+\xi\bullet\frac{\partial}{\partial \mathbf{x}} \tag{2.10}$$

Integration of Eq. (2.9) over a discretized time step Δt yields Eq. (2.11)

$$f\left(\mathbf{x}+\xi\Delta t,\xi,t+\Delta t\right)=\frac{1}{\lambda}e^{-t'/\lambda}\int_0^{\Delta t} g^{eq}\left(\mathbf{x}+\xi t',\xi,t+t'\right)dt'+e^{-t'/\lambda}f\left(\mathbf{x},\xi,t\right) \tag{2.11}$$

with the assumption that g^{eq} is smooth and linear over the interval $0\le t'\le\Delta t$. The discretization time step Δt is also assumed to be small. The integrand in Eq. (2.11) can be approximated as

$$\begin{aligned} g^{eq}\left(\mathbf{x}+\xi t',\xi,t+t'\right)=&\left(1-\frac{t'}{\Delta t}\right)g^{eq}\left(\mathbf{x},\xi,t\right)+\frac{t'}{\Delta t}g^{eq}\left(\mathbf{x}+\xi\Delta t,\xi,t+\Delta t\right)\\ &+O\left(\Delta t^2\right)\quad 0\le t'\le\Delta t \end{aligned} \tag{2.12}$$

Substituting Eq. (2.12) into Eq. (2.11) and taking a Taylor series expansion of the RHS of Eq. (2.13) reduces to

$$f\left(\mathbf{x}+\boldsymbol{\xi}\Delta t,\boldsymbol{\xi},t+\Delta t\right)=f\left(\mathbf{x},\boldsymbol{\xi},t\right)-\frac{1}{\tau_f}\left[f\left(\mathbf{x},\boldsymbol{\xi},t\right)-g^{eq}\left(\mathbf{x},\boldsymbol{\xi},t\right)\right] \tag{2.13}$$

$$\tau_f=\frac{\lambda}{\Delta t} \tag{2.14}$$

where τ_f is the dimensionless relaxation time. Eq. (2.13) is the temporal discretization of the BE. The phase space $\boldsymbol{\xi}$ and $\mathbf{x}$ have to be discretized in order to reduce Eq. (2.13) to the LBE. The discretization process of phase spaces $\boldsymbol{\xi}$ and $\mathbf{x}$ in LBM is such that configuration space $\mathbf{x}$ and $\boldsymbol{\xi}$ are coupled (He 1997). This is achieved by the LBM lattice structure. Taking the Taylor series expansion of g^{eq} about the macroscopic velocity $\mathbf{u}$ to obtain Eq. (2.15)

$$g^{eq}=f^{eq}+O(\mathbf{u}^3) \tag{2.15}$$

$$f^{eq}=\frac{\rho}{(2\pi RT)^{D_o/2}}\exp\left[-\frac{(\boldsymbol{\xi})^2}{2RT}\right]\times\left(1+\frac{\boldsymbol{\xi}\bullet\mathbf{u}}{RT}+\frac{\left(\boldsymbol{\xi}\bullet\mathbf{u}\right)^2}{2\left(RT\right)^2}-\frac{\mathbf{u}^2}{2RT}\right) \tag{2.16}$$

f^{eq} is the approximate EDF obtained by taking a small velocity (low-Mach) number expansion up to second order. Substituting Eq. (2.15) into the conservation equations Eq. (2.6) – (2.8) and neglecting higher terms of velocity expansion yields

$$\rho = \int f^{eq} \mathbf{d\xi} \tag{2.17}$$

$$\rho \mathbf{u} = \int \boldsymbol{\xi} f^{eq} d\boldsymbol{\xi} \tag{2.18}$$

$$\frac{D_o \rho RT}{2} = \frac{1}{2} \int \left(\boldsymbol{\xi} - \mathbf{u}\right)^2 f^{eq} d\boldsymbol{\xi} \tag{2.19}$$

The integral used in determination of the moments in Eq. (2.17) – (2.19) can be generalized as

$$I = \int \exp\left(-\boldsymbol{\beta}^2\right) \psi(\boldsymbol{\beta}) d\boldsymbol{\beta} \tag{2.20}$$

$$\boldsymbol{\beta} = \frac{\boldsymbol{\xi}}{\sqrt{2RT}} \tag{2.21}$$

$$\psi(\boldsymbol{\beta}) = \frac{\boldsymbol{\beta}^m \rho \left(2RT\right)^{(m+1-D)/2}}{\pi^{D/2}} \left[1 + \frac{2\left(\boldsymbol{\beta} \bullet \mathbf{u}\right)}{\sqrt{2RT}} + \frac{\left(\boldsymbol{\beta} \bullet \mathbf{u}\right)^2}{RT} - \frac{\mathbf{u}^2}{2RT}\right] \tag{2.22}$$

where m is the order of hydrodynamic moment required in order to obtain the macroscopic NS equation. The range of values for m is 0≤ m ≤ 3 for thermal models otherwise the range is 0≤ m ≤ 4 (He, 1997). The integral in Eq. (2.20) can be evaluated numerically using the Gauss-Hermite quadrature (Abramowitz 1972)

$$I = \int \exp\left(-\boldsymbol{\beta}^2\right) \psi(\boldsymbol{\beta}) d\boldsymbol{\beta} \approx \sum_{k=1}^{L} W_k \psi(\boldsymbol{\beta}_k) \tag{2.23}$$

$$W_k = \frac{2^{L-1} L! \sqrt{\pi}}{L^2 \left[H_{k-1}(\boldsymbol{\beta}_k)\right]^2} \tag{2.24}$$

where W_k, $\boldsymbol{\beta}_k$, L are the weights, abscissas or discrete velocities and number of integration points of the numerical quadrature. H_{k-1} is the Hermite polynomial of degree $k-1$. Evaluation of the integral numerically and the PDF evolution equation (Eq. (2.13)) in conjunction with the lattice units structure yields the LBE shown in Eq. (2.25)

$$f_i(\mathbf{x}+\mathbf{e}_i\Delta t, t+\Delta t) = f_i(\mathbf{x},t) - \frac{1}{\tau_f}\left[f_i(\mathbf{x},t) - f_i^{eq}(\mathbf{x},t)\right] \tag{2.25}$$

$$f_i^{eq} = \rho w_i\left[1+\frac{3}{e^2}(\mathbf{e}_i \bullet \mathbf{u}) + \frac{9}{2e^4}(\mathbf{e}_i \bullet \mathbf{u})^2 - \frac{3}{2e^2}\mathbf{u}\bullet\mathbf{u}\right] \tag{2.26}$$

where f_i , f_i^{eq}, $\mathbf{e}_i$ and e are the PDF, EDF, particle velocity and velocity magnitude along the ith direction of the lattice structure. The weights w_i in the EDF as shown in Eq. (2.26) are determined such that conservation constraints are satisfied and symmetry of the NS equations are retained. The hydrodynamic variables are obtained from the moment of the discrete PDF over the discrete velocity $\mathbf{e}_i$.

$$\sum f_i = \sum f_i^{eq} = \rho \tag{2.27}$$

$$\sum f_i\ \mathbf{e}_i = \sum f_i^{eq}\mathbf{e}_i = \rho\mathbf{u} \tag{2.28}$$

$$P = \rho C_s^2 \tag{2.29}$$

$$\nu = C_s^2\Delta t\left(\tau_f - \frac{1}{2}\right) \tag{2.30}$$

where *P,* C_s and ν are the fluid pressure, lattice speed of sound and kinematic viscosity.

2.4 Lattice Pattern and Lattice Structure

The lattice structure in the LBM helps in discretization of the fluid domain into nodes/particles. The lattice structure also couples the configuration and momentum phase spaces. The lattice structure must have symmetry in order to properly recover the NS equations and ensure velocity independent pressure, isotropy and Galilean invariance. The general nomenclature used for describing the lattice structure is DxQy, the letter x and y represents the dimensions and speed model respectively. The D2Q7 and D2Q9 lattice model are shown in Figure 2.2 and Figure 2.3.

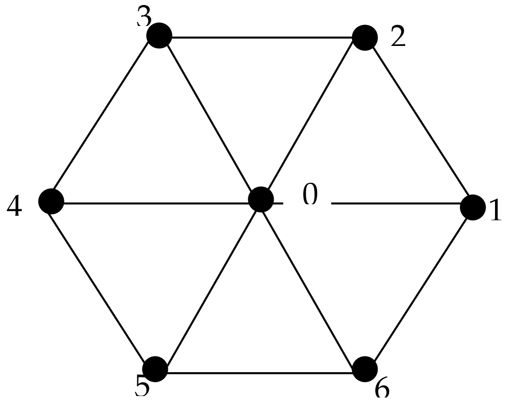

Figure 2.2 2D, 7 speed (D2Q7) model.

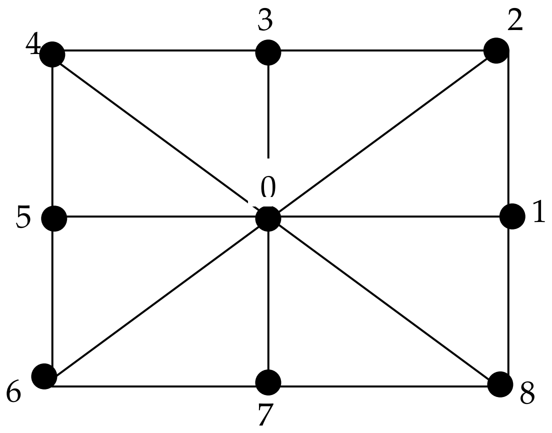

Figure 2.3 2D, 9 speed (D2Q9) model.

D2Q7 has a rest or stationary particle labeled 0 and moving particles labeled 1 to 6 in Figure 2.1. Similarly, the D2Q9 has rest particle labeled 0 and moving particles labeled 1 to 8 in Figure 2.2. For 3D simulation, popular cubic lattice patterns are the D3Q15, D3Q19 and D3Q27 models. The lattice structure determines the weights w_i in EDF , lattice speed of sound by solving the integral in Eq. (2.23). Using the D2Q9 lattice structure as an example, the numerical quadrature (Eq. (2.23)) in 2D Cartesian configuration space can be reduced to

$$I=\frac{\rho}{\pi}\left(\sqrt{2RT}\right)^{j+k}\left\{\left(1-\frac{\mathbf{u}^2}{2RT}\right)I_jI_k+\frac{2\left(u_xI_{j+1}I_k+u_yI_jI_{k+1}\right)}{\sqrt{2RT}}\right.$$
$$\left.+\frac{2\left(u_x^2I_{j+2}I_k+2u_xu_yI_{j+1}I_{k+1}+u_y^2I_jI_{k+2}\right)}{RT}\right\} \tag{2.31}$$

$$I_j=\int_{-\infty}^{+\infty}\beta^j\exp(-\beta^2)\,d\beta \tag{2.32}$$

where u_x and u_y are the velocity components in the Cartesian coordinate system. Using three integration points for the Gauss-Hermite quadrature, the points are

$$\beta_1=-\sqrt{3/2}\ ,\ \ \beta_2=0\ ,\ \ \beta_3=\sqrt{3/2} \tag{2.33}$$

The corresponding weights of the numerical quadrature are

$$W_1=\frac{\sqrt{\pi}}{6}\ ,\ \ \mathrm{W}_2=\frac{2\sqrt{\pi}}{3}\ ,\ \ \mathrm{W}_3=\frac{\sqrt{\pi}}{6} \tag{2.34}$$

Evaluation of the integral in Eq. (2.31) and using the relationship in Eq. (2.21) reduces to

$$I=\sum_{\alpha,\gamma=1}^{3}\xi_{\alpha,\gamma}^{m}f_{\alpha,\gamma}^{eq} \tag{2.35}$$

$$f_{\alpha,\gamma}^{eq} = \frac{\rho}{\pi} W_\alpha W_\gamma \boldsymbol{\xi}_{\alpha,\gamma}^{m} \left[1 + \frac{\left(\boldsymbol{\xi}_{\alpha,\gamma} \bullet \mathbf{u}\right)}{RT} + \frac{\left(\boldsymbol{\xi}_{\alpha,\gamma} \bullet \mathbf{u}\right)^2}{2\left(RT\right)^2} - \frac{\mathbf{u}^2}{2RT} \right] \tag{2.36}$$

where α, γ and m are the indices for the integration and order of the moment. The weights can be further reduced to

$$w_i = \frac{W_\alpha W_\gamma}{\pi} = \begin{cases} 4/9, & \alpha=\gamma=2,\ i=0 \\ 1/9, & \alpha=1, \gamma=2,\ i=1,3,5,7 \\ 1/36, & \alpha=\gamma=1,\ i=2,4,6,8 \end{cases} \tag{2.37}$$

where w_i is the weight along the i^th^ direction of the D2Q9 model. The lattice speed from the abscissas of the quadrature and lattice sound speed are determined as

$$\xi_1 = -e\ , \quad \xi_2 = 0\ , \quad \xi_3 = e \tag{2.38}$$

$$e = \sqrt{3RT} \tag{2.39}$$

$$C_s = \sqrt{RT} = \frac{e}{3} \tag{2.40}$$

The D2Q9 discretizes the configuration space into a square with a lattice constant or distance of $e\Delta t$, the momentum space with velocity vector $\mathbf{e}_i$ for the D2Q9 model is defined as

$$e_i = \begin{cases} 0 \quad i=0 \\ e\left[\dfrac{\cos(i-1)\pi}{4}, \dfrac{\sin(i-1)\pi}{4}\right], \; i=1,3,5,7 \\ \left(\sqrt{2}\right)e\left[\dfrac{\cos(i-1)\pi}{4}, \dfrac{\sin(i-1)\pi}{4}\right], \; i=2,4,6,8 \end{cases} \tag{2.41}$$

With the relations in Eq.(2.37)-(2.41) for the D2Q9, the EDF in Eq. (2.36) can be reduced to the form of Eq. (2.26) with all the lattice specific parameters determined. The same procedure can be repeated for other lattice models to determine the lattice specific parameters. The lattice parameters for other models are shown in Table 2.1

Table 2.1 Lattice parameters for popular 2D and 3D lattice models (Qian et al. 1992)

Lattice Model	Lattice Speed $\lvert e_i \rvert^2$	w_i	C_s^2
D1Q3	0	$2/3$	$1/3$
	1	$1/6$	
D2Q9	0	$4/9$	$1/3$
	1	$1/9$	
	2	$1/36$	
D3Q15	0	$2/9$	$1/3$
	1	$1/9$	
	3	$1/72$	
D3Q19	0	$1/3$	$1/3$
	1	$1/18$	
	2	$1/36$	

2.5 Reduction to the Navier-Stokes Equation

In order for the LBM to simulate the macroscopic hydrodynamic NS equation, the NS should be recoverable from the LBE. Taking the Taylor series expansion of the LBE (Eq. (2.26)) in both space and time.

$$\begin{aligned}&\Delta t\left(\frac{\partial f_i}{\partial t}+e_i.\nabla f_i\right)+\frac{\Delta t^2}{2}\left(\frac{\partial^2 f_i}{\partial t^2}+2e_i.\nabla\frac{\partial f_i}{\partial t}+e_ie_i:\nabla\nabla f_i\right)\\&+O(\Delta t^3)=-\frac{1}{\tau_f}\left(f_i-f_i^{eq}\right)\end{aligned}\tag{2.42}$$

Assuming Δt is of the same order as the Knudsen number ε. The expansion can then be rewritten in terms of the Knudsen number

$$\begin{aligned}&\Delta\varepsilon\left(\frac{\partial f_i}{\partial t}+e_i.\nabla f_i\right)+\frac{\Delta\varepsilon^2}{2}\left(\frac{\partial^2 f_i}{\partial t^2}+2e_i.\nabla\frac{\partial f_i}{\partial t}+e_ie_i:\nabla\nabla f_i\right)\\&+O(\Delta\varepsilon^3)=-\frac{1}{\tau_f}\left(f_i-f_i^{eq}\right)\end{aligned}\tag{2.43}$$

Using the Chapman-Enskog expansion (Chapman et al. 1970) to perform a multi-scale expansion of the PDF, time and space with its associated derivatives yields

$$t=t_0+\varepsilon t_1+\varepsilon^2 t_2+O(\varepsilon^3)\tag{2.44}$$

$$x=\mathbf{x}_0+\varepsilon\mathbf{x}_1+\varepsilon^2\mathbf{x}_2+O(\varepsilon^3)\tag{2.45}$$

$$f_i=f_i^{(0)}+\varepsilon f_i^{(1)}+\varepsilon^2 f_i^{(2)}+O(\varepsilon^3)\tag{2.46}$$

$$\frac{\partial}{\partial t}=\frac{\partial}{\partial t_0}+\varepsilon\frac{\partial}{\partial t_1}+\varepsilon^2\frac{\partial}{\partial t_2}+O(\varepsilon^3)\tag{2.47}$$

$$\frac{\partial}{\partial \mathbf{x}} = \frac{\partial}{\partial \mathbf{x}_0} + \varepsilon \frac{\partial}{\partial \mathbf{x}_1} + \varepsilon^2 \frac{\partial}{\partial \mathbf{x}_2} + O(\varepsilon^3) \qquad (2.48)$$

Substituting the Chapman-Enskog expansion into the Eq. (2.43) and separating to the zero, first and second orders of ε.

$$O(\varepsilon^0): \qquad f_i^{(0)} = f_i^{eq} \qquad (2.49)$$

$$O(\varepsilon^1): \qquad \Delta t \left[\frac{\partial f_i^{(0)}}{\partial t_1} + e_{ik} \frac{\partial f_i^{(0)}}{\partial x_{1k}} \right] = \frac{-1}{\tau} f_i^{(1)} \qquad (2.50)$$

$$O(\varepsilon^2): \qquad \begin{aligned} &\Delta t \left[\frac{\partial f_i^{(1)}}{\partial t_1} + \frac{\partial f_i^{(0)}}{\partial t_2} + e_{ik} \frac{\partial f_i^{(1)}}{\partial x_{1k}} \right] + \\ &\frac{\Delta t^2}{2} \left[\frac{\partial^2 f_i^{(0)}}{\partial t_1^2} + 2 e_{ik} \frac{\partial^2 f_i^{(0)}}{\partial t_1 \partial x_{1k}} + e_{ik} e_{im} \frac{\partial^2 f_i^{(0)}}{\partial x_{1m} \partial x_{1k}} \right] = -\frac{f_i^{(2)}}{\tau_f} \end{aligned} \qquad (2.51)$$

Using Eq. (2.50), Eq. (2.51) can be simplified to

$$\Delta t \left(\frac{\partial f_i^{(0)}}{\partial t_2} - \left(\frac{1}{2\tau_f} - 1 \right) \left[\frac{\partial f_i^{(1)}}{\partial t_1} + e_{ik} \frac{\partial f_i^{(1)}}{\partial x_{1k}} \right] \right) = -\frac{f_i^{(2)}}{\tau_f} \qquad (2.52)$$

Using Eq. (2.49)-(2.52), the multi-scale expansion of the PDF simplifies to

$$f_i = f_i^{eq} + \varepsilon f_i^{(1)} + \varepsilon^2 f_i^{(2)} + O(\varepsilon^3) \qquad (2.53)$$

Using Eq. (2.52) and constraints on the EDF in Eq. (2.27)-(2.28) yields the following

$$\sum_i f_i^{(1)} = \sum_i f_i^{(2)} = 0 \qquad (2.54)$$

$$\sum_i f_i^{(1)} \mathbf{e}_i = \sum_i f_i^{(2)} \mathbf{e}_i = 0 \qquad (2.55)$$

Taking the summation of Eq. (2.50) over the lattice directions *i* and using Eq. (2.54) yields the continuity equation to the first order

$$\frac{\partial \sum_i f_i^{(0)}}{\partial t_1} + \sum_i e_{ik} \frac{\partial f_i^{(0)}}{\partial x_{1k}} = \frac{\partial \rho}{\partial t_1} + \frac{\partial \rho u_k}{\partial x_{1k}} = 0 \tag{2.56}$$

Multiplying Eq. (2.50) by the particle velocity e_{im} and taking the summation over the lattice directions *i* yield the momentum equations to the first order

$$\frac{\partial \sum_i e_{im} f_i^{(0)}}{\partial t_1} + \sum_i e_{ik} e_{im} \frac{\partial f_i^{(0)}}{\partial x_{1k}} = \frac{\partial \rho u_m}{\partial t_1} + \sum_i e_{ik} e_{im} \frac{\partial f_i^{(0)}}{\partial x_{1k}} = 0 \tag{2.57}$$

Proceeding to the second order terms, summing over Eq. (2.52) and using the constraints in Eq. (2.54)-(2.55)

$$\left(\frac{\partial \sum_i f_i^{(0)}}{\partial t_2} + \left(\frac{1}{2\tau_f} - 1 \right) \left[\frac{\partial \sum_i f_i^{(1)}}{\partial t_1} + \sum_i e_{ik} \frac{\partial f_i^{(1)}}{\partial x_{1k}} \right] \right) = \frac{\partial \rho}{\partial t_2} = 0 \tag{2.58}$$

Multiplying Eq. (2.52) by the particle velocity e_{im} and summing over the lattice directions

$$\left(\frac{\partial \sum_i e_{im} f_i^{(0)}}{\partial t_2} - \left(\frac{1}{2\tau_f} - 1 \right) \Delta t \left[\frac{\partial \sum_i e_{im} f_i^{(1)}}{\partial t_1} + \sum_i e_{im} e_{ik} \frac{\partial f_i^{(1)}}{\partial x_{1k}} \right] \right) \\ = \frac{\partial \rho u_m}{\partial t_2} - \left(\frac{1}{2\tau_f} - 1 \right) \Delta t \sum_i e_{im} e_{ik} \frac{\partial f_i^{(1)}}{\partial x_{1k}} = 0 \tag{2.59}$$

Combining the first order continuity equation (Eq. (2.56)) and second order continuity equation (Eq. (2.58)) yields the continuity equation expressed as

$$\frac{\partial \rho}{\partial t} + \frac{\partial \rho u_k}{\partial x_k} = 0 \tag{2.60}$$

Combining the first order (Eq. (2.57)) and second order (Eq. (2.59)) momentum equations yields

$$\frac{\partial \rho u_m}{\partial t} + \sum_i e_{ik} e_{im} \frac{\partial f_i^{(0)}}{\partial x_{1k}} = \left(\frac{1}{2\tau_f} - 1 \right) \Delta t \sum_i e_{im} e_{ik} \frac{\partial f_i^{(1)}}{\partial x_{1k}} \tag{2.61}$$

Eq. (2.61) can be re-written in the form

$$\frac{\partial \rho u_m}{\partial t} + \frac{\partial \Pi_{km}^{(0)}}{\partial x_{1k}} = \left(\frac{1}{2\tau_f} - 1 \right) \Delta t \frac{\partial \Pi_{km}^{(1)}}{\partial x_{1k}} \tag{2.62}$$

Using the following definitions in Eq.(2.63-2.64)

$$e_{ik} e_{im} f_i^{(0)} = \Pi_{km}^{(0)} = \rho u_k u_m + P \delta_{km} \tag{2.63}$$

$$e_{ik}e_{im}f_i^{(1)} = \Pi_{km}^{(1)} = S_{km} \qquad (2.64)$$

where δ_{km} and S_{mk} is the Kronecker delta and strain rate tensor. Substituting Eq. (2.63) – (2.64) into Eq. (2.62) yields the NS equations

$$\frac{\partial \rho u_m}{\partial t} + u_k \frac{\partial u_m}{\partial x_k} = -\frac{\partial P}{\partial x_k} + \rho\nu \frac{\partial S_{mk}}{\partial x_k} \qquad (2.65)$$

where ν is the kinematic viscosity.

2.6 Implementation of LBM

This section addresses the practical implementation concepts in LBM. Concepts addressed in this section are the streaming and collision steps, boundary conditions, grid refinement technique using the multi-block LBM and unit conversion between physical and lattice units.

2.6.1 Streaming and Collision Process

LBM consists of two steps namely the streaming and collision processes. During the streaming step, the particles move to the neighboring lattice points in the direction of its velocity. The streaming process models the molecule transport in between two successive collisions. It is global in nature since the PDF at a node needs propagating information from its neighbors. Figure 2.4a-2.4b shows a fluid domain that is discretized into 2 X 3 nodes by a D2Q9 lattice model before and after streaming. The black dots represent some representative PDF used for illustrative purposes. The PDF f_3 at location 1-1 in Figure 2.4a at time t streams in the vertical direction to location 1-2 at time $t+\Delta t$ in Figure 2.4b.

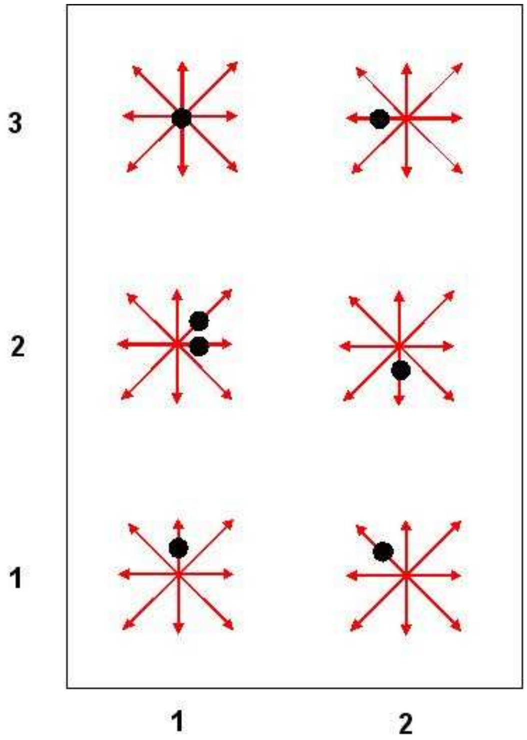

Figure 2.4a D2Q9 model before streaming at time t.

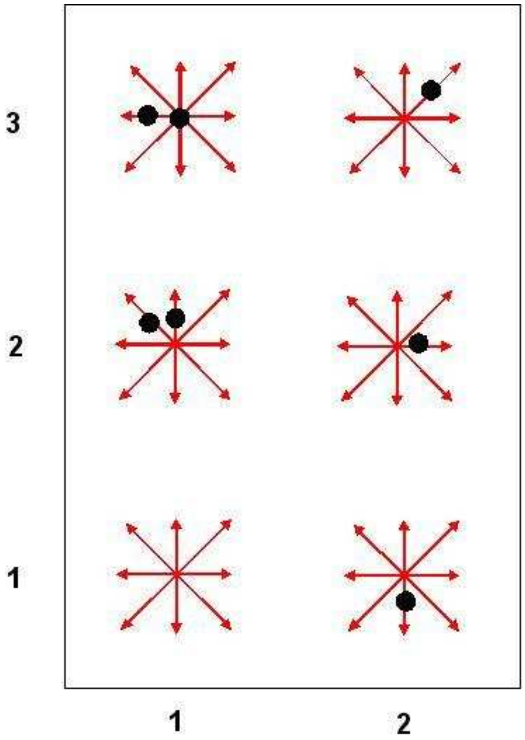

Figure 2.4b D2Q9 model after streaming at time t+Δt.

Similarly the rest or stationary particle f_0 at location 1-3 before streaming remains immobile after the streaming step, there is also an arriving PDF f_5 at location 1-3 from location 2-3 after streaming. The streaming step can be expressed as

$$f_i(x+e_i\Delta t, t+\Delta t) = f_i^k(x,t) \tag{2.66}$$

where $f_i^k(x,t)$ is the post collision or before streaming PDF. During the collision step, the arriving particles to the next neighborhood lattice site interact with each other according to scattering rules and change their velocity directions. The collision process is local. The collision step models the interaction between fluid particles and can be expressed as

$$f_i^k(x,t) = f_i(x,t) + \Omega_i \tag{2.67}$$

$$\Omega_i = -\frac{1}{\tau}\left(f_i(x,t) - f_i^{eq}(x,t)\right) \tag{2.68}$$

Ω_i is the BGK collision operator in the i^{th} lattice direction. The collision operator does not change the total mass and velocity magnitude at the node but changes the distribution along the lattice directions. The collision operator must satisfy the following two constraints for mass and momentum conservation

$$\sum_i \Omega_i = 0 \tag{2.69}$$

$$\sum_i \Omega_i \mathbf{e}_i = 0 \tag{2.70}$$

2.6.2 Boundary Conditions

Boundary conditions in LBM can be categorized into inlet/outlet and wall boundary conditions. Unlike the NS equations or continuum based methods where the boundary conditions can be directly imposed on the primary variables of velocity and/or pressure, in LBM the boundary conditions have to be imposed indirectly by using the

PDF f. Implementation of boundary conditions in LBM is done by using suitable schemes to determine the unknown PDF from the known PDF at the boundary of the fluid domain.

Wall Boundary Conditions

The wall boundary conditions are the no-slip and slip boundary conditions. For the no-slip boundary condition, the tangential and normal velocity components at the wall are zero. In order to achieve the no-slip in LBM, the incoming and known PDF is bounced back in the opposite direction to determine the outgoing and unknown PDF. This no-slip implementation is called the bounce-back scheme (Succi 2001). The unknown PDF for a D2Q9 model in a channel flow are represented with the dotted lines as shown in Figure 2.5.

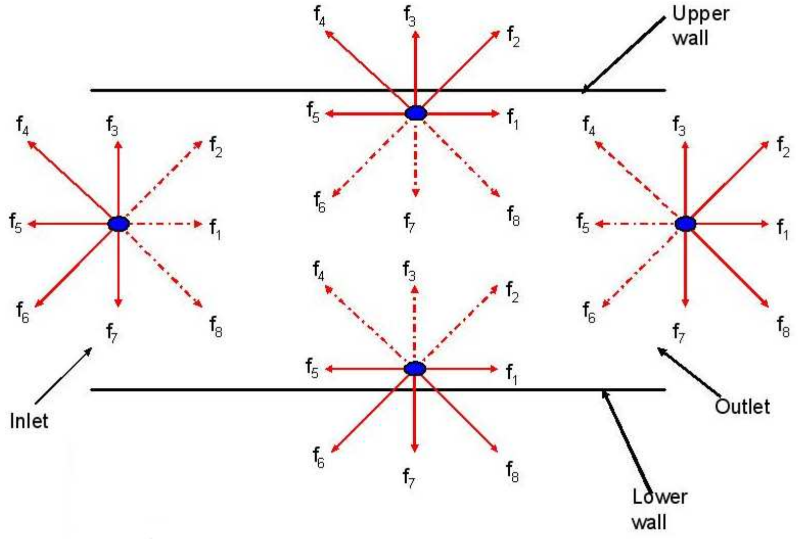

Figure 2.5 Unknown PDF (dotted lines) at boundary of a 2D channel using D2Q9 model.

At the lower wall, the PDFs f_2, f_3 and f_4 are unknown while f_6, f_7 and f_8 are unknown for the upper wall. Implementation of the bounce back scheme for the lower and upper walls are shown in Eq. (2.71) and Eq. (2.72).

$$\begin{aligned} f_2 &= f_6 \\ f_3 &= f_7 \\ f_4 &= f_8 \end{aligned} \tag{2.71}$$

$$\begin{aligned} f_6 &= f_2 \\ f_7 &= f_3 \\ f_8 &= f_4 \end{aligned} \tag{2.72}$$

The bounce back is first order accurate, second order accuracy can be achieved by using the half way bounce-back scheme. The wall is shifted by one half mesh unit towards the fluid in the half way bounce-back scheme (Succi, 2001 and Chen et al. 1998). In the slip boundary condition there is a tangential slip velocity between the wall and the adjacent fluid zone. The slip velocity for isothermal gas flows can be estimated by expression shown in Eq. (2.73) to the first order of Knudsen number *Kn* (Succi et al. 2005).

$$u_f - u_w = \frac{2-\sigma_v}{\sigma_v} Kn \frac{\partial u_f}{\partial n} \tag{2.73}$$

$$\sigma_v = \frac{m_i - m_r}{m_i - m_w} \tag{2.74}$$

Where u_f, u_w, σ_v and n are the fluid velocity, wall velocity, the tangential momentum accommodation coefficient and the outward unit normal. The variables m_i, m_r and m_w

are the incoming momentum of gas molecules before collision with the wall, outgoing momentum of molecules after collision with wall and momentum of the wall respectively. The two extreme values of σ_v is when it assumes the value of 0 (specular reflection) and 1(diffuse reflection). In diffuse reflection, the reflected gas molecules have completely lost memory information of the incoming gas molecules. In reality the reflection at the wall is between specular and diffuse reflections. In order to implement the slip BC in LBM, it is assumed that a fraction α of the particle distribution is diffusely reflected while (1- α) will be specularly reflected (Zhang et al. 2005). The constant α is related to σ_v. An implementation of the partly diffusive and specular LBM boundary condition to capture slip effects for the lower wall in Figure 2.4 is shown in Eq. (2.75).

$$\begin{aligned} f_2 &= (1-\alpha) f_8 \\ f_3 &= (1-\alpha) f_6 + (1-\alpha) f_8 + f_7 \\ f_4 &= (1-\alpha) f_8 \end{aligned} \tag{2.75}$$

The values of σ_v is readily available from experiment and well documented in literatures for different surface conditions and gases, the availability of experimental values for the accommodation coefficient makes this type of boundary condition more universal and physically realistic(Zhang et al. 2005).

Inlet/Outlet Boundary Conditions

The velocity and pressure boundary condition proposed by Zou et al. 1997 was used in the current work for prescribing velocity or pressure boundary conditions at the open boundary of the computational domain. The Zou boundary condition assumes a bounce- back rule for non-equilibrium component of f normal to the boundary. Making reference to Figure 2.4, the non-equilibrium bounce back for normal component of f at the inlet is

$$f_1 - f_1^{eq} = f_5 - f_5^{eq} \tag{2.76}$$

Using Eq. (2.27), Eq. (2.28) and Eq. (2.76), the pressure boundary condition at the inlet boundary in Figure 5 is implemented as

$$\begin{aligned} u_x &= \frac{P_{in}}{C_s^2} - (f_0 + f_3 + f_7 + 2(f_5 + f_4 + f_6)) \\ f_8 &= f_4 + \frac{1}{2}(f_3 - f_7) + \frac{u_x}{6} \\ f_1 &= f_5 + \frac{2u_x}{3} \\ f_2 &= f_6 - \frac{1}{2}(f_3 - f_7) + \frac{u_x}{6} \end{aligned} \tag{2.77}$$

where P_{in} is the prescribed pressure at the inlet. Similarly for a prescribed inlet normal velocity $u_{x,in}$, the velocity boundary condition at the inlet can be implemented using Eq. (2.78). Similar procedure can be followed for implementation at the other open boundaries.

$$
\begin{aligned}
\rho &= \frac{(f_0 + f_3 + f_7 + 2(f_5 + f_4 + f_6))}{(1 - u_{x,in})} \\
f_8 &= f_4 + \frac{1}{2}(f_3 - f_7) + \frac{\rho u_{x,in}}{6} \\
f_1 &= f_5 + \frac{2\rho u_{x,in}}{3} \\
f_2 &= f_6 - \frac{1}{2}(f_3 - f_7) + \frac{\rho u_{x,in}}{6}
\end{aligned}
\tag{2.78}
$$

2.6.3 Multi-Block LBM

The computational efficiency in LBM is limited by the fact that discretization of the fluid domain is constrained to a uniform grid or lattice. Fine grid resolution is needed in regions with high shear rate or high gradient of the hydrodynamic variables. The use of fine grid in such high gradient region necessitates that a uniform fine grid has to be used in the entire computational domain in LBM. Using the fine grid resolution in low gradient regions or where it is not needed wastes computational resources and increases the computational cost. The Multi-Block LBM (Yu 2002) circumvents this limitation by placing fine uniform grid block in the high gradient regions and using a coarser grid block in other areas. The information exchange between the coarse and fine grid block is such that at their interfaces there is continuity of density, velocity, viscosity, stress. Figure 2.6 shows the interface structure between the coarse and fine block mesh, the fine block interface is represented by the line AI (with fine grid points running points A to I) while the coarse block interface is the line JR (with coarse grid points J,L,N,P and R). The fine block grid is refined by a factor of *m* both space and time (*m* =2 for the case shown in Figure 2.5). The fine block interface is embedded in the coarse block while the coarse block interface is embedded in the fine block, consequently information at the fine block interface comes from the coarse block and information at coarse block interface comes from the fine block.

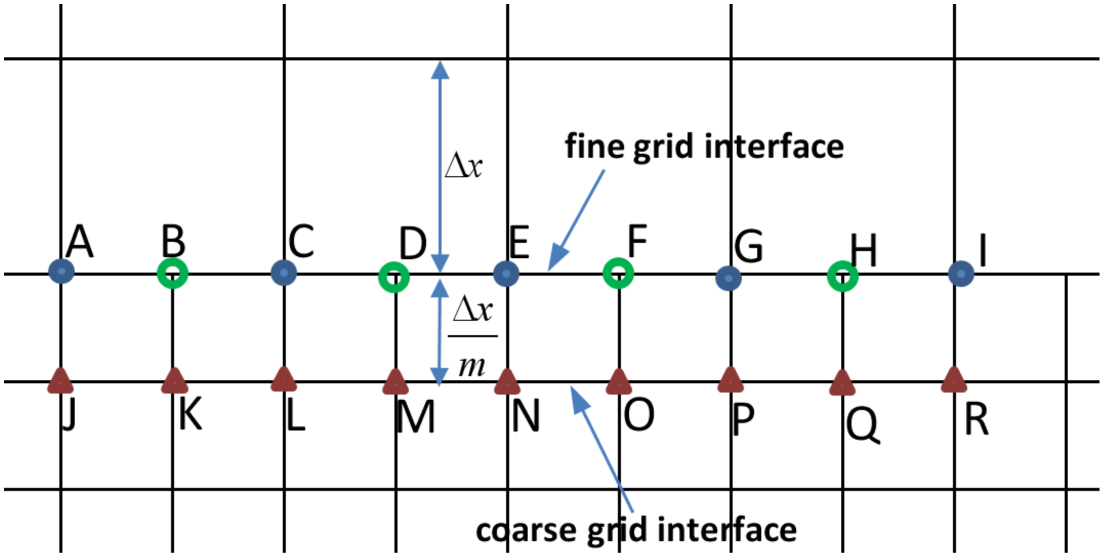

Figure 2.6 Interface structure between fine and coarse mesh.

At the fine grid interface, there is an exchange of PDF and EDF at the coarse grid points with the filled blue circles (A, C, E, G and I) to its corresponding equivalent values on the fine grid using Eq. (2.80) – Eq. (2.81).

$$\tau_{ff} = \frac{1}{2} + m\left(\tau_f - \frac{1}{2}\right) \tag{2.79}$$

$$ff_i^{eq} = f_i^{eq} \tag{2.80}$$

$$ff_i^k = f_i^{eq} + \frac{\tau_{ff} - 1}{m\left(\tau_f - 1\right)}\left[f_i^k - f_i^{eq}\right] \tag{2.81}$$

Where τ_{ff}, ff_i^{eq} and ff_i^k are the relaxation factor, EDF and post-collision PDF on the fine grid. The continuity of viscosity, hydrodynamic variables (pressure, density and velocity) and stress at the fine grid interface is ensured by Eq. (2.79), Eq. (2.80) and Eq. (2.81) respectively (Yu, 2002). Spatial interpolation is needed in order to obtain the corresponding EDF ff_i^{eq} and post-collision PDF ff_i^k at the fine interface for the grid points shown in green doughnut whose EDF and PDF cannot be obtained using Eq. (2.80)- (2.81) because there are no corresponding coarse grid points. In addition to the spatial interpolation, temporal interpolation is needed for all grid points on the fine grid interface at intermediate time due to subdivision of the time step in the fine block.

After *m* iterations of the fine block, information is passed from fine block to the coarse grid points (J, L, N, P and R) at the coarse grid interface using Eq. (2.80) and Eq. (2.82).

$$f_i^k = ff_i^{eq} + \frac{m\left(\tau_f - 1\right)}{\tau_{ff} - 1}\left[ff_i^k - ff_i^{eq}\right] \tag{2.80}$$

2.6.4 Lattice Units to Physical Units

The fluid transport variables determined in LBM are in lattice units (LU). The fluid transport variables in LU need to be converted back to physical units (PU) and vice-versa. The dimensionless numbers governing the fluid transport phenomenon are used to convert from the lattice units to the physical units. This is done by ensuring that the dimensionless numbers are of the same magnitude in both lattice and physical units. The dimensionless variables also help in setting up the LBM parameters such as the relaxation time τ (which in turn determines the kinematic viscosity in LU) or the characteristic velocity. Examples of such dimensionless numbers are Reynolds (Re), Knudsen (Kn), Eckert (Ec), and Prandtl (Pr) numbers.

For illustrative purposes, consider the flow of a fluid in a 2D channel with the unit Reynolds number and the following parameters

L = channel height = characteristic length = 10^{-3}m

U = fluid inlet velocity = characteristic velocity = 10^{-3}m/s

ν = kinematic viscosity = 10^{-6}m^{2}s^{-1}

Using the Re and T^* as a suitable dimensionless number for scaling between the LU and PU as shown in Eq. (2.81) and Eq. (2.82).

$$\mathrm{Re} = \frac{UL}{\nu} = \frac{U_{LU} L_{LU}}{\nu_{LU}} \tag{2.81}$$

$$T^* = \frac{t}{\frac{L}{U}} = \frac{t_{LU}}{\frac{L_{LU}}{u_{LU}}} \tag{2.82}$$

Where *t*, L and U are the time, characteristic length and velocity in PU with corresponding variable denoted in lattice units with subscript LU. To set up the channel flow in LBM, two parameters in LBM lattice units from the choice of U_{LU}, L_{LU} and ν_{LU}. The third parameter will then be determined from Eq. (2.81). For the current example, ν_{LU} and L_{LU} is chosen to use for the initial setup by choosing a relaxation factor τ_f of 0.6 and discretizing the channel with a 256 x 256 D2Q9 model. Using Eq.

(2.30), ν_{LU} is determined to have a value of 0.033 and L_{LU} is 256 (number of nodes along the channel height). Using Eq. (2.81) the characteristic velocity U_{LU} is 0.00013021. The value of 0.00013021 is then used as inlet velocity boundary condition in conjunction with the other LBM parameters stated earlier to simulate the flow in the channel.

If after solving the flow problem for 30 lattice time units in the current example and a velocity of 0.000195 in LU is obtained in the middle of the channel. Eq. (2.81) and Eq. (2.82) can then be used to determine the centerline velocity in PU to be 0.0015 m/s at time t = 900s.

CHAPTER 3

IMMERSED BOUNDARY METHOD

3.1 Numerical Methods for Fluid Structure Interaction

Various flows of biological and engineering interest involve the interaction between complex (moving or stationary, flexible or rigid) bodies and the flow field. The interaction between the body and flow field is termed fluid structure interaction (FSI). The effect of FSI can be uni-directional or bi-directional. In bi-directional FSI, there is a two-way interaction between the flow and the immersed body that is the flow of the fluid affects the shape and/or location of the body while translated or deformed body affects the resulting flow field. Examples of bi-directional FSI are the blood flow in compliant or flexible blood vessels and the heart, deformation of red blood cells in microvessels, aquatic and bacterial locomotion, to mention a few. In uni-directional FSI, there is a one-way interaction between the body and the flow. In this case the body affects the flow field without any reciprocal deformation or displacement of the body. Examples of uni-directional FSI is the flow over rigid bluff bodies, such as cylinders. The numerical methods used for the simulation of FSI problems can be categorized based on the meshing strategy, the method used to track or capture the solid/fluid interface and the method used to enforce boundary condition at the solid/fluid interface. Categorization based on the meshing technique can result in groups using conformal and non-conformal based methods. Boundary fitted fluid meshes that conform to the shape of the immersed body boundary are used in the conformal methods. Remeshing of the fluid mesh is often necessary in order to maintain good quality fluid mesh. Example of conformal method is the arbitrary Lagrangian method (ALE) (van de Vosse et al. 2003 and Ge et al. 2007). In the non-conformal method, the fluid mesh does not align or conform to the shape of the immersed body, but rather the complex body boundary is superimposed onto the fluid mesh. For moving boundary FSI problems, the moving boundary moves in a fixed fluid mesh and eliminates re-meshing of the fluid mesh. The advantages of the non-conformal method, for stationary body (particularly for bodies with complex shape) induce the reduction of the computational effort in the iterative process of generating good quality conformal mesh during pre-processing. For moving boundary problems, non-conformal method eliminates the need for fluid grid re-meshing. Due to the inherent advantage of non-conformal method, FSI can easily be simulated in fixed grid Cartesian based fluid solvers, such as LBM. Peskin first developed the non-conformal method using the immersed boundary method (IBM) (Peskin 1972 and Peskin 1977). Examples of other numerical approaches that use non-conformal fluid mesh include volume of fluid(VOF) (Hirt et al. 1981 and Nagano et al. 2010) , level set method(LSM) (Sethian 1996 and Sethian et al. 1988) , marker- and-cell method (Harlow et al. 1970 and Glimm et al. 1985), fictitious domain method (FDM) (De Hart et al. 2003 and Bertrand et al. 1997), extended immersed boundary method (ExIBM) (Wang et al. 2004), immersed finite element method (IFEM) (Zhang et al. 2007 and Liu et al. 2006), and immersed interface method (IIM) (Leveque et al. 1994).

There are also Eulerian-Eulerian (EE) and Eulerian-Lagrangian (EL) FSI methods based on the formulation used for resolving the fluid/solid interface. In EE method, the interface is resolved using an Eulerian formulation where the evolution of the interface is solved in a stationary inertia frame. The interface is not explicitly solved or tracked in EE method therefore suitable means are used to reconstruct the interface and such methods are also called interface capturing methods. Representative EE FSI methods are the VOF and LSM where the interface is captured by using phase volume fraction and the zero level set function. EE methods are best suited for problems where there are significant geometric and topological changes in the interface such as void formation, contact, or merging which is particularly encountered in liquid-liquid systems. The diffusive nature of the approaches used in the interface reconstruction of the interface in EE FSI based methods generally leads to unsatisfactory results due to inaccuracy in resolving the fluid/solid interface. There is also the additional computational complexity associated with the reconstruction of the shape and location of the interface. In EL FSI method, the interface is explicitly tracked by placing markers or grid points on the boundary of the immersed body and it is also called interface tracking methods. The evolutions of the markers are solved using local reference frame that moves with the interface. EL based methods are able to resolve the interface properly when compared to EE based methods. Examples of EL FSI based methods are IBM, ExIBM, IIM, FDM and IFEM.

Categorization of FSI numerical methods based on enforcement of boundary conditions can be classified as sharp interface, spreading, and diffuse interface approaches (Udaykumar et al. 2001). In the sharp interface approaches, the computational stencil near the immersed boundary is modified in order to directly impose the boundary conditions at the interface, leading to a sharp interface demarcation between the solid and fluid. Representative sharp approaches are IIM, ALE, and some implementation variants of IBM called the discrete forcing IBM (Mittal 2005). The enforcement of boundary conditions in diffuse interface approaches are achieved by determining body force or source terms at the solid grid points and spreading the body force to neighboring fluid nodes using a suitable distribution kernel. Examples of diffuse interface methods are IFEM, ExIBM, and the continuous forcing type of IBM (Mittal 2005).

The immersed boundary method (IBM) is the pioneering method amongst the class of non-conformal FSI methods. IBM has also led to the development of other non-boundary-fitted methods, such as fictitious domain method, extended immersed boundary method, immersed finite element method, and immersed interface method. IBM is also an Eulerian-Lagrangian FSI method. As discussed earlier, the implementation variant of IBM determines whether it is a sharp, or diffuse interface FSI method. The ghost cell finite difference and cut cell finite volume IBM (Mittal 2005) implementation are sharp interface methods and are mostly used in high Reynolds number applications. The inclusion of moving boundary can be more difficult for IBM variants that fall under the sharp interface classification. IBM implementation variants that fall under the diffuse interface methods are the direct forcing, feedback, and the energy functional approaches. These methods are mostly suitable for low Reynolds number flows with moving or stationary flows. Due to the nature of the flows investigated in the current research, the diffuse interface implementation variant (direct forcing IBM to be specific) was used. In the next sections, the different forms of the diffuse interface IBM methods and the implementation of direct forcing IBM within the LBM computational framework will be discussed.

3.2 Diffuse Interface Immersed Boundary Method

In IBM, the solid domain Ω_s is superimposed onto an Eulerian fluid domain Ω_f as shown in Figure 3.1. The boundary of the solid domain is discretized into Lagrangian grid points (represented by the filled dots in Figure 3.1) with position vector X. The solid grid points do not have to coincide with the fluid grid points. The interaction between the body and the surrounding fluid is considered by the introduction of a body force to the fluid motion governing equations in order to enforce the boundary conditions at the solid/fluid interface.

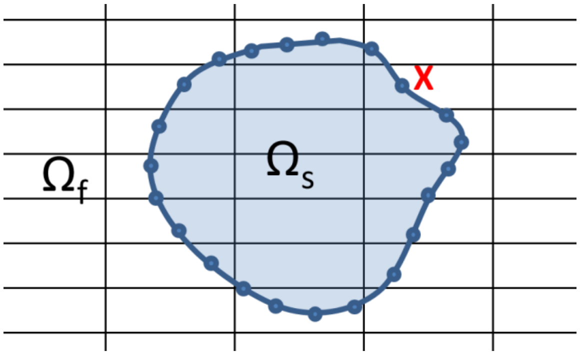

Figure 3.1 Lagrangian solid grid superimposed on the Eulerian fluid grid.

The body force $\mathbf{f}(\mathbf{X},t)$ is determined at the Lagrangian grid points and suitable transformation functions are devised to transform the body force $\mathbf{f}(\mathbf{X},t)$ from the Lagrangian solid grid point to an equivalent Eulerian body force $\mathbf{F}(\mathbf{x},t)$ in the fluid domain. The body force $\mathbf{F}(\mathbf{x},t)$ is then incorporated into the Navier Stokes equations or fluid governing equation as a source term as shown in Eq. (3.1)

$$\rho\left(\frac{\partial \mathbf{u}}{\partial \mathrm{t}}+(\mathbf{u}\bullet\nabla\mathbf{u})\right)=-\nabla \mathrm{p}+\mu\nabla^2\mathbf{u}+\mathrm{F}(\mathbf{x},\mathrm{t}) \tag{3.1}$$

The discrete Dirac delta function $\delta(\mathbf{x}-\mathbf{X})$ is typically used in IBM as the transformation function for transforming the Lagrangian body force $\mathbf{f}(\mathbf{X},\mathbf{t})$ into the Eulerian form $\mathrm{F}(\mathbf{x},\mathrm{t})$ (Peskin 2002) as shown in Eq. (3.2).

$$\mathbf{F}(\mathbf{x},t)=\int \mathbf{f}(\mathbf{X},t)\delta(\mathbf{x}-\mathbf{X})\mathbf{ds} \tag{3.2}$$

Where $\mathbf{ds}$ is the differential arc length along the boundary of the immersed solid. There are different variants of $\delta(\mathbf{x}-\mathbf{X})$ available in literature. The form of $\delta(\mathbf{x}-\mathbf{X})$ (Peskin 2002) in 2D Cartesian coordinate used in the current work is as shown in Eq. (3.3)

$$\begin{aligned}
\delta(\mathbf{x}-\mathbf{X}) &= \frac{1}{dx^2}\phi\left(\frac{x_1}{dx}\right)\phi\left(\frac{x_2}{dx}\right)\\
\phi(r) &= \frac{3-2|r|+\sqrt{1+4|r|-4r^2}}{8}(r<1)\\
\phi(r) &= \frac{5-2|r|-\sqrt{-7+12|r|-4r^2}}{8}(1\le r\le 2)
\end{aligned} \tag{3.3}$$

$$\phi(r)=0(r>2)$$

where x_1 and x_2 represents the components of $\mathbf{x}-\mathbf{X}$ in the respective coordinate direction and dx is the fluid grid spacing. The discrete delta function $\delta(\mathbf{x}-\mathbf{X})$ does not only provide a means of transforming the body force from Lagrangian to Eulerian coordinate system but it also distributes the body force to the neighboring fluid nodes.

The delta function $\delta(\mathbf{x}-\mathbf{X})$ shown in Eq. (3.3) distributes $\mathbf{f}(\mathbf{X},\mathrm{t})$ to the fluid nodes within two fluid grid spacing distance from the solid node as shown in discrete delta function distribution in Figure 3.2. The diffuse interface IBM implementation (energy functional, feedback and direct forcing) variants are similar in that the discrete Dirac delta is used in transforming and distributing the Lagrangian body force to the fluid domain, the difference between the variants is in how the body force is calculated.

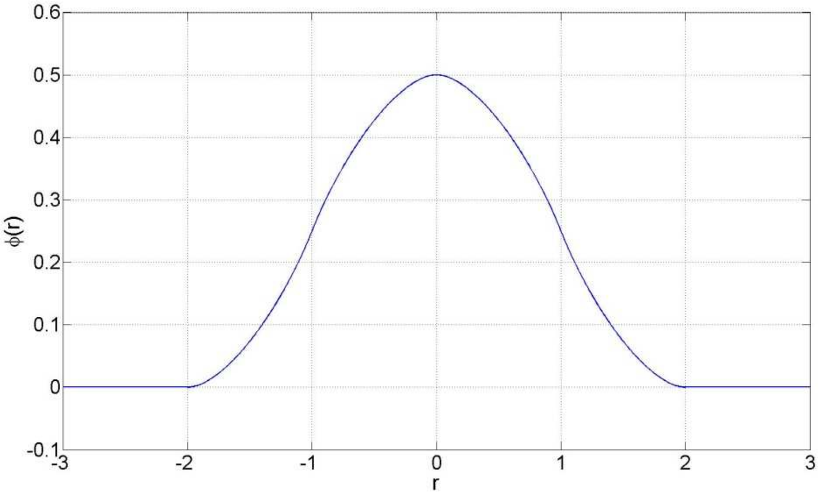

Figure 3.2 $\phi(r)$ distribution profile used in $\delta(\mathbf{x}-\mathbf{X})$ in Eq. (3.3).

3.2.1 Energy Functional IBM

The energy functional form of IBM (Peskin 2002) belongs to the class of continuous forcing approaches (Mittal 2005) used to determine the body force. The body $\mathbf{f}(\mathbf{X},\mathrm{t})$ is determined from the derivative of energy functional as shown in Eq. (3.4).

$$\mathbf{f}(\mathbf{X},\mathrm{t}) = \frac{\partial \mathrm{E}(\mathbf{X},\mathrm{t})}{\partial \mathbf{X}} \tag{3.4}$$

The energy functional can be the strain, elastic or bending energy densities. The immersed boundary is represented by a series of Lagrangian points that are connected to each other by massless elastic fibers that moves with the same local velocity as the fluid. There are also other variants of the energy functional IBM that removes the massless assumption by incorporating mass into the IBM formulation (Peskin et al. 2007). The discrete Dirac delta is used to obtain the local velocity $\mathbf{u}(\mathbf{X},\mathrm{t})$ at the solid grid point from the neighboring fluid node velocity $\mathbf{u}(\mathrm{x},\mathrm{t})$ using Eq. (3.5).

$$\frac{\partial \mathbf{X}}{\partial \mathrm{t}} = \mathbf{u}(\mathbf{X},\mathrm{t}) = \int \mathbf{u}(\mathbf{x},\mathrm{t})\delta(\mathbf{x}-\mathbf{X})\mathrm{dx} \tag{3.5}$$

The energy functional form of IBM is mainly used for immersed elastic boundaries whose energy functional and material constitutive law can easily be obtained. In order to handle immersed rigid boundaries using the energy functional IBM, the elastic fibers are assumed to obey Hooke's law with an extremely high positive stiffness constant κ (Mittal 2005). The body force is then evaluated as the restoring or penalty force required to bring the solid grid points back to its equilibrium state using Eq. (3.6).

$$\mathbf{f}(\mathbf{X},\mathrm{t}) = \kappa\left(\mathbf{X}-\mathbf{X}_{\mathrm{e}}\right) \tag{3.6}$$

$\mathbf{X}_e$ is the position vector of the solid grid points at its equilibrium or initial configuration. Using high values of κ leads to stiffness of the governing equations and causes numerical instability (Mittal 2005). Spurious elastic effects and deviations from the equilibrium state will also occur if lower values of κ is used. This usually places restriction on the application of this form of IBM to applications with rigid boundary.

3.2.2 Feedback Forcing IBM

In the feedback forcing methods, the body force $\mathbf{f}(\mathbf{X},t)$ is determined by integrating the velocity at the solid grid points with two negative large constants α and β (Saiki et al. 1996 and Goldstein et al. 1993) as shown in Eq. (3.7).

$$\mathbf{f}(\mathbf{X},t)=\alpha\int_0^t\left(\mathbf{u}(\mathbf{X},t')-\mathbf{U}_b(\mathbf{X},t')\right)dt'+\beta\left(\mathbf{u}(\mathbf{X},t)-\mathbf{U}_b(\mathbf{X},t)\right) \tag{3.7}$$

where $\mathbf{u}(\mathbf{X},t)$ is the interpolated velocity at the solid grid point and $\mathbf{U}_b(\mathbf{X},t)$ is the desired, or actual, velocity at the solid grid point. The feedback forcing provides a feedback control of the velocity at the solid point with the intention of minimizing the velocity error $(\mathbf{u}(\mathbf{X},t)-\mathbf{U}_b(\mathbf{X},t))$. The two large constants α and β render Eq. (3.7) stiff and place the requirement of small time steps on the numerical integration. A wrong choice of these constant can lead to numerical instability particularly for unsteady flows (Mittal 2005). There is also no selection criteria used in determining the optimum choice of the constants that will ensure numerical stability, ad-hoc judgments are needed in most cases.

3.2.3 Direct Forcing IBM

The direct forcing IBM (Mohd-Yusof 1997) eliminates the numerical instability encountered by both the energy functional and feedback forcing IBM by eliminating the large constants used in determining $\mathbf{f}(\mathbf{X},t)$ from previously discussed approaches. The body force is determined directly by solving Eq. (3.8) at the solid grid points.

$$\mathbf{f}(\mathbf{X},t) = -\left(\frac{\left(\mathbf{U}_b(\mathbf{X},t) - \mathbf{u}(\mathbf{X},t)\right)}{dt} + \left(\mathbf{u} \bullet \nabla\right)\mathbf{u} \right) + \frac{1}{\rho}\nabla P - \nu\nabla^2\mathbf{u} \tag{3.8}$$

$\mathbf{U}_b(\mathbf{X},t)$ represents the desired velocity on the boundary of the immersed body while the interpolated velocity $\mathbf{u}(\mathbf{X},t)$ is obtained from the neighboring fluid velocity $\mathbf{u}(\mathbf{x},\mathbf{t})$. The body force $\mathbf{f}(\mathbf{X},t)$ can be viewed as an artificial or penalty forcing required to achieve the desired flow velocity on the surface of the body. The interpolated velocity $\mathbf{u}(\mathbf{X},t)$ is obtained in the current work by using a bilinear interpolation from the neighboring fluid nodes. In Figure 3.3 representative solid nodes on the boundary of the solid are shown with blue filled circles with the velocity of the neighboring fluid nodes denoted by $u_1(\mathbf{x},t)$, $u_2(\mathbf{x},t)$, $u_3(\mathbf{x},t)$ and $u_4(\mathbf{x},t)$. Referring to the nomenclature in Figure (3.3), the bilinear interpolation used to obtain velocity $\mathbf{u}(\mathbf{X},t)$ in the current work is as shown in Eq. (3.9).

$$\mathbf{u}(\mathbf{X},t)=\frac{1}{\Delta x\Delta y}\begin{bmatrix}\mathbf{u}_1(\mathbf{x},t)\Delta x_b\Delta y_b+\mathbf{u}_2(\mathbf{x},t)\Delta x_b\Delta y_f+\\ \mathbf{u}_3(\mathbf{x},t)\Delta x_f\Delta y_f+\mathbf{u}_4(\mathbf{x},t)\Delta x_f\Delta y_b\end{bmatrix} \tag{3.9}$$

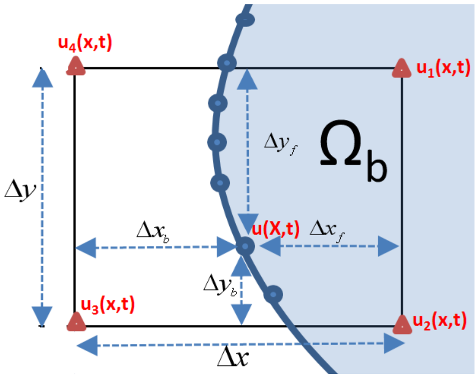

Figure 3.3 Schematic of bilinear interpolation at solid grid point.

3.3 Direct Forcing Lattice Boltzmann Immersed Boundary Method

The inherent advantage of using a fixed fluid mesh in IBM enhances the computational efficiency and accuracy of Cartesian mesh-based numerical schemes like LBM in handling complex and moving boundaries. The direct forcing IBM was incorporated into the LBM computational framework in the current work and the combined approach is called IB-LBM. In order to implement the IB-LBM, the Lagrangian body force $\mathbf{f}(\mathbf{X},t)$ is determined from the direct forcing equation shown in Eq. (3.8) in conjunction with the bilinear interpolation equation (Eq. (3.9)). The Eulerian body force $\mathbf{F}(\mathbf{x},t)$ is then obtained from $\mathbf{f}(\mathbf{X},t)$ using Eq. (3.2). The Eulerian body force $\mathbf{F}(\mathbf{x},t)$ is then incorporated in to the RHS of LBE (Eq. (2.28)) as a source term. The LBE with the inclusion of a body force or source term (Guo et al. 2002) can be written as

$$f_i(\mathbf{x}+\mathbf{e_i}\Delta t, t+\Delta t) = f_i(\mathbf{x},t) - \frac{1}{\tau_f}\left(f_i(\mathbf{x},t) - f_i^{eq}(\mathbf{x},t)\right) + \Delta t F_i \tag{3.10}$$

where F_i is the Eulerian body force along the i$^{\text{th}}$ direction of the LBM lattice structure. The body force F_i is determined from $\mathbf{F}(\mathbf{x},t)$ using Eq. (3.11) (Guo et al. 2002).

$$F_i = \left(1 - \frac{1}{2\tau_f}\right)\omega_i \left[\frac{\mathbf{e}_i - \mathbf{u}}{c_s^2} + \frac{(\mathbf{e}_i \bullet \mathbf{u})}{c_s^4}\mathbf{e}_i\right] \bullet \mathbf{F}(\mathbf{x},t) \tag{3.11}$$

In addition to adding the body force to the LBE, IB-LBM also added as a momentum source to the macroscopic velocity equation (Eq. (2.28)) (Guo et al. 2002), which Eq. (2.28) is modified to account for the body force yields Eq. (3.12)

$$\sum f_i\, \mathbf{e_i} + \frac{\Delta t}{2}\mathbf{F}(\mathbf{x},t) = \rho\mathbf{u} \tag{3.12}$$

CHAPTER 4

DIRECT HEATING IMMERSED BOUNDARY LATTICE BOLTZMANN METHOD

4.1 Lattice Boltzmann Method Thermal Models

The thermal LBM is still a developing and maturing field when compared with the hydrodynamic or isothermal LBM. The major thermal LBM approaches used for thermal flow simulations can be categorized as multispeed approach (MSA) or single population approach, passive scalar approach (PSA) and thermal energy approach (TEA) or double population approach. The multispeed approach uses the same PDF to model the macroscopic variables of density, velocity, pressure and temperature by increasing the number of discrete speeds of the lattice structure. The PSA and the TEA on the other hand uses different PDF to model the temperature and internal energy respectively. The original formulation of PSA assumes negligible viscous dissipation and compression work. The application of IBM to the LBM computation of thermal flows is close to non-existence despite the practical and engineering importance of heat transfer over immersed boundaries. In the following sections, the different thermal LBM models are discussed and a new direct heating IB-LBM is developed and introduced for thermal flow problems with immersed bodies. The direct heating IB-LBM was developed for both Neumann (constant heat flux) and Dirichlet (constant temperature) boundary conditions. A novel and simple method of handling the Neumann boundary conditions and the calculation of the Nusselt number is introduced for IBM.

4.1.1 Multispeed Approach (MSA) LBM

In MSA thermal LBM, the same PDF is used for momentum and energy transport (McNamara et al. 1993; Alexander et al. 1993 and Chen et al. 1994). The recovery of the macroscopic thermal variables of temperature requires the addition of additional discrete particle speed into the lattice structure. For instance, the D2Q9 model needs four additional speeds, which makes a total of thirteen speeds in a MSA formulation. Higher order moments of the PDF are also needed in determining the temperature T or internal energy E as shown in Eq. (4.1)

$$\rho E = \tfrac{1}{2}\sum_i f_i \left(\mathbf{e}_i - \mathbf{u}\right)^2 \tag{4.1}$$

$$E = \frac{D_o k_b T}{2} = \frac{D_o RT}{2N_A} \tag{4.2}$$

where k_b and N_A is the Boltzmann constant and Avogadro's number. In order to satisfy local energy conservation, third order velocity terms of $\left(\mathbf{e}_i \bullet \mathbf{u}\right)^3$, $\left(\mathbf{e}_i \bullet \mathbf{u}\right)u^2$ and u^3 are included in the EDF(Eq. (2.26)) to obtain the generic form shown in Eq. (4.3). The collision operator $\mathbf{\Omega}_i$ must also satisfy the constraint in Eq. (4.4)

$$f_i^{eq} = \rho w_i \left[1 + a(\mathbf{e}_i \bullet \mathbf{u}) + b(\mathbf{e}_i \bullet \mathbf{u})^2 + c\left(\mathbf{u} \bullet \mathbf{u}\right) + d\left(\mathbf{e}_i \bullet \mathbf{u}\right)^3 + e\left(\mathbf{e}_i \bullet \mathbf{u}\right)u^2 + ju^3\right] \tag{4.3}$$

$$\frac{\Omega_i e_i^2}{2} = 0 \tag{4.4}$$

where a, b, c, d, e and j are model constants determined from the choice of the lattice structure. The MSA thermal LBM have the limitation of simulating a narrow temperature range due to the small number of additional discrete speeds used for the modeling the energy transport (Chen et al. 1998). The MSA also assumes that the momentum and thermal modes relaxes to equilibrium at the same rate hence the Prandtl number is fixed or a constant (Chen et al. 1998). Most MSA thermal LBM also suffers from numerical instability which is attributed to the lack of an H- therorem (Chen et al. 1998). The limitation of the fixed Prandtl number can be relieved by the use of a two-time relaxation operator (Chen et al. 1997). Several attempts have also been made in order to resolve the numerical instability, among such attempts are the introduction of temperature dependent factor in the EDF (Teixeira et al. 2000), this attempt enhances the numerical instability but introduces artificial thermal diffusion. Other attempts such as using extra moment and discrete speeds (Chen et al. 1994), using Lax-Wendroff advection to achieve adjustable time stepping have been used to increase the numerical stability (McNamara et al. 1995 and McNamara et al. 1997). Despite all of these attempts, marginal improvements were made with regards to the numerical stability and this is a major limitation of the MSA thermal LBM.

4.1.2 Thermal Energy Approach (TEA) LBM

In addition to the PDF f used for the momentum transport, the TEA thermal LBM introduces another PDF h to model the internal energy transport (He, 1998). The internal energy PDF h is related to the hydrodynamic PDF f as shown in Eq. (4.5)

$$h=\frac{(\boldsymbol{\xi}-\mathbf{u})^2}{2}f \tag{4.5}$$

From the Boltzmann equation, the internal energy transport can be written as

$$\frac{\partial h}{\partial t}+(\boldsymbol{\xi}\bullet\nabla)h=\frac{(\boldsymbol{\xi}-\mathbf{u})^2}{2}\Omega(f)-fq \tag{4.6}$$

$$q=(\boldsymbol{\xi}-\mathbf{u})\bullet\left(\frac{\partial\mathbf{u}}{\partial t}+(\boldsymbol{\xi}\bullet\nabla)\mathbf{u}\right) \tag{4.7}$$

where q is the heat dissipation term. A new collision operator $\boldsymbol{\Omega}^h$ for the PDF h can be expressed as

$$\Omega^h=\frac{(\boldsymbol{\xi}-\mathbf{u})^2}{2}\Omega(f)=-\frac{h-h^{eq}}{\tau_h} \tag{4.8}$$

where h^{eq} and τ_h is the EDF and relaxation factor for the internal energy PDF g. Using the Chapman-Enskog expansion (Chapman et al. 1970) to perform a multi-scale expansion of the PDF f and h , time and space with its associated derivatives yields Eq. (4.9) (showing details for only PDF h)

$$h=h^{eq}+\varepsilon h^{(1)}+\varepsilon^2 h^{(2)}+O(\varepsilon^3) \tag{4.9}$$

The first order Chapman-Enskog expansion of Eq. (4.6) yields

$$\frac{\partial h^{eq}}{\partial t_0}+(\boldsymbol{\xi}\bullet\nabla_1)h^{eq}=-\frac{h^{(1)}}{\tau_h}-f^{eq}q \tag{4.10}$$

where ∇_1 is the first order spatial derivatives of the Chapman-Enskog expansion and t_0 is the zeroth order expansion in time. Taking the integral of the Eq. (4.10) over the velocity phase space $\boldsymbol{\xi}$ to obtain Eq. (4.11).

$$\frac{\partial(\rho E)}{\partial t_0}+(\rho\mathbf{u}E)\bullet\nabla_1=-p(\nabla_1\bullet\mathbf{u}) \tag{4.11}$$

The RHS of Eq. (4.11) is the work done due to compression by the pressure. Similarly the second order Chapman-Enskog expansion of Eq. (4.6) yields

$$\frac{\partial h^{eq}}{\partial t_1}+\left[\frac{\partial}{\partial t_0}+(\boldsymbol{\xi}\bullet\nabla_1)\right]h^{(1)}=-\frac{h^{(2)}}{\tau_h}-f^{(1)}q \tag{4.12}$$

$$f^{(1)}=-\tau_f\left[\frac{\partial f^{eq}}{\partial t_0}+\nabla_1\bullet(\boldsymbol{\xi}f^{eq})\right] \tag{4.13}$$

where t_1 is the first order expansion in time. Substituting Eq. (4.13), $h^{(1)}$ in Eq. (4.10) into Eq. (4.12) and taking the integral in velocity space yields

$$\frac{\partial(\rho E)}{\partial t_1}=(\rho\kappa\nabla E)\bullet\nabla_1+\Pi:\nabla\mathbf{u} \tag{4.14}$$

$$\kappa=\frac{(D_o+2)\tau_f RT}{D_o} \tag{4.15}$$

where the $\Pi : \nabla \mathbf{u}$ and κ are the viscous dissipation and thermal conductivity of the fluid. The energy equation can be obtained by combining the first order term (Eq. (4.11)) and the second order term (Eq. (4.15))

$$\frac{\partial(\rho E)}{\partial t} + (\rho \mathbf{u} E) \bullet \nabla = -p(\nabla_1 \bullet \mathbf{u}) + (\rho \kappa \nabla E) \bullet \nabla + \Pi : \nabla \mathbf{u} \tag{4.16}$$

In order to avoid inconsistency of viscosity between the isothermal LBM and the TEA thermal model and also to keep the numerical scheme explicit, the hydrodynamic PDF f is modified into the PDF $\overline{f}$ where $\overline{f}$ is as defined in Eq. (4.17)

$$\overline{f} = f + \frac{\Delta t}{2\tau_f}\left(f - f^{eq}\right) - \frac{\Delta t}{2}\left(\frac{\mathbf{G} \bullet (\xi - \mathbf{u})}{RT}\right) f^{eq} \tag{4.17}$$

where $\mathbf{G}$ is the external force per unit mass acting on the system. The time discretized evolution equation for the modified hydrodynamic PDF $\overline{f}$ is then given by

$$\begin{aligned} \overline{f}(\mathbf{x} + \xi \Delta t, \xi, t + \Delta t) = \overline{f}(\mathbf{x}, \xi, t) - \frac{\Delta t}{\tau_f + 0.5\Delta t}\left[\overline{f}(\mathbf{x}, \xi, t) - f^{eq}(\mathbf{x}, \xi, t)\right] + \\ \left(\frac{\tau_f \Delta t}{\tau_f + 0.5\Delta t}\right)\left(\frac{\mathbf{G} \bullet (\xi - \mathbf{u})}{RT}\right) f^{eq} \end{aligned} \tag{4.18}$$

In order to obtain the modified LBE, the velocity phase space must also be discretized in Eq. (4.18). Using the Gauss-Hermite quadrature and similarly following the same procedures as outlined in sections 2.3 and 2.4, the LBE for the modified hydrodynamic PDF $\overline{f}$ in the TEA thermal LBM yields

$$\overline{f}_i\left(\mathbf{x}+\mathbf{e}_i\Delta t,t+\Delta t\right)=\overline{f}_i\left(\mathbf{x},t\right)-\frac{\Delta t}{\tau_f+0.5\Delta t}\left[\overline{f}_i\left(\mathbf{x},t\right)-f_i^{eq}\left(\mathbf{x},t\right)\right]+ \left(\frac{\tau_f\Delta t}{\tau_f+0.5\Delta t}\right)\left(\frac{\mathbf{G}\bullet\left(\mathbf{e}_i-\mathbf{u}\right)}{RT}\right)f_i^{eq} \tag{4.19}$$

The macroscopic variables of density and velocity in MSA thermal LBM are obtained from the moment of PDF $\overline{f}$ as shown in Eq. (4.20)-(4.21)

$$\sum\overline{f}_i=\rho \tag{4.20}$$

$$\sum\overline{f}_i\mathbf{e}_i+\frac{\rho\mathbf{G}\Delta t}{2}=\rho\mathbf{u} \tag{4.21}$$

Similarly, the internal energy PDF h is modified to $\overline{h}$ as shown in Eq. (4.22) in order to maintain the explicitness of LBM

$$\overline{h}=h+\frac{\Delta t}{2\tau_h}\left(h-h^{eq}\right)+\frac{\Delta t}{2}fq \tag{4.22}$$

The time discretized evolution equation for the modified thermal PDF $\overline{h}$ is then given as

$$\bar{h}\left(\mathbf{x}+\xi\Delta t,\xi,t+\Delta t\right)=\bar{h}\left(\mathbf{x},\xi,t\right)-\frac{\Delta t}{\tau_h+0.5\Delta t}\left[\bar{h}\left(\mathbf{x},\xi,t\right)-h^{eq}\left(\mathbf{x},\xi,t\right)\right]- \left(\frac{\tau_h\Delta t}{\tau_h+0.5\Delta t}\right)f\left(\mathbf{x},\xi,t\right)q\left(\mathbf{x},\xi,t\right) \tag{4.23}$$

The LBE for the thermal PDF $\bar{h}$ can be obtained by discretizing the velocity phase space and using Gauss-Hermite quadrature to obtain the TEA thermal LBE as shown in Eq. (4.24)

$$\bar{h}_i\left(\mathbf{x}+\mathbf{e}_i\Delta t,t+\Delta t\right)=\bar{h}_i\left(\mathbf{x},t\right)-\frac{\Delta t}{\tau_h+0.5\Delta t}\left[\bar{h}_i\left(\mathbf{x},t\right)-h_i^{eq}\left(\mathbf{x},t\right)\right]- \left(\frac{\tau_h\Delta t}{\tau_h+0.5\Delta t}\right)f_i(\mathbf{x},t)q_i(\mathbf{x},t) \tag{4.24}$$

$$q_i(\mathbf{x},t)=\left(\mathbf{e}_i-\mathbf{u}\right)\bullet\left[\frac{1}{\rho}\left(-\nabla p+\nabla\bullet\Pi\right)+\left(\mathbf{e}_i-\mathbf{u}\right)\bullet\nabla\mathbf{u}\right] \tag{4.25}$$

For a D2Q9 lattice structure, the EDF h_i^{eq} is expressed as

$$h_i^{eq}=\begin{cases}-\dfrac{2\rho E}{3e^2}\mathbf{u}\bullet\mathbf{u}\ ,\ i=0\\ \dfrac{\rho E}{9}\left[1.5+\dfrac{3}{2e^2}(\mathbf{e}_i\bullet\mathbf{u})+\dfrac{9}{2e^4}(\mathbf{e}_i\bullet\mathbf{u})^2-\dfrac{3}{2e^2}\mathbf{u}\bullet\mathbf{u}\right],\ i=1,3,5,7\\ \dfrac{\rho E}{36}\left[3+\dfrac{6}{e^2}(\mathbf{e}_i\bullet\mathbf{u})+\dfrac{9}{2e^4}(\mathbf{e}_i\bullet\mathbf{u})^2-\dfrac{3}{2e^2}\mathbf{u}\bullet\mathbf{u}\right],\ i=2,4,6,8\end{cases} \tag{4.26}$$

The internal energy E is then determined as the zeroth order moment with the inclusion of the viscous dissipation and work done by compression as shown in Eq. (4.27).

$$\rho E = \sum \bar{h}_i - \frac{\Delta t}{2} \sum q_i \left(\frac{\tau_f \bar{f}_i + 0.5 \Delta t f_i^{eq} + 0.5 \Delta t \tau_f Y_i}{\tau_f + 0.5 \Delta t} \right) \tag{4.27}$$

$$Y_i = \left(\frac{\mathbf{G} \bullet (\mathbf{e}_i - \mathbf{u})}{RT} \right) f_i^{eq} \tag{4.28}$$

The TEA thermal LBM consists of Eq. (4.24), (4.26) and (4.27). The TEA thermal model provides a suitable approach for modeling realistic thermal flow problems. However, the simplicity of LBM in terms of implementation and application of boundary conditions (bounce-back rule) is lost in TEA. The implementation simplicity is lost due to the complicated gradient operator (Eq. 4.25) appearing in Eq. (4.24). The bounce back boundary conditions is not easily applied in the TEA thermal model because the evolution equations (Eq. (4.19) and (4.24)) are for the modified PDF $\bar{f}$ and $\bar{h}$ while the bounce back rule is to be applied to the original PDF f and h. In order to make the TEA approach simpler, the complicated gradient operator q_i, which models the viscous dissipation and compression work, was dropped (Peng et al. 2003). The simplified TEA makes the implementation simple and amenable to the traditional bounce-back boundary conditions since the evolution equation is in terms of the original PDF f and h. The simplified TEA thermal model then simplifies to

$$h_i(\mathbf{x} + \mathbf{e}_i \Delta t, t + \Delta t) = h_i(\mathbf{x}, t) - \frac{\left[h_i(\mathbf{x}, t) - h_i^{eq}(\mathbf{x}, t) \right]}{\tau_h} \tag{4.29}$$

The simplified TEA model was validated for natural convection in a square cavity over a wide range of Rayleigh number and gave accurate and comparable results to the TEA model with less computational effort (Peng 2003). The TEA model can also be simplified by substituting the complicated gradient operator q_i with a forcing term Z_i to account for the viscous dissipation effect (D'Orazio 2004). The D'Orazio's TEA model has the form

$$h_i\left(\mathbf{x}+\mathbf{e}_i\Delta t, t+\Delta t\right)=h_i\left(\mathbf{x},t\right)-\frac{\Delta t}{\tau_h+0.5\Delta t}\left[h_i\left(\mathbf{x},t\right)-h_i^{eq}\left(\mathbf{x},t\right)\right]- \left(\frac{\tau_h\Delta t}{\tau_h+0.5\Delta t}\right)f_i(\mathbf{x},t)Z_i \tag{4.30}$$

$$Z_i=\frac{\left(\mathbf{e}_i-\mathbf{u}(\mathbf{x},t)\right)\bullet\left(\mathbf{u}(\mathbf{x}+\mathbf{e}_i\Delta t,t+\Delta t)-\mathbf{u}(\mathbf{x},t)\right)}{\Delta t} \tag{4.31}$$

The internal energy E in D'Orazio's TEA model is then obtained as shown in Eq. (4.32).

$$\rho E=\sum h_i-\frac{\Delta t}{2}\sum Z_i f_i \tag{4.32}$$

4.1.3 Passive Scalar Approach (PSA) LBM

The PSA thermal model describes the temperature evolution as a passive scalar that is advected by the fluid and assumes negligible viscous dissipation and compression work in the limit of small Brinkman number (Shan 1997). The PSA model was introduced to overcome the shortcomings (numerical instability) of the MSA thermal model. The PSA model (Shan 1997) predates the TEA (He et al. 1998) approach discussed earlier with the TEA introduced later in order to account for viscous dissipation and compression work that is assumed negligible in PSA model. Due to the negligible viscous dissipation and compression work assumption, the temperature is advected by the fluid and is governed by the advection-diffusion equation. Prior to the development of the PSA model, Shan et al. 1993 had developed a multi-component and multiphase LBM with interparticle interaction for mass transfer applications that is also governed by the advection-diffusion equation (Shan et al. 1993). Due to the analogy between mass and heat transfer, the Shan multi-component and multiphase LBM was extended for thermal or heat transfer applications with the interaction potential between the fluid phases or components set to zero (Shan 1997). Like the TEA, PSA model introduces an additional PDF h_i for the temperature evolution (Shan 1997) and is governed by Eq. (4.33).

$$h_i(\mathbf{x}+\mathbf{e_i}\Delta t, t+\Delta t) = h_i(\mathbf{x},t) - \frac{1}{\tau_h}\left(h_i(\mathbf{x},t) - h_i^{eq}(\mathbf{x},t)\right) \tag{4.33}$$

The temperature T is obtained as a zero order moment of the PDF h_i as shown in Eq. (4.34).

$$\sum h_i = T \tag{4.34}$$

Using a D2Q9 model, the EDF h_i^{eq} can be expressed in the form shown in Eq. (4.35) where the weights w_i are similar to its hydrodynamic counterpart (see Table 2.1).

$$h_i^{eq} = Tw_i \left[1 + \frac{3}{e^2}(\mathbf{e_i} \bullet \mathbf{u}) + \frac{9}{2e^4}(\mathbf{e_i} \bullet \mathbf{u})^2 - \frac{3}{2e^2}\mathbf{u} \bullet \mathbf{u} \right] \qquad (4.35)$$

The PSA offers better and superior numerical stability when compared to the MSA thermal LBM model and its implementation is simpler than the original TEA model. The PSA model also offers the benefit of an adjustable Prandtl number Pr when compared to a fixed Pr for MSA model. The Pr is adjusted by selecting appropriate hydrodynamic and thermal relaxation factors to the desired value. The shortcoming of the PSA is the assumption of negligible viscous dissipation and compression work. This shortcoming was recently solved by introducing the viscous dissipation as a heat source term in the PSA model (Mai et al. 2010). The appeal of the new PSA model is that in obtaining the viscous dissipation, the strain rate tensor is obtained from second order moment the non-equilibrium PDF without evaluating spatial derivatives thereby simplifying the determination of the viscous dissipation term. The PSA model was used in the current work.

4.2 Direct Heating Immersed Boundary Lattice Boltzmann Method Implementation

The application of IBM within the context of the LBM for isothermal flows has been successfully applied to moving and stationary immersed bodies with complex boundaries and there are a plethora of applications in literature. However, limited studies have been done for immersed boundary problems for thermal flow applications within the IB-LBM computational framework. The heat transfer of bodies with either stationary or moving boundary is of practical engineering and biological interest. The feedback forcing and heating approach was recently introduced within the LBM framework and simulation was done for natural convection in a square cavity with square and circular cylinders with constant temperature boundary conditions (Jeong et al. 2010). In their work, the TEA thermal LBM model was used. The no-slip boundary condition was enforced by the introduction of the body force terms into the hydrodynamic PDF. The body force term is determined from the feedback forcing using Eq. (3.7) as discussed in previous chapter. The constant temperature boundary condition was enforced by introducing a heat source into the internal energy PDF. The heat source term $h(\mathbf{X},t)$ at the Lagrangian node was determined using a feedback heating approach as shown in Eq. (4.36).

$$h(\mathbf{X},t)=\alpha_h\int_0^t\left(\Theta(\mathbf{X},t')-E_b(\mathbf{X},t')\right)dt'+\beta_h\left(\Theta(\mathbf{X},t)-E_b(\mathbf{X},t)\right) \tag{4.36}$$

Where Θ is the interpolated internal energy at the Lagrangian node obtained from the neighboring or surrounding nodes. The internal energy E_b is the desired internal energy at the Lagrangian node. The quantity α_h and β_h are negative constants. The usage of the feedback forcing and heating for thermal IB-LBM further complicates the choice of the arbitrary constants that has to be used in evaluating the body force and heat source terms. The number of constants increases to four, two (α_h and β_h) for determining the body force and two (α_h and β_h) for the heat source term. As discussed in previous section the choices of these constants are not physically based but require ad-hoc judgment in choosing it. Wrong choices of these constants lead to numerically instability. In light of these limitations of the feedback heating approach, a new direct heating approach for thermal flows within the context of the LBM computational framework is developed. The developed direct heating approach will eliminate the need of using of any arbitrary constants for evaluation of the heat source. The direct heating approach will be developed for both Neumann (constant heat flux) and Dirichlet (constant temperature) boundary conditions. A new implementation of the Neumann boundary condition and calculation of the local Nusselt number was also developed. Recently a direct heating approach was also introduced within the LBM computational framework (Kang et al. 2011) using the TEA thermal LBM model and was applied for constant temperature boundary condition and natural convection cases. However the current work differs from the work of Kang et al. 2011 in that the direct heating was applied for both constant temperature and heat flux boundary conditions with applications to both natural and forced convection thermal flow problems. The other major difference and contribution of the current work as mentioned earlier is the introduction of a new method of implementing the constant heat flux boundary condition and calculation of the local Nusselt number within the IBM. In order to develop the direct heating IB-

LBM, an Eulerian heating source term H_i is added to the PSA equation (Eq. 4.33) and can be written as

$$h_i(\mathbf{x}+\mathbf{e_i}\Delta t, t+\Delta t) = h_i(\mathbf{x},t) - \frac{1}{\tau_h}\left(h_i(\mathbf{x},t) - h_i^{eq}(\mathbf{x},t)\right) + \Delta t H_i \tag{4.37}$$

The heat source term H_i is the heat source term along the i^{th} direction of the LBM lattice structure. The summation of directional heat source term H_i about all the lattice directions at a fluid node should equal to the heat source term $H(\mathbf{x},t)$ as shown in Eq. (4.38). The directional heat source H_i is obtained from Eq. (4.39).

$$H(\mathbf{x},t) = \sum_i H_i \tag{4.38}$$

$$H_i = \omega_i\left[1 + \frac{\mathbf{e}_i \bullet \mathbf{u}}{c_s^2}\left(1 - \frac{1}{2\tau_h}\right)\right]H(\mathbf{x},t) \tag{4.39}$$

Taking a Taylor series expansion of the left hand side of Eq. (4.37) yields

$$\begin{aligned} h_i(\mathbf{x}+\mathbf{e_i}\Delta t, t+\Delta t) = h_i(\mathbf{x},t) + \Delta t D_i h_i(\mathbf{x},t) + \\ \frac{\Delta t^2}{2} D^2{}_i h_i(\mathbf{x},t) + O(\Delta t^3, \Delta x^3) \end{aligned} \tag{4.40}$$

$$D_i = \left(\frac{\partial}{\partial t} + \mathbf{e}_i \bullet \frac{\partial}{\partial \mathbf{x}}\right) \tag{4.41}$$

Using the Chapman-Enskog multiscale expansion of the PDF h_i and heat source term H_i yields Eq. (4.42) and (4.44). There is also the constraint that the summation of all the non-equilibrium PDF about a node is zero as shown in Eq. (4.43).

$$h_i = h_i^{eq} + \varepsilon h_i^{(1)} + \varepsilon^2 h_i^{(2)} + O(\varepsilon^3) \tag{4.42}$$

$$\sum_i h_i^{(n)} = 0 \tag{4.43}$$

$$H_i = \varepsilon H_i^{(1)} \tag{4.44}$$

Substituting Eq.(4.40) into Eq.(4.37) yields

$$\Delta t D_i h_i(\mathbf{x},t) + \frac{\Delta t^2}{2} D^2{}_i h_i(\mathbf{x},t) = -\frac{1}{\tau_h}\left(h_i(\mathbf{x},t) - h_i^{eq}(\mathbf{x},t)\right) + \Delta t H_i \tag{4.45}$$

Substituting Eq. (4.42) and Eq. (4.44) into Eq. (4.45) and collecting terms to first and second order of ε

$$O(\varepsilon) : \Delta t\left\{D_{1i} h_i^{eq}\right\} = -\frac{1}{\tau_h} h_i^{(1)} + \Delta t H_i^{(1)} \tag{4.46}$$

$$O(\varepsilon^2) : \Delta t\left(D_{2i} h_i^{eq}\right) + \Delta t\left(D_{1i} h_i^{(1)}\right) + \frac{\Delta t^2}{2}\left(D_{1i}^2 h_i^{eq}\right) = -\frac{1}{\tau_h} h_i^{(2)} \tag{4.47}$$

$$D_{\alpha i} = \left(\frac{\partial}{\partial t_\alpha} + \mathbf{e}_i \bullet \frac{\partial}{\partial \mathbf{x}_\alpha}\right) \tag{4.48}$$

$$D_{\alpha i}^2 = \left(\frac{\partial}{\partial t_\alpha} + \mathbf{e}_i \bullet \frac{\partial}{\partial \mathbf{x}_\alpha}\right)^2 \tag{4.49}$$

Substituting Eq. (4.46) into the second order spatial and time derivatives in Eq. (4.47) and simplifying further to obtain Eq. (4.50)

$$O(\varepsilon^2): \Delta t\left(D_{2i}h_i^{eq}\right) - \Delta t\left\{1-\frac{1}{2\tau_h}\right\}\left(D_{1i}h_i^{(1)}\right) = -\frac{1}{\tau_h}h_i^{(2)} - \frac{\Delta t^2}{2}D_{1i}H_i^{(1)} \tag{4.50}$$

Summing over all lattice directions *i* in Eq. (4.46) and (4.50) with the relations in Eq. (4.42)-(4.44) to obtain Eq. (4.51) where σ is direction in the respective Cartesian coordinate system.

$$\frac{\partial\left(\sum_i\left[h_i^{eq}+\frac{\Delta t}{2}H_i\right]\right)}{\partial t}+\frac{\partial\left(\sum_i e_{i\sigma}\left[h_i^{eq}+\frac{\Delta t}{2}H_i\right]\right)}{\partial x_\sigma}=\frac{\partial}{\partial x_\sigma}\left(\sum_i\left[1-\frac{1}{2\tau_h}\right]e_{i\alpha}h_i^{(1)}\right)+\sum_i H_i \tag{4.51}$$

The first term and second terms on left hand side of Eq. (4.51) models the temporal term and convective terms of the temperature field T. The first on the right hand side of Eq. (4.51) models the thermal diffusion or heat conduction while the second term models the heat source. The temperature field T is obtained as a zero-order moment of the thermal PDF with the inclusion of the heat source term as shown in Eq. (4.52). The convection term is obtained as the first order moment of the EDF and the heat source terms as shown in Eq. (4.53). The heat conduction q is obtained as the first order moment of the non-equilibrium PDF (Eq. (4.54)).

$$\sum h_i^{eq}+\frac{\Delta t}{2}H(\mathbf{x},t)=T \tag{4.52}$$

$$\sum_i e_{i\sigma}\left[h_i^{eq}+\frac{\Delta t}{2}H_i\right]=u_\sigma T \tag{4.53}$$

$$\left(\sum_i\left[1-\frac{1}{2\tau_h}\right]e_{i\sigma}h_i^{(1)}\right)=q \tag{4.54}$$

The heat conduction q in Eq. (4.54) can be simplified in terms of the EDF to Eq. (4.55)

$$\alpha\frac{\partial}{\partial x_\sigma}\left[\sum_i\left(h_i^{eq}+\frac{\Delta t}{2}H_i\right)\right]=\left(\sum_i\left[1-\frac{1}{2\tau_h}\right]e_{i\sigma}h_i^{(1)}\right)=q \tag{4.55}$$

$$\alpha=c_s^2\Delta t\left(\tau_h-{}^1\!/_2\right) \tag{4.56}$$

where α is the thermal diffusivity. Substituting Eq. (4.51), Eq. (4.52), (4.54) and (4.38) into Eq. (4.50) obtains the macroscopic energy equation without the viscous heating and dissipative terms as shown in Eq. (4.57)

$$\left(\frac{\partial T}{\partial t}+\mathbf{u}\bullet\nabla T\right)=\alpha\nabla^2 T+H(\mathbf{x},t) \tag{4.57}$$

The Prandtl number Pr which is the ratio of the momentum diffusivity to thermal diffusivity is given by Eq. (4.58)

$$\Pr=\frac{\nu}{\alpha}=\frac{2\tau_f-1}{2\tau_h-1} \tag{4.58}$$

The heating source $H(\mathbf{x},t)$ that is obtained by the newly formulated direct heating approach is to be used in Eq. (4.37), (4.39) using the newly formulated direct heating approach. The determination of the heat source $H(\mathbf{x},t)$ will depend on the type of boundary condition that is to be enforced on the immersed boundary. The following section will address the implementation for the Dirichlet (constant temperature) and Neumann (constant heat flux) boundary conditions using the direct heating IB-LBM.

4.2.1 Direct Heating IB-LBM for Constant Temperature Boundary Condition

A sketch showing the isothermal immersed body Ω_b with temperature T_b is shown in Figure 4.1. The Lagrangian solid nodes are shown with the blue circle markers with temperature $T(\mathbf{X},t)$. The surrounding or neighboring fluid nodes are shown with the red triangle markers.

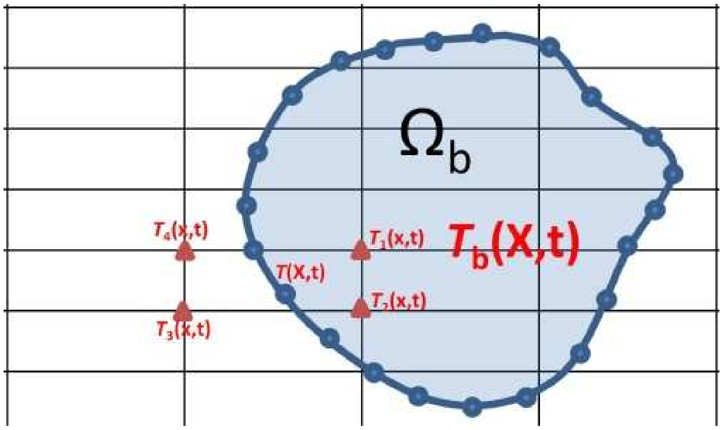

Figure 4.1 Schematic of the immersed body for constant temperature boundary condition.

For the Cartesian grid, four nodes that are the nearest neighbors of a solid node with temperatures $T_1(\mathbf{x},t)$, $T_2(\mathbf{x},t)$, $T_3(\mathbf{x},t)$ and $T_4(\mathbf{x},t)$ can be identified as shown in Figure 4.1. The temperature $T(\mathbf{X},t)$ are obtained from the neighboring four fluid nodes using bilinear interpolation with Eq. (4.59) with all the nomenclature of all variables used in the interpolation defined in Figure 4.2.

$$T(\mathbf{X},t)=\frac{1}{\Delta x\Delta y}\begin{bmatrix} T_1(\mathbf{x},t)\Delta x_b\Delta y_b+T_2(\mathbf{x},t)\Delta x_b\Delta y_f \\ +T_3(\mathbf{x},t)\Delta x_f\Delta y_f+T_4(\mathbf{x},t)\Delta x_f\Delta y_b \end{bmatrix} \tag{4.59}$$

In the direct heating approach, a Lagrangian heat source term $h(\mathbf{X},t)$ is determined at the location of the solid nodes such that the representative temperature at the solid node is $T_b(\mathbf{X},t)$. The Lagrangian heat source $h(\mathbf{X},t)$ is obtained from Eq. (4.60).

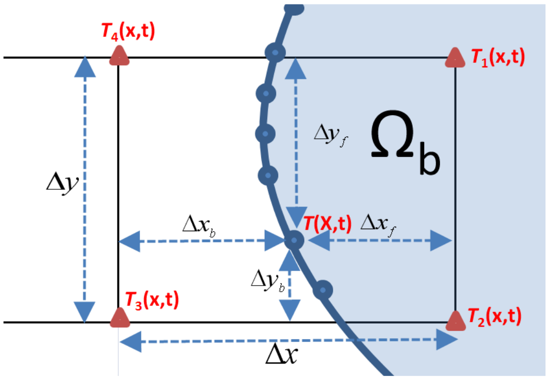

Figure 4.2 Schematic of bilinear interpolation for temperature at solid grid point.

$$h(\mathbf{X},t)=\left(\frac{T_b(\mathbf{X},t)-T(\mathbf{X},t)}{\partial t}+\mathbf{u}\bullet\nabla T(\mathbf{X},t)\right)-\alpha\nabla^2 T(\mathbf{X},t) \tag{4.60}$$

The Lagrangian heat source term $h(\mathbf{X},t)$ can be regarded as the penalty or artificial heat source to ensure that the constant temperature boundary condition ($T_b(\mathbf{X},t)$) is satisfied or enforced on the solid boundary. The Lagrangian heat source $h(\mathbf{X},t)$ is then transformed and distributed to the Eulerian fluid nodes using the discrete Dirac delta function $\delta(\mathbf{x}-\mathbf{X})$ as shown in Eq. (4.61) to obtain the heat source $H(\mathbf{x},t)$ at the fluid nodes .

$$H(\mathbf{x},t) = \int h(\mathbf{X},t)\delta(\mathbf{x}-\mathbf{X})\mathbf{ds} \tag{4.61}$$

Using Eq. (4.39), the heat source H_i along the i$^{\text{th}}$ lattice direction can be determined from $H(\mathbf{x},t)$. The determined H_i is then used in the PSA thermal model in Eq. (4.37) to update the thermal PDF h_i and the temperature of the fluid can be obtained from Eq. (4.52). A new method of determining the local Nusselt number within the context of thermal IBM will be derived. The local Nusselt number $Nu_l(\mathbf{X},t)$ is shown in Eq. (4.62) where L, $\gamma(\mathbf{X},t)$ and κ are the characteristic length scale, heat transfer coefficient and thermal conductivity of the fluid.

$$Nu_l(\mathbf{X},t) = \frac{\gamma(\mathbf{X},t)L}{\kappa} \tag{4.62}$$

The surface heat flux $q''(\mathbf{X},t)$ at the boundary node of the immersed body is given by Eq. (4.63), where T_∞ is the fluid reference temperature.

$$q''(\mathbf{X},t) = \gamma(\mathbf{X},t)\left(T_b(\mathbf{X},t) - T_\infty\right) \tag{4.63}$$

Eq. (4.64) relates the surface heat flux $q''(\mathbf{X},t)$ and the direct heating source $h(\mathbf{X},t)$ at each solid node.

$$q''(\mathbf{X},t) = \rho c_p h(\mathbf{X},t) dx \tag{4.64}$$

Using Eq. (4.63) and (4.64), the heat transfer coefficient γ(X,t) can be rewritten in terms of the direct heating source term $h(\mathbf{X},t)$ as shown in Eq. (4.65).

$$\gamma(\mathbf{X},t) = \frac{\rho c_p h(\mathbf{X},t) dx}{\left(T_b(\mathbf{X},t) - T_\infty\right)} \tag{4.65}$$

Substituting $\gamma(\mathbf{X},t)$ in Eq. (4.65) into Eq. (4.62) and the local Nusselt number can be expressed in the form as shown in Eq. (4.66)

$$Nu_l(\mathbf{X},t) = \frac{h(\mathbf{X},t) dxL}{\left(T_b(\mathbf{X},t) - T_\infty\right)\alpha} \tag{4.66}$$

The form of the local Nusselt number in Eq. (4.66) offers a unique advantage in the calculation of the Nusselt number that no extra computational step is needed in determining the surface normal and the temperature gradient normal to the surface, as required in previous thermal IBM studies (Jeong et al. 2010; Yoon et al. 2010 and Kim et al. 2004). The local Nusselt number can readily be determined from the heat source $h(\mathbf{X},t)$. This advantage is particularly useful for moving boundary applications where the surface normal changes as the boundary moves. The surface-averaged Nusselt number Nu over the boundary surface is of practical interest in many engineering applications as it provides a measure of the overall heat transfer. Nu can be determined by averaging the local Nusselt number over the solid grid points as shown in Eq. (4.67) where $\mathbf{\Omega}_L$ is the total arc length of the immersed boundary (for 2D-cases)

$$Nu = \frac{1}{\mathbf{\Omega}_L}\int Nu_l(\mathbf{X},t)ds \tag{4.67}$$

4.2.2 Direct Heating IB-LBM for Constant Heat Flux Boundary Condition

The sketch of an immersed body with a constant heat flux $q''(\mathbf{X},t)$ on its boundary is shown in Figure 4.3. Similar to Figure 4.1, the solid nodes are shown with blue circle markers while the fluid nodes are shown with red triangle markers and the temperature of the four neighboring node of a solid node are denoted by $T_1(\mathbf{x},t)$, $T_2(\mathbf{x},t)$, $T_3(\mathbf{x},t)$ and $T_4(\mathbf{x},t)$. For heat flux boundary condition, the desired temperature $T_b(\mathbf{X},t)$ and Lagrangian heating source $h(\mathbf{X},t)$ in Eq. (4.60) needs to be determined.

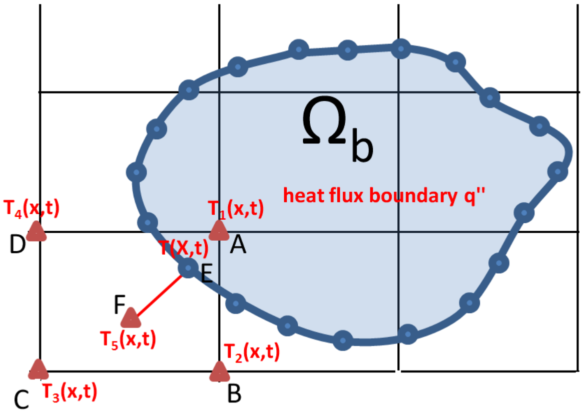

Figure 4.3 Schematic of the immersed body for constant heat flux boundary condition.

Referring to Fig. 4.3, previous studies using the finite volume method IBM (Kim et al. 2004) have approached such a boundary condition by selecting a point F, which lies inside of the boundary volume cell, and on the surface normal at the boundary point E. The desired temperature $T_b(\mathbf{X},t)$ is then determined by enforcing the heat flux $q''(\mathbf{X},t)$ between boundary node and the interior node point F.

In the current work, a new method is proposed for the Neumann type boundary condition for thermal IBM. The method eliminates the need to determine the surface normals and the need to interpolate for temperature at an interior point in the calculation of the surface temperature. The present method will be beneficial particularly for problems that contain deforming boundary, since the surface normal will change as the boundary deforms. The new method is described in the following.

1. The direct heating source $h(\mathbf{X},t)$ can be determined from Eq. (4.64), since ρ, c_p, dx and heat flux $q''(\mathbf{X},t)$ are known.

2. The determined Lagrangian heat source $h(\mathbf{X},t)$ is used in calculating the Eulerian heat source $H(\mathbf{x},t)$ and is distributed to the fluid nodes using Eq. (4.61).
3. Bilinear interpolation is used to obtain the temperature T(X,t) at point E only. With $h(\mathbf{X},t)$ and $T(\mathbf{X},t)$ determined, Eq. (4.60) can be reformulated in terms of the unknown $T_b(\mathbf{X},t)$ as shown in Eq. (4.68).
4.

$$T_b(\mathbf{X},t)=T(\mathbf{X},t)+\Delta t\left(h(\mathbf{X},t)-\mathbf{u}\bullet\nabla T(\mathbf{X},t)+\alpha\nabla^2 T(\mathbf{X},t)\right) \tag{4.68}$$

$T_b(\mathbf{X},t)$ in Eq.(4.68) can be viewed as the temperature required on the boundary in order to satisfy the heat flux boundary condition. $T_b(\mathbf{X},t)$ and $h(\mathbf{X},t)$ determined in steps 1 and 3 can then be used to determine the local Nusselt number using Eq. (4.66)

CHAPTER 5

MULTIPHYSICS COUPLING SCHEME

5.1 Multiphysics Coupling Approaches

Multiphysics phenomena involve the multidisciplinary interaction between complex systems that are governed by different physical laws or governing equations with the systems having sometimes disparate time scales. Examples are conjugate heat or mass transfer across a deformable arterial wall. The blood flow deforms the arterial wall and the resulting wall deformation affects the flow pattern. The perturbed, or disturbed, flow pattern in turn affects the heat/mass transfer characteristics. Other examples are in combustion or chemically reacting processes where the fluid flow pattern affects the temperature or specie concentration with the temperature or specie concentration having an effect on the reaction kinetics. There are two approaches typically used in simulating multiphysics problems namely the monolithic and partitioned approaches (Hubner et al. 2004).

In the monolithic approach, the governing equations of the interacting complex systems are integrated and solved simultaneously using the same discretization scheme and numerical solver. The couplings between the interacting systems are implicitly, or inherently, achieved as the coupled equations are solved. An example in the case of FSI problem will be to solve the Navier-Stokes and solid deformation equations in the same solver using the same discretization scheme, such as finite volume or finite elements approach method. A monolithic approach has the advantage of capturing the underlying physics when there is a strong coupling between the field variables of the interacting system (Hubner et al. 2004). On the other hand, ill conditioned coefficient matrices can arise with monolithic approaches when the systems have disparate time scales and stiffness. This necessitates the usage of a global pre-conditioner (Heil 2004). It is also computationally expensive when using monolithic approaches for realistic or large scale coupled problems in for example FSI applications. The possibility of leveraging domain specific numerical scheme or available software is obliterated with monolithic approaches.

A partitioned approach uses separate solvers for the interacting complex system. For example, in a FSI application, different solvers are used for the fluid and solid equations. The coupling between the fluid and solid solver has to be explicitly enforced by the interchange of information or field variables in order to satisfy both dynamic and kinematic constraints at the fluid/structure (FS) interface. Partitioned approach can have implicit or explicit coupling scheme. In implicit coupling scheme, the solution variables is iterated over the solution field in both the fluid and solid solver until a convergence criterion is achieved and hence information interchange is done several times within a time step. In an explicit coupling scheme, the solution variable is solved only once by the fluid and solid solver. Information interchange occurs only once per time step and requires smaller time steps than the implicit coupling scheme. The partitioned approach has the advantage of leveraging existing domain specific codes that is well developed and tested. The partitioned approach is faced with the challenge of accurately implementing the information exchange at the interface of the interacting systems, since each solver can have non matching mesh with different resolution at the interface.

A partitioned approach numerical framework was developed in the current work using the direct forcing and heating IB-LBM with a finite element based commercial software ABAQUS 6.8 for arterial wall thermography. The developed numerical framework is not limited to arterial wall thermography applications but can be applied to problems with conjugate heat/mass transfer between a fluid and a deforming, or non-deforming solid wall. The direct forcing IB-LBM was used for determining the fluid forces to be transferred to the solid solver while the newly developed direct heating IB-LBM was used for determining the heat transfer coefficient to be used at the fluid-solid interface. The finite element method was used for deformation and energy transport in the solid or arterial wall. In the subsequent sections, the structural dynamics and energy transport equations for the solid will be discussed. Arterial constitutive relations will also be discussed. The final section of the chapter will introduce the developed numerical framework for coupling between the fluid solver (using the direct forcing and heating IB-LBM) and the finite element solid solver.

5.2 Arterial Wall Dynamics

The governing equations for the mechanical response of the solid are the equilibrium or equations of motion, the constitutive equations relating the stress to the strain and the strain displacement equations.

5.2.1 Solid Body Stress and Strain Measures

The current position vector $\mathbf{x}_s$ of a solid Ω_s undergoing motion, or deformation, is related to its initial configuration with position vector $\mathbf{X}$ as shown in Eq. (5.1)

$$\mathbf{x}_s = \chi(\mathbf{X}, t) \tag{5.1}$$

The displacement vector $\mathbf{d}$ and the deformation gradient tensor F of the solid body are given by relations shown in Eq. (5.2) and (5.3).

$$\mathbf{d} = \mathbf{x}_s - \mathbf{X} \tag{5.2}$$

$$F = \frac{\partial \mathbf{x}_s}{\partial \mathbf{X}} \tag{5.3}$$

$$J = |F| \tag{5.4}$$

The determinant J of the deformation gradient tensor F is a measure of the change in volume of the solid body. The right Cauchy-Green deformation tensor C and the Green strain E are given by Eq. (5.5)-(5.6), where I is the identity tensor.

$$C = F^T F \tag{5.5}$$

$$E = \frac{1}{2}(C - I) = \frac{1}{2}\left(\nabla\mathbf{d} + \nabla\mathbf{d}^T + \nabla\mathbf{d}\nabla\mathbf{d}^T\right) \tag{5.6}$$

The principal stretches λ_i of the body in its respective coordinate directions i are determined as the eigenvalues of the tensor G where, G is as defined in Eq. (5.8).

$$\left|G^2 - \lambda I\right| = 0 \tag{5.7}$$

$$G^2 = C \tag{5.8}$$

The measures of stress in the body can be defined by the Cauchy σ or second Piola-Kirchhoff S stress tensors. The second Piola-Kirchhoff S stress is related to the Cauchy stress tensor by the relation shown in Eq. (5.9).

$$S = JF^{-1}\sigma F^{-T} \tag{5.9}$$

The invariants I_i of the deformation gradient tensor F are given by

$$I_i = \begin{cases} tr\left(C\right) = \lambda_1^2 + \lambda_2^2 + \lambda_3^2 \ , i = 1 \\ \dfrac{1}{2}\left[I_1^2 - tr\left(C^2\right)\right] = \lambda_1^2\lambda_2^2 + \lambda_1^2\lambda_3^2 + \lambda_2^2\lambda_3^2 \ , i = 2 \\ \left|C\right| = J^2 = \lambda_1^2\lambda_2^2\lambda_3^2 \ , i = 3 \end{cases} \tag{5.10}$$

where tr represents the trace of a tensor.

5.2.2 Arterial Wall Constitutive Equations

Due to the elastic nature of the arterial walls, constitutive equations are needed in order to determine the stress from the deformation or strain. The arterial wall is a hyperelastic material. For hyperelastic material modeling, the constitutive equations are typically expressed in terms of a scalar energy density function (SEDF) W. SEDF can be a function of the principal stretches λ_i or the Green strain E or the strain invariants I_i. The measures of stress (either S or σ) are determined from the derivative of the SEDF with respect to either Green deformation tensor C, or Green strain E, or the strain invariants I_i as shown in Eq. (5.11)-(5.13).

$$S=\frac{\partial W}{\partial E}=2\frac{\partial W}{\partial C} \tag{5.11}$$

$$\sigma=\frac{1}{J}F\frac{\partial W}{\partial E}F^{T}=\frac{2}{J}F\frac{\partial W}{\partial C}F^{T} \tag{5.12}$$

$$\sigma=\frac{2}{\sqrt{I_3}}\left[\left(\frac{\partial W}{\partial I_1}+I_1\frac{\partial W}{\partial I_2}\right)C-\frac{\partial W}{\partial I_2}C\bullet C\right]+2\sqrt{I_3}\frac{\partial W}{\partial I_3} \tag{5.13}$$

The arterial wall tissues are typically composed of 70% water and consequently the arterial wall is assumed to be incompressible (Kalita et al. 2008). The incompressible constraint means that not all displacements are admissible. The volume is conserved and therefore increase in dimension in one direction must lead to decrease in other directions in order to conserve volume. The incompressibility constraint of the arterial wall makes the third strain I_3 to be unity. The constitutive arterial wall models can be broadly classified into phenomenological and mechanistic (structural) arterial models. Phenomenological models are empirical in nature, while the mechanistic or structural, arterial model takes into consideration the structural information of the histology of the arterial wall (Gasser et al. 2006). The popular arterial phenomenological models that will be discussed are Fung type, logarithm type, Ogden and polynomial models. The structural or mechanistic based models of Holzapfel and Neo-Hookean will also be discussed in the following subsections.

Fung Type Arterial Model

The SEDF W of a Fung type arterial model in its general form under the assumption of isotropy is shown in Eq. (5.14)

$$W = \alpha\left(e^{Q} - 1\right) \tag{5.14}$$

where α are material parameters that are specific to the choice of the model. The variable Q appearing in the exponent in Eq. (5.14) is a function of a strain measure or invariant. The form of SEDF W in Eq. (5.14) is typically obtained by fitting it to experimental data. In its initial formulation by Fung (Chuong et al. 1983) the α and Q are shown in Eq. (5.15)

$$\begin{aligned} &\alpha = \frac{c_1}{2} \\ &Q = b_1 E_{\theta\theta}^2 + b_2 E_{zz}^2 + b_3 E_{rr}^2 + 2b_4 E_{\theta\theta} E_{zz} + 2b_5 E_{rr} E_{zz} \\ &\quad + 2b_6 E_{rr} E_{\theta\theta} + b_7 E_{\theta r}^2 + b_8 E_{rz}^2 + b_9 E_{\theta z}^2 \end{aligned} \tag{5.15}$$

where $c_1, b_i\left(i \in [1\ 9]\right)$ parameters are determined from the fit to experimental data and $E_{ij}\left(i, j \in [r, \theta, z]\right)$ are components of the Greens strain in the cylindrical coordinate system. There are also the 2D variants of the Fung type model (Fung et al. 1993) where there is the assumption of no torsion and inflation strains ($E_{\theta r} = E_{\theta z} = 0$). Other variants of the model is that proposed by Delfino (Delfino et al. 1997) where Q is a function of the strain invariant I_1 as shown in Eq. (5.16), where a and b are material properties.

$$\alpha = \frac{a}{b} \tag{5.16}$$

$$Q = \frac{b}{2}\left(I_1 - 3\right) \tag{5.17}$$

Logarithm Type Arterial Model

The SEDF W for the logarithm arterial model is a function of the natural logarithm of a strain measure and has the general form shown in Eq. (5.18)

$$W = \alpha \ln\left(Q\right) \tag{5.18}$$

where α are material parameters and Q is a function of a strain measure or invariant. The logarithm type model was used to model the pressure-radius relationship for a canine carotid artery with Q (Takamizawa et al. 1987) as defined in Eq. (5.19).

$$\begin{aligned} &\alpha = -c_1 \\ &Q = 1 - \frac{a_{\theta\theta} E_{\theta\theta}^2}{2} - \frac{a_{zz} E_{zz}^2}{2} - a_{\theta z} E_{\theta\theta} E_{zz} \end{aligned} \tag{5.19}$$

Other variants of the logarithm type arterial model available in literature (Horgan et al. 2003) is of the form shown in Eq. (5.20)

$$\begin{aligned} &\alpha = -\frac{\mu}{2} J_m \\ &Q = 1 - \frac{I_1 - 3}{J_m} \end{aligned} \tag{5.20}$$

J_m is the maximum limiting value of $I_1 - 3$.

Ogden Type Arterial Model

The Ogden material model is typically used for modeling rubber-like material (Fu et al. 2001). It is used in arterial wall modeling due to the similarity of strain stiffening effects common to both arterial wall and rubber. The SEDF W in the Ogden arterial wall model is a function of the principal stretches λ_i and has the form shown in Eq. (5.21)

$$W = \sum_{i=1}^{2} \frac{\mu_i}{\alpha_i} \left(\lambda_1^{\alpha_i} + \lambda_2^{\alpha_i} + \lambda_3^{\alpha_i} - 3 \right) \tag{5.21}$$

where μ_i and α_i are material parameters. The Ogden material model was used to model arterial damage in a bovine carotid artery (Hokanson et al. 1997).

Polynomial Type Arterial Model

The polynomial order model expresses the SEDF W as a polynomial of the modified strain invariant and has the form shown in Eq. (5.22) with the assumption of incompressibility of the arterial wall (Zunino et al. 2009 and Gervaso et al. 2008). A_{ij} is a material constant determined from the fit to experimental data.

$$W = \sum_{i+j=1}^{N} A_{ij} \left(\overline{I}_1 - 3 \right)^i \left(\overline{I}_2 - 3 \right)^j \tag{5.22}$$

$$\bar{I}_1 = J^{-2/3} I_1$$
$$\bar{I}_2 = J^{-4/3} I_2 \tag{5.23}$$

Neo-Hookean Arterial Wall Model

The Neo-Hookean (Taber 2004) is a simple hyperelastic model and has the form shown in Eq. (5.24)

$$W = \frac{\mu}{2}\left(I_1 - 3\right) \tag{5.24}$$

where μ is the shear bulk modulus of the arterial wall.

Holzapfel Type Anisotropic Arterial Model

Most arterial models and the ones discussed previously assumes that the arterial wall is isotropic but in reality the walls are typically anisotropic. In order to introduce anisotropy into the arterial wall constitutive models, Holzapfel and his co-workers (Holzapfel et al. 2010 and Holzapfel et al. 2008) developed an anisotropic material model whose SEDF W is a summation of an isotropic SEDF W_{iso} and anisotropic SEDF W_{aniso}. The modeling of the anisotropic SEDF is achieved by assuming that the arterial wall is fiber reinforced with two family of collagen fibers with direction cosines m' and m. The isotropic part is a Neo-Hookean model (as defined in Eq. (5.25)) with contribution coming from the elastin in the arterial wall.

$$W_{iso} = \frac{\mu}{2}\left(I_1 - 3\right) \tag{5.25}$$

Additional strain invariants (I_4 and I_6) are introduced in order to determine the anisotropic SEDF W_{aniso}. The additional strain invariants are determined from Eq. (5.26)

$$\begin{aligned} I_4 &= m \bullet \left(Cm\right) \\ I_6 &= m' \bullet \left(Cm'\right) \end{aligned} \tag{5.26}$$

The anisotropic SEDF W_{aniso} is then obtained as

$$\begin{aligned} &W_{aniso} = \frac{k_1}{2k_2} \sum_{i=4,6} e^{Q} - 1 \\ &Q = k_2\left(\kappa I_1 + \left(1 - 3\kappa\right) I_i - 1\right)^2 \\ &\kappa \in \begin{bmatrix} 0 & \frac{1}{3} \end{bmatrix} \end{aligned} \tag{5.27}$$

where k_1 and k_2 are parameter constants. κ determines the dispersion of the collagen fibers. When $\kappa = 0$ means there is no dispersion of the fibers while $\kappa = 1/3$ corresponds to the case of isotropic dispersion.

5.2.3 Arterial Wall Equation of Motion

The governing equation of motion for the arterial wall is given by Eq. (5.28)

$$\sigma_{ij,j} = \rho_s \ddot{d}_i \tag{5.28}$$

where $\sigma_{ij,j}$ is the derivative of the components of the Cauchy stress tensor σ_{ij} with respect to the spatial coordinates x_j. ρ_s and $\ddot{d}_i$ are the density and acceleration of the solid or arterial wall. The finite element method was used in the current work to discretize and solve the equation of motion shown in Eq. (5.28). In finite elements, the continuum equations are discretized into an assembly of finite element sets that are connected to each other at nodes. Each element set have a finite degrees of freedom defined at its nodes. The finite element discretization of Eq. (5.28) was done using the principle of virtual displacements which states that under a small virtual displacement, the virtual internal work δU_{int} of the system is equal to the external virtual work δU_{ext} in order to maintain equilibrium of forces. The virtual internal work is given by Eq. (5.29)

$$\delta U_{\mathrm{int}} = \int_{V_s} \{\delta E\}^T \{\sigma\} dV_s \tag{5.29}$$

The displacement vector $\mathbf{d}$ is discretized into the element nodal displacement vector $\{\mathbf{D}\}$ by the use of the shape function N as shown in Eq. (5.30)

$$\{\mathbf{d}\} = [N]\{\mathbf{D}\} \tag{5.30}$$

The strain-displacement relation in terms of the nodal displacements can be expressed as

$$E = [B]\{\mathbf{D}\} \tag{5.31}$$

where the matrix $[B]$ contains derivatives of the shape function N. The matrix $[B]$ is obtained by using the strain-displacement relation in Eq. (5.6) and the finite element approximation of the displacements in Eq. (5.30). The stress-strain in the finite element form is shown in Eq. (5.32)

$$\sigma = [E_{mat}]\{E\} \tag{5.32}$$

where the matrix $[E_{mat}]$ is the elasticity matrix that and it is obtained from the constitutive equations of the arterial wall or solid of interest. Substituting Eq. (5.31) into Eq. (5.32) in order to obtain the stress in terms of the nodal displacements yields

$$\sigma = [E_{mat}][B]\{\mathbf{D}\} \tag{5.33}$$

Substituting Eq. (5.31) and Eq. (5.33) into the virtual internal work δU_{int} in Eq. (5.29) yields

$$\delta U_{\text{int}} = \sum \int_{V_{el}} \{[B]\{\delta\mathbf{D}\}\}^T [E_{mat}][B]\{\mathbf{D}\}\, dV_{el} = \{\delta\mathbf{D}\}^T \sum \int_{V_{el}} [K]_{el}\{\mathbf{D}\}\, dV_{el} \tag{5.34}$$

$$[K]_{el} = [B]^T [E_{mat}][B] \tag{5.35}$$

where $[K]_{el}$ and dV_{el} is the element stiffness matrix and volume. In cases where there is internal damping by the solid material, a damping element matrix $[C]_{el}$ can be introduced. The virtual internal work can be expressed as

$$\delta U_{\text{int}} = \{\delta \mathbf{D}\}^T \sum \int_{V_{el}} [K]_{el} \{\mathbf{D}\} dV_{el} + \{\delta \mathbf{D}\}^T \sum \int_{V_{el}} [C]_{el} \{\dot{\mathbf{D}}\} dV_{el} \tag{5.36}$$

where $\{\dot{\mathbf{D}}\}$ is the velocity vector. The external virtual work δU_{ext} is composed of contribution from body forces $\{\mathbf{F}_b\}$ such as the inertia and external concentrated forces $\{\mathbf{F}_c\}$.

$$\delta U_{ext} = \int_{V_s} \{\delta \mathbf{D}\}^T \{\mathbf{F}_b\} dV_s + \{\delta \mathbf{D}\}^T \{\mathbf{F}_c\} \tag{5.37}$$

$$\{\mathbf{F}_b\} = -[N]\rho_s [N]^T \{\ddot{\mathbf{D}}\} \tag{5.38}$$

The body force can be discretized using the shape functions into the form

$$\{\mathbf{F}_b\} = -\sum [M]_{el} \{\ddot{\mathbf{D}}\} \tag{5.39}$$

$$[M]_{el} = [N]^T \rho_s [N] \tag{5.40}$$

where $[M]_{el}$ is the element mass matrix. Substituting Eq. (5.39) into Eq. (5.37) yields

$$\delta U_{ext} = \sum - \int_{V_{el}} [M]_{el} \{\ddot{\mathbf{D}}\} dV_{el} + \{\delta \mathbf{D}\}^T \{\mathbf{F}_c\} \tag{5.41}$$

Equating the δU_{ext} and δU_{int} yields the finite element equation of motion

$$[M]\{\ddot{\mathbf{D}}\}+[C]\{\dot{\mathbf{D}}\}+[K]\{\mathbf{D}\}=\{\mathbf{F}_c\} \tag{5.42}$$

$$\begin{gathered}[M]=\sum[M]_{el}\\ [C]=\sum[C]_{el}\\ [K]=\sum[K]_{el}\end{gathered} \tag{5.43}$$

where $[M]$, $[C]$ and $[K]$ are the global mass, damping and stiffness matrices obtained. The Newmark integration scheme is used for numerical integration of Eq. (5.42). The Newmark method expresses the velocity and displacement at the current time step (time step n+1) in terms of known variables from the previous time step (time step n) and unknown acceleration $\{\ddot{\mathbf{D}}\}_{n+1}$ of the current time step as shown in Eq. (5.45)-(5.46). The acceleration at the current time step is determined from Eq. (5.44).

$$\{\ddot{\mathbf{D}}\}_{n+1}=[M]^{-1}\left\{\{\mathbf{F}_c\}_{n+1}-[C]_{n+1}\{\dot{\mathbf{D}}\}_{n+1}-[K]_{n+1}\{\mathbf{D}\}_{n+1}\right\} \tag{5.44}$$

$$\{\dot{\mathbf{D}}\}_{n+1}=\{\dot{\mathbf{D}}\}_n+\Delta t\left[(1-\gamma)\{\ddot{\mathbf{D}}\}_n+\gamma\{\ddot{\mathbf{D}}\}_{n+1}\right] \tag{5.45}$$

$$\{\mathbf{D}\}_{n+1}=\{\mathbf{D}\}_n+\Delta t\{\dot{\mathbf{D}}\}_n+\frac{\Delta t^2}{2}\left[(1-2\beta)\{\ddot{\mathbf{D}}\}_n+2\beta\{\ddot{\mathbf{D}}\}_{n+1}\right] \tag{5.46}$$

Where Δt is the time step, γ and β are constants that affects the integration scheme and numerical stability. For the choice of $\gamma = {}^1\!/_2$, $\beta = {}^1\!/_4$ results in an implicit scheme that is unconditionally stable while the choice of $\gamma = {}^1\!/_2$, $\beta = {}^1\!/_6$ leads to an explicit scheme that is conditionally stable, values of $\gamma > \frac{1}{2}$ results in numerical damping. Hilber et al. 1978 introduced the α parameter that is used to achieve controllable numerical damping and also maintain an implicit numerical scheme. The numerical damping removes high frequency noise or oscillations in the numerical solution. The α parameter is related to γ and β as shown in Eq. (5.47). The case of $\alpha = 0$ corresponds to no numerical damping while $\alpha = -\frac{1}{3}$ corresponds to high numerical damping.

$$\gamma = \frac{1-2\alpha}{2}, \; \beta = \frac{(1-\alpha)^2}{4}, \; \alpha \in \left[-\frac{1}{3}, 0\right] \tag{5.47}$$

5.3 Arterial Wall Heat Transfer

The governing energy equation at the arterial wall is shown in Eq. (5.48) with the assumption that effect of heat transfer due to blood perfusion is negligible.

$$\frac{\partial\left(\rho_s C_p T\right)}{\partial t} + \nabla \bullet \left(\kappa \nabla T\right) = q''' \tag{5.48}$$

Where C_p, κ and T are the specific heat, thermal conductivity and temperature of the arterial wall. q''' is the volumetric heat generation rate within the arterial wall due to tissue metabolism. An integral formulation of the energy equation in Eq. (5.48) with the introduction of surface heat flux terms q'' can be written as

$$\int_{V_s} \frac{\partial\left(\rho_s C_p T\right)}{\partial t} dV_s + \int_{V_s} \nabla \bullet \left(\kappa \nabla T\right) dV_s = \int_{V_s} q''' dV_s + \int_S q'' dS \tag{5.49}$$

Using the standard Galerkin finite element formulation for the energy equation in Eq. (5.49) yields

$$\begin{gathered} \sum \int_{V_{sl}} \delta T \frac{\partial\left(\rho_s C_p [N]\{\mathbf{T}\}\right)}{\partial t} dV_{el} + \sum \int_{V_{el}} \delta T \; \nabla \bullet \left(\kappa \nabla [N]\{\mathbf{T}\}\right) dV_{el} = A \\ A = \sum \int_{V_{el}} \delta T \; q''' dV_{el} + \sum \int_{S_{el}} \delta T \; q'' dS_{el} \end{gathered} \tag{5.50}$$

$$T = [N]\{\mathbf{T}\} \tag{5.51}$$

$$\delta T = [N]\{\delta \mathbf{T}\} \tag{5.52}$$

where δT is the weight used in the Galerkin finite element formulation, $\{\mathbf{T}\}$ is the nodal temperature of an element , dS_{el} is an element surface area and $\{\dot{\mathbf{T}}\}$ is time derivative of the nodal temperature. Substituting Eq. (5.52) yields

$$\sum \int_{V_{sl}} \{\delta \mathbf{T}\} \left[C_{cap}\right]_{el} \{\dot{\mathbf{T}}\} dV_{el} + \sum \int_{V_{el}} \delta \mathbf{T} \; [\mathrm{K}_{cond}]_{el} \{\mathbf{T}\} \; dV_{el} = \delta \mathbf{T} \sum \{Q_{el}\} \tag{5.53}$$

$$\left[C_{cap}\right]_{el} = [N]^T \rho_s C_p [N] \tag{5.54}$$

$$[K_{cond}]_{el} = \nabla [N]^T \bullet \kappa \nabla [N] \tag{5.55}$$

$$\{Q_{el}\} = \int_{V_{el}} [N]^{\mathrm{T}} \; q''' dV_{el} + \int_{S_{el}} [N]^{\mathrm{T}} \; q'' dS_{el} \tag{5.56}$$

where $\left[C_{cap}\right]_{el}$ and $[K_{cond}]_{el}$ are the element capacitance and conductance matrices. Assembling of the respective element matrices reduces Eq. (5.50) to the global finite element discretization of the energy equation as shown in Eq. (5.57).

$$\left[C_{cap}\right]\left\{\dot{\mathbf{T}}\right\}+\left[K_{cond}\right]\left\{\mathbf{T}\right\}=\left\{\mathbf{Q}\right\} \tag{5.57}$$

$$\begin{aligned}\left[C_{cap}\right]&=\sum\left[C_{cap}\right]_{el}\\ \left[K_{cond}\right]&=\sum\left[K_{cond}\right]_{el}\end{aligned} \tag{5.58}$$

The time integration of Eq. (5.57) can be written in the general time discrete form shown in Eq. (5.59)

$$\begin{gathered}\left[C_{cap}\right]\left(\frac{\left\{\mathbf{T}\right\}_{n+1}-\left\{\mathbf{T}\right\}_{n}}{\Delta t}\right)+\theta\left[K_{cond}\right]\left\{\mathbf{T}\right\}_{n+1}=\left\{\mathbf{Q}\right\}-\left(1-\theta\right)\left[K_{cond}\right]\left\{\mathbf{T}\right\}_{n}\\ 0\le\theta\le 1\end{gathered} \tag{5.59}$$

where $\left\{\mathbf{T}\right\}_{n+1}$ and $\left\{\mathbf{T}\right\}_{n}$ is the nodal temperature at the current and previous time step. The choice of parameter θ affects the numerical integration scheme. When $\theta=0$ produces the Euler forward difference scheme which is first order accurate in time, explicit and conditionally stable. When $\theta>0$ the resulting numerical scheme is implicit and unconditional stable, for $\theta=1$ and $\theta={}^{1}\!/_{2}$ results in the backward differencing and Crank-Nicolson schemes.

5.4 Implementation of the FSI and Conjugate Heat Transfer Coupling

The finite element discretization for the solid deformation and heat transfer was done using the ABAQUS 6.8 commercial package. The coupling between the LBM and ABAQUS was an explicit partitioned coupling scheme. For the FSI case, the forces at the fluid-solid interface Γ_I are required to be in balance. The force balance at the interface Γ_I is achieved by requiring continuity of normal component of stress at the interface using Eq. (5.60) where σ_f, σ_s are the fluid and solid stresses while $\mathbf{n}$ is the normal unit vector at Γ_I.

$$\sigma_f \mathbf{n} = \sigma_s \mathbf{n} \quad on\ \Gamma_I \tag{5.60}$$

The no-slip boundary condition must also be satisfied by requiring that the fluid velocity $\mathbf{u}_f$ from the LBM equals to the solid velocity $\mathbf{u}_s$ from ABAQUS as shown in Eq. (5.61).

$$\mathbf{u}_f = \mathbf{u}_s \quad on\ \Gamma_I \tag{5.61}$$

In terms of the explicit coupling scheme implementation, LBM calculates the fluid loading pressure $\sigma_f \mathbf{n}$ and impose it as a traction boundary condition in ABAQUS at the fluid-solid interface Γ_I. The traction boundary condition $\sigma_f \mathbf{n} A$ acts as a forcing function or loading vector $\{\mathbf{F}_c\}$ on the right hand side of the solid equation of motion (Eq. (5.41)) where A is the deformed or current surface area. Figure 5.1 shows an arbitrary finite element discretization of a solid consisting of 5 elements (four quadrilateral and one triangle elements with 8 and 6 nodes respectively). The elements are numbered 1 to 5 for illustrative purposes. The common nodes between LBM and ABAQUS (that is at the fluid-solid interface) is shown with the red filled circles while the blue filled square are nodal points interior to the solid.

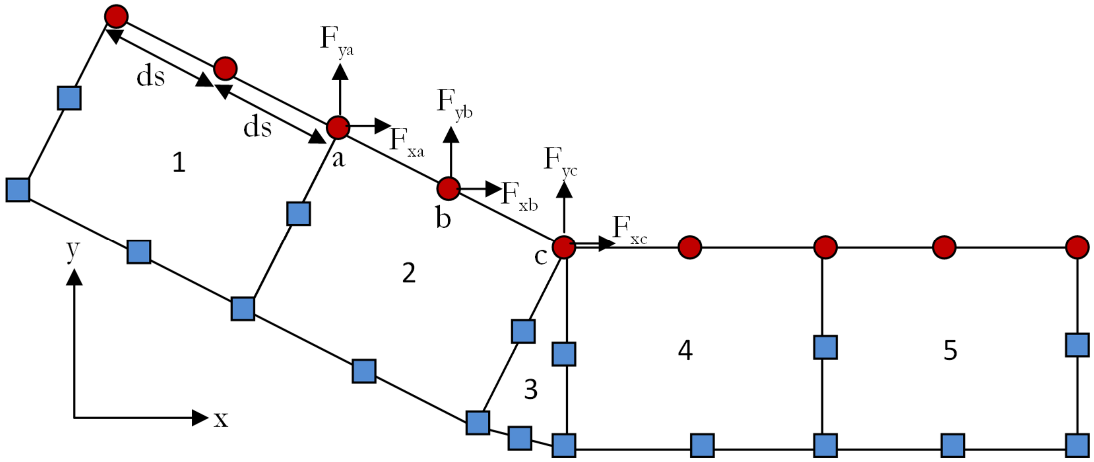

Figure 5.1 Schematic of the force coupling scheme between LBM and ABAQUS.

Looking at Element 2, the normal forces $\mathbf{F}_{n\alpha}$ (not shown in the Figure) at the interface nodes (where α represents the node labels a, b and c) are resolved into their respective components $F_{x\alpha}$ and $F_{y\alpha}$ in the x-y Cartesian coordinate system as shown in Figure 5.1 and Eq. (5.62).

$$\begin{gathered}\mathbf{F}_{n\alpha} = F_{x\alpha}\mathbf{i} + F_{y\alpha}\mathbf{j} \\ \alpha\text{=a,b,c}\end{gathered} \tag{5.62}$$

The terms $\mathbf{i}$ and $\mathbf{j}$ in Eq. (5.62) are the unit vectors in the x and y directions respectively. The direct forcing IB-LBM was used for calculation of $F_{x\alpha}$ and $F_{y\alpha}$ as shown in Eq. (5.63) and Eq. (5.65).

$$F_{x\alpha} = -C_{d\alpha}\left(0.5\rho_f u_o^2 dsD\right)_{PU} \tag{5.63}$$

$$C_{d\alpha} = \left(\frac{2ds\ \mathrm{dx}}{\rho_f u_0^2 D} \right)_{LU} f_x(\mathbf{X}_\alpha, t) \tag{5.64}$$

$$F_{y\alpha} = -C_{L\alpha} \left(0.5 \rho_f u_o^2 ds D \right)_{PU} \tag{5.65}$$

$$C_{L\alpha} = \left(\frac{2ds\ \mathrm{dx}}{\rho_f u_0^2 D} \right)_{LU} f_y(\mathbf{X}_\alpha, t) \tag{5.66}$$

$$\mathbf{f}(\mathbf{X}_\alpha, t) = f_x(\mathbf{X}_\alpha, t)\ \mathbf{i} + f_y(\mathbf{X}_\alpha, t)\ \mathbf{j} \tag{5.67}$$

Where ρ_f, u_o, ds and D are the fluid density, characteristic velocity, node grid spacing and characteristic length scale. $C_{d\alpha}$ and $C_{L\alpha}$ are the drag and lift coefficient at the nodes. dx is the fluid grid spacing while $f_x(\mathbf{X}_\alpha, t)$ and $f_y(\mathbf{X}_\alpha, t)$ are the components of the body force $\mathbf{f}(\mathbf{X}_\alpha, t)$ (that is obtained from the direct forcing Eq. (3.8)) in the x and y directions. The subscripts LU and PU in Eq. (5.63)-(5.66) represent LBM and physical units respectively. Terms with LU subscript are evaluated in LBM units while terms with PU are evaluated in physical units that are used in ABAQUS. The force $F_{x\alpha}$ and $F_{y\alpha}$ is then converted into element surface tractions T_x and T_y. For Element 2 in Figure 5.1, the surface tractions can be calculated as

$$T_x = \frac{\left(\dfrac{(F_{xa} 0.5ds) + (F_{xb} ds) + (F_{xc} 0.5ds)}{2ds} \right)}{2ds} = (F_{xa} 0.5ds) + (F_{xb} ds) + (F_{xc} 0.5ds) \tag{5.68}$$

$$T_y = \frac{\left(\dfrac{(F_{ya} 0.5ds) + (F_{yb} ds) + (F_{yc} 0.5ds)}{2ds} \right)}{2ds} = (F_{ya} 0.5ds) + (F_{yb} ds) + (F_{yc} 0.5ds) \tag{5.69}$$

The stress continuity boundary condition (Eq. (5.60)) at the interface Γ_I is then satisfied as

$$\sigma_f \mathbf{n} = \sigma_s \mathbf{n} = T_x\ \mathbf{i} +\ T_y\ \mathbf{j} \quad on\ \ \Gamma_I \tag{5.70}$$

The no-slip boundary condition at the interface is then enforced by setting the velocity $\mathbf{U}_b(\mathbf{X},t)$ in the direct forcing IB-LBM equation (Eq. (3.8)) equal to the solid velocity in lattice units using Eq. (5.71).

$$\mathbf{U}_b(\mathbf{X}_\alpha,t) = \mathbf{Re}_\alpha \left(\frac{\nu}{D} \right)_{LU} \tag{5.71}$$

$$\mathbf{Re}_\alpha = \left(\frac{\mathbf{u}_{s\alpha} D}{\nu} \right)_{PU} \tag{5.72}$$

The data or information exchange sequence between fluid solver LBM and solid solver ABAQUS is shown in Figure 5.2. A status flag was created in both codes to signal when to receive and wait for information. The flags are written to an external file that is periodically accessed by both solvers. The status flag for ABAQUS was named *ab_stat* while the status flag in LBM was named *for_stat.* For example when *for_stat* =1 and *ab_stat* =0 indicates that LBM is solving and ABAQUS should wait for information exchange. After LBM finishes solving it changes *for_stat* =0 and *ab_stat* =1 indicating that LBM should wait for information exchange while ABAQUS is solving. The status flag is written to an external file accessible by both LBM and ABAQUS. The fluid solver starts first at time t_n while ABAQUS waits for information exchange, once the fluid solver finishes solving at time t_{n+1}(Step 1 in Figure 5.1), the surface traction in Eq. (5.70) is then written to an external output file *press.txt* to be read by ABAQUS.

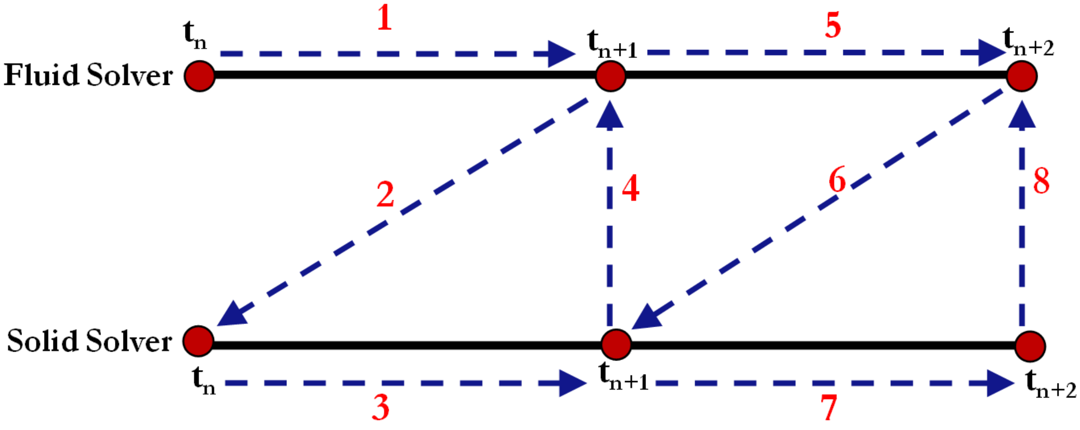

Figure 5.2 Data exchange sequence between LBM and ABAQUS.

The status flags *for_stat* is set to 0 and *ab_stat* to 1 by LBM. ABAQUS then reads the surface traction load (step 2) from the file *press.txt*. The traction load is used as boundary condition at the interface for the time interval t_n to t_{n+1} (step 3). At the end of step 3, ABAQUS writes the current nodal coordinates and velocities at the interface to an external file named *coord.txt* and *vel.txt*. The status flags *for_stat* is set to 1 and *ab_stat* to 0 by ABAQUS. LBM then reads the current nodal coordinates and velocities from *coord.txt* and *vel.txt,* the IB-LBM nodes are then updated with the newly received coordinates and velocities (step 4). The sequence of steps 1-2-3-4 completes one coupling cycle between LBM and ABAQUS, the cycles is repeated until the desired simulation stop time is reached. The information interchange at the ABAQUS side was handled by ABAQUS Fortran user subroutine *UEXTERNALDB*. The user subroutine *URDFIL* was used for writing of the velocities and coordinates to the external file *vel.txt* and *coord.txt while* user subroutine *UTRACLOAD* was used to impose the surface traction on the solid structure.

For the conjugate heat transfer case, the continuity of heat flux and temperature are required at the fluid-solid interface Γ_I as shown in Eq. (5.73) and Eq. (5.74).

$$\kappa_f \left(\frac{\partial T}{\partial n} \right)_{\Gamma_I} = \kappa_s \left(\frac{\partial T}{\partial n} \right)_{\Gamma_I} \tag{5.73}$$

$$T_{wf} = T_{ws} \tag{5.74}$$

Where κ_f and κ_s are the thermal conductivities of the fluid and solid. The wall temperature at the interface Γ_I from the fluid and solid sides are T_{wf} and T_{ws}. For the implementation of the interface boundary conditions in Eq. (5.73)-(5.74), ABAQUS sends the solid wall temperature to LBM. The solid wall temperature is then used in LBM as a boundary condition in order to satisfy temperature continuity at the interface. The direct heating IB-LBM is used for enforcing the wall temperature boundary condition. LBM in turn sends the Nusselt number to ABAQUS from which the heat transfer coefficient and heat flux can be calculated in order to satisfy the heat flux continuity at the interface. Using Element 2 shown in Figure 5.1 as an example, the element heat flux $\kappa_s \left(\frac{\partial T}{\partial n} \right)_{\Gamma_I}$ at the interface Γ_I for the solid solver can be determined using Eq. (5.75)

$$\kappa_s \left(\frac{\partial T}{\partial n} \right)_{\Gamma_I} = Nu \left[\frac{\kappa_f}{D} \left(T_{ws} - T_\infty \right) \right]_{PU} \tag{5.75}$$

$$Nu = \left(\frac{\left(Nu_a 0.5ds \right) + \left(Nu_b ds \right) + \left(Nu_c 0.5ds \right)}{2ds} \right)_{LU} \tag{5.76}$$

where T_∞ is the bulk fluid or reference temperature. Nu is the effective Nusselt number for the element 2 . The Nusselt number Nu is calculated from the local Nusselt numbers Nu_a, Nu_b and Nu_b at points a, b and c as shown in Eq. (5.76). The local Nusselt number is determined using the new approach proposed in Eq. (4.62). The heat flux determined at the interface from Eq. (5.75) is then used in the heat flux term q'' in Eq. (5.56). The temperature continuity boundary condition is enforced by setting $T_b(\mathbf{X},t)$ in the direct heating IB-LBM (Eq. 4.60) to the value shown in Eq. (5.77).

$$T_b(\mathbf{X},t) = \left(T_\infty \right)_{LU} \left(1 + \theta \right) \tag{5.77}$$

$$\theta = \left(\frac{T_{ws} - T_\infty}{T_\infty} \right)_{PU} \tag{5.78}$$

The updated temperature $T_b(\mathbf{X},t)$ is then used in the direct forcing IB-LBM as shown Eq. (4.60). The coupling between ABAQUS and IB-LBM for the conjugate heat transfer case is similar to the coupling scheme discussed previously for FSI case with the exception that the information exchanged is different (temperature and heat flux as opposed to traction, velocity and nodal coordinates). The ABAQUS user subroutine *DFILM* was used to impose the surface traction.

CHAPTER 6

RESULTS AND DISCUSSION

A 2D direct forcing and heating IB-LBM parallel code was developed using Fortran 90. The parallelism of the code was implemented using OpenMP. The developed IB-LBM code and multiphysics coupling scheme proposed in section 5.4 was validated in the current Chapter. The validated direct forcing and heating IB-LBM was then applied to study the influence of flow parameters, geometric parameters (macrophage cell density and fibrous cap thickness) on the thermal profile of a stenotic plaque in an artery. The first section of this chapter validates the LBM code using classical flows available in literature as benchmarks. The second section validates the direct forcing IB-LBM for rigid bodies while the third section validates direct forcing IB-LBM for flexible body problems (FSI). In addition, the third section also validates the proposed new multiphysics coupling scheme. The fourth section addresses the validation of the new direct heating IB-LBM and the last section applies the developed computational framework to a typical arterial thermography problem as highlighted previously.

6.1 Validation of the LBM code

The current section will be validating the LBM module of the code with classical flows such as Couette flow (with and without wall slip), Rayleigh flow (starting Couette flow) and lid driven cavity flow with slip. The choices of the benchmark cases are such that the LBM code was tested for its ability to capture boundary conditions adequately and transient flow phenomenon and rich flow features in 2D.

6.1.1 Validation of LBM Code with Couette Flow

The developed LBM code was benchmarked with the classical steady state Couette flow. The schematic of the flow domain is shown in Figure 6.1, the upper wall of the channel is moved with a horizontal linear velocity V_o while the lower wall is stationary. A linear velocity profile develops with an analytical solution (Panton, 2005) as given in Eq. (6.1).

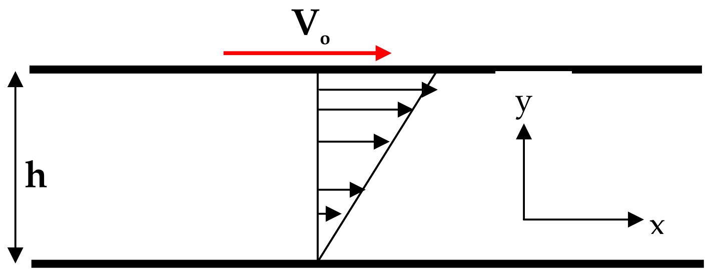

Figure 6.1 Schematic of the Couette flow.

$$u_x = \frac{V_o y}{h} \tag{6.1}$$

where u_x is the fluid velocity in x-coordinate or horizontal direction. Two test cases were conducted using the channel height h of 0.05m. The test cases were for a Reynolds number Re of 10 and 100 with Re as defined in Eq. (6.2).

$$\mathrm{Re} = \frac{V_o h}{\nu} \tag{6.2}$$

The D2Q9 lattice model was used. The bounce-back rule proposed by Zou et al. 1997 was used for the no slip boundary condition on the lower wall while the velocity boundary condition also proposed by Zou et al. 1997 was used for the moving wall. Periodic boundary conditions were used for the inflow and outflow boundaries. A 32 X 16 lattice grid with relaxation factor τ of 0.6 was used for Re =10 while a 128 X 64 lattice grid with relaxation factor τ of 0.58 was used for Re=100. The comparison of the results from the LBM code with that of the analytical solution is shown in Figure 6.2.

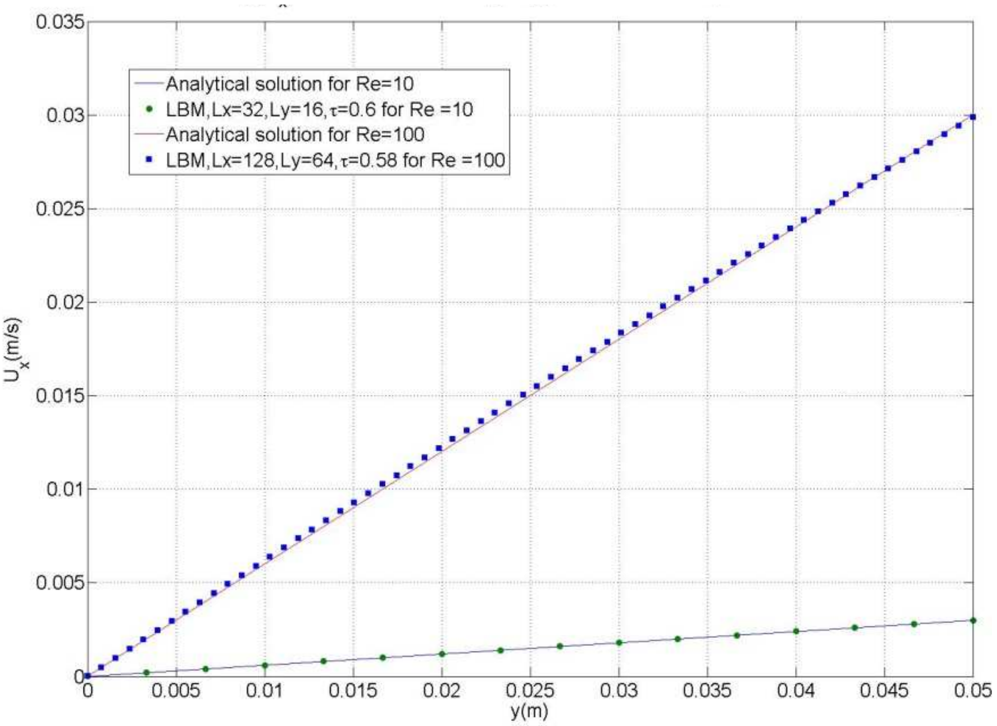

Figure 6.2 Comparison of the current LBM with analytical Couette flow results.

The results from the LBM code were able to capture the qualitative linear velocity profile as shown in Figure 6.2. There was also good agreement quantitatively between the current LBM results and analytical Couette flow results.

6.1.2 Validation of LBM Code with Rayleigh Flow

The Rayleigh or diffusion flow was used as a numerical benchmark to test the ability of the current LBM code to capture transient flow phenomena. In addition, the current benchmark will also assess the numerics that relate lattice units to physical units. The Rayleigh flow is induced by the impulsive motion of a flat plate. The velocity of the impulsively moved plate at time $t > 0$ is constant and denoted by V_o. In the current case, the lower wall or plate was moved with a velocity V_o=0.03m/s and the fluid has a kinematic viscosity υ of 0.15 Stokes. The flow has a Re of 100 with a channel height of 0.05m. The analytical solution (Panton, 2005) for the Rayleigh flow is given in Eq. (6.3)

$$\frac{U_x}{V_o} = 1 - erf\left(\frac{y}{2\sqrt{\upsilon t}}\right) \tag{6.3}$$

where erf is the error function. Eq. (2.81) and (2.82) was used to scale between LBM velocity and time lattice units with physical velocity and time scales. The D2Q9 lattice model was used for the discretization of the flow domain. Periodic boundary conditions were used for the inflow and outflow boundary conditions. The Zou moving wall boundary condition was used at y =0 and bounce-back rule was used at y = ∞ (that is at y=Ly in LBM). The transient velocity profile were sampled at times t = 1.3563, 6.7817 and 13.5634 seconds as shown on Figure 6.3. The LBM results agreed both qualitatively and quantitatively with the analytical solution for the developing velocity profile.

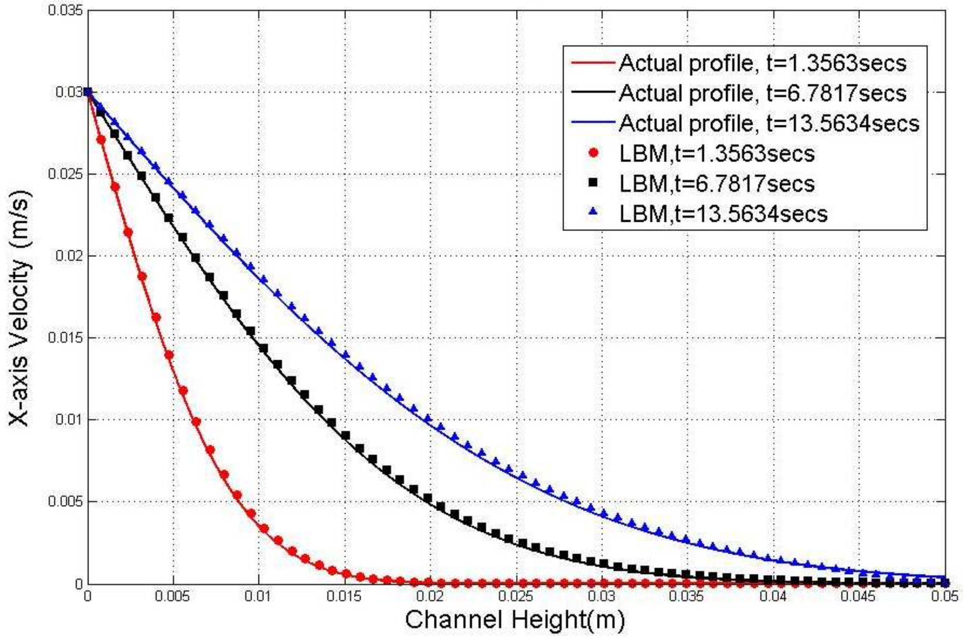

Figure 6.3 Comparison of the results between the current LBM code and analytical results for Rayleigh flow.

6.1.3 Validation of LBM Code Slip Boundary Condition with Micro-Couette Flow

The micro-Couette flow was also used as a numerical benchmark of the current code to test the implementation of the slip boundary condition. The micro Couette flow is similar to the Couette flow simulated in section 6.1.1, except that there is a slip flow at both the upper and lower walls and the traditional no-slip boundary condition is no longer applicable. The analytical solution for the isothermal 2D micro Couette flow (Liou et al. 2006) is

$$\frac{u}{V_o} = \frac{\dfrac{y}{h} + \left[\dfrac{2-\sigma}{\sigma}\right] Kn}{1 + 2\left[\dfrac{2-\sigma}{\sigma}\right] Kn} \tag{6.4}$$

where V_o is the upper wall velocity, h is the channel height, Kn is the Knudsen number and σ is the accommodation coefficient. σ is 1 for diffuse reflection and 0 for specular reflection. The slip boundary condition discussed in Chapter 2 and shown in Eq. (2.75) was used for implementation of the slip boundary condition in the current numerical benchmark. The Kn was related to the LBM parameters using Eq. (6.5)

$$Kn = \frac{c_s(\tau_f - 0.5)}{N_y} \tag{6.5}$$

where N_y is the channel height in lattice units and c_s is the lattice speed of sound. Numerical experiments were conducted for Kn of 0.01and 0.08 with Re =1. The accommodation coefficient σ had values of 0.1, 0.5, 0.8 and 1. The effect of Kn number on the normalized velocity $\frac{u}{V_o}$ profile is shown in Figure 6.4. Qualitatively, increasing the Kn number while keeping the accommodation coefficient σ constant leads to higher slip velocity at the walls. This qualitative feature was captured by the current LBM code as shown in Figure 6.4. There was also good agreement quantitatively between the LBM results and the analytical results. Similarly, Figure 6.5 shows the effect of σ on the normalized velocity profile. Qualitatively, there is increasing slip on the walls for reducing σ as captured by the current LBM results with good accuracy as shown in Figure 6.5.

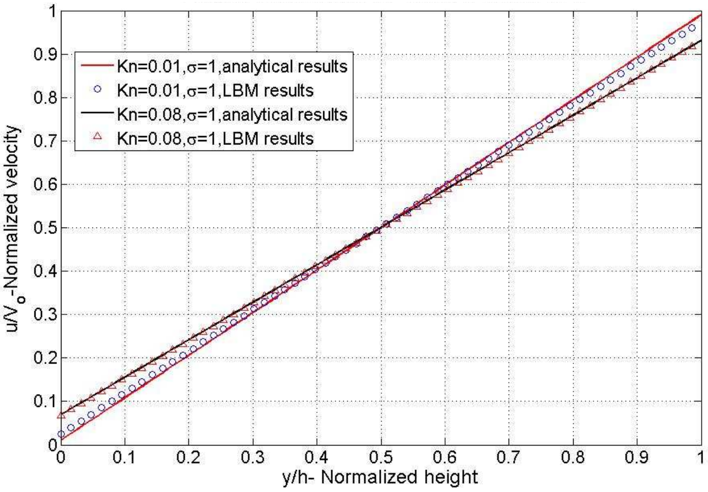

Figure 6.4 Effect of Kn number on the normalized velocity profile.

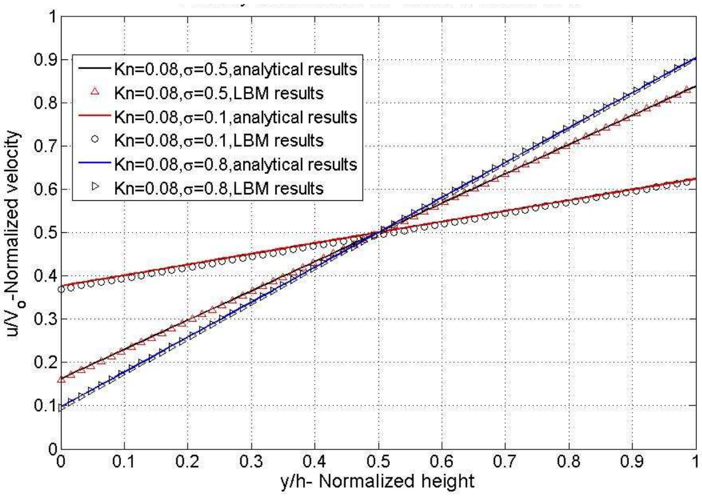

Figure 6.5 Effect of accommodation coefficient on the normalized velocity profile.

6.1.4 Validation of LBM Code with Lid Driven Cavity Flow

The current LBM code was used to simulate flow in a micro-lid-driven square cavity flow with Kn of 0.01, 0.1 and 0.2 with Re=0.3 and accommodation coefficients σ

of 0.2, 0.5 and 1. The upper wall of the square cavity moves with a constant velocity V_o from left to right while the other three walls are stationary. The movement of the upper wall leads to the formation of a circulatory flow. A 300 x 300 D2Q9 lattice model was used for the discretization of the flow domain. The center location of the vortex generated is recorded and benchmarked with that of published results (Tang et al. 2005) as shown on Table 6.1.

Table 6.1 Vortex center location for micro lid-driven cavity flow

Kn	•	Vortex center Location	
		Current Results	Tang et al. 2005
0.01	1	(0.5,0.762)	(0.5,0.7633)
0.01	0.5	(0.5,0.758)	(0.5,0.7567)
0.01	0.2	(0.5,0.74)	(0.5,0.7433)
0.1	1	(0.5,0.73)	(0.5,0.72)
0.1	0.5	(0.5,0.698)	(0.5,0.7067)
0.1	0.2	(0.5,0.687)	(0.5,0.69)
0.2	1	(0.5,0.668)	(0.5,0.66)

The vortex is centrally along the x-axis but its position along the y-axis depends on the Kn and σ. The y-location of the vortex center moves downward as the Kn number increases or as the accommodation coefficient decreases due to increasing slip effects at the wall. The ensuing flow pattern obtained from the LBM code is shown in a y-velocity contour plot in Figure 6.6 (for Kn=0.01, σ=1) where the velocity magnitudes are in lattice units.

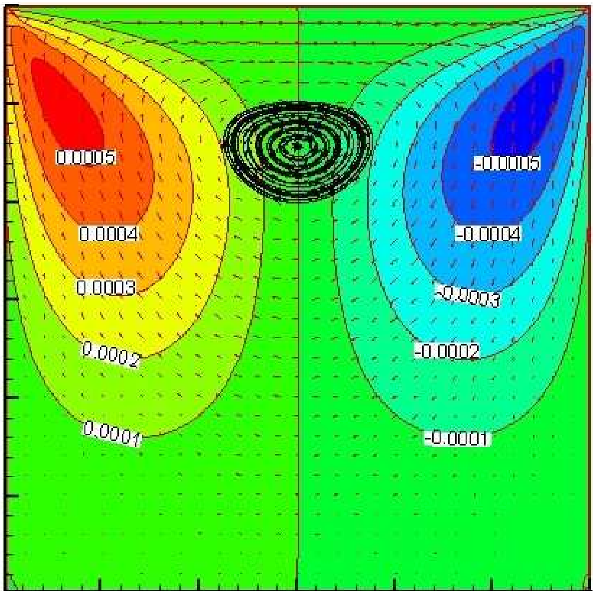

Figure 6.6 Velocity contour plot and vortex center location for Kn=0.01, σ =1.

The vortex center for Kn=0.01 and σ=1 is shown in Figure 6.6. The re-circulatory nature of the flow is such that there is an upward flow current in half of the domain (left hand side) and a downward flow current on the other half (right hand side) as shown in Figure 6.6. The current LBM code was able to capture these qualitative effects in vortex center locations and flow pattern features as shown on Table 6.1 and Figure 6.6. Quantitatively, there was also good agreement of the vortex center location with published results.

6.2 Validation of the Direct Forcing IB-LBM Code for Rigid Bodies

This section presents the validation of the direct forcing IB-LBM discussed in section 3.3. The numerical benchmarking in this section was for rigid, or non-deforming, immersed objects. The flow over a circular cylinder and NACA 0012 airfoil were used as numerical benchmark cases. The results will be presented and discussed in the next sections. The direct forcing IBM was used for handling of the boundary conditions of the immersed object.

6.2.1 Flow Over a Circular Cylinder

The schematic of the flow domain used for the current numerical benchmark is shown in Figure 6.7 (Turek et al. 1996). The 2D, circular cylinder is asymmetrically placed in a duct. A parabolic velocity profile is prescribed at the domain inlet for the x-axis velocity component U using Eq. 6.6 while the y-axis velocity component V is zero

$$\begin{aligned} U(0,y) &= \frac{4U_{mean}\,y\left(H-y\right)}{H^2} \\ V(0,y) &= 0 \end{aligned} \tag{6.6}$$

$$U_{mean} = \frac{2U(0,\frac{H}{2})}{3} \tag{6.7}$$

where U_{mean} is the average velocity at the inlet. Zero gradient of the velocity components was used as the boundary condition at the outlet. The bounce-back rule was used for the implementation of the no-slip boundary conditions on the top and bottom walls while the direct forcing IBM was used for the no-slip boundary conditions on the circular cylinder and also to account for the presence of the immersed cylinder in the underlying Cartesian fluid grid.

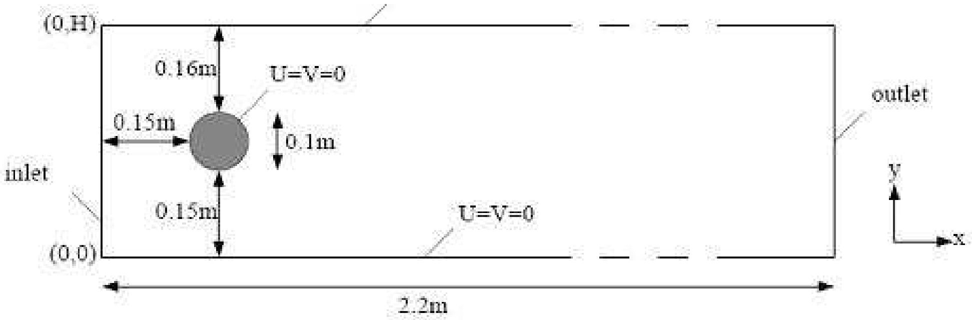

Figure 6.7 Schematic of the flow domain for the 2D circular cylinder numerical benchmark (Turek 1996).

Numerical experiments were conducted for Re =20 and Re =100. The multi-block LBM was used for grid refinement around the circular cylinder for both cases of Re=20 and Re=100. A 440 X 82 D2Q9 lattice model was used for discretization of the domain outside the refined region. The drag C_D and lift C_L coefficients were determined and benchmarked against the results of Turek et al. 1995. Other quantities of interest used for quantitative comparison with the results in literature were the recirculation length L behind the cylinder for case of Re =20, Strouhal number St for the case of Re=100 where vortex shedding occurs. C_D, C_L and St are as defined in Eq. (6.8)-(6.10)

$$C_D = \frac{2F_x}{\rho U_{mean}^2 D} \tag{6.8}$$

$$C_L = \frac{2F_y}{\rho U_{mean}^2 D} \tag{6.9}$$

$$St = \frac{fD}{U_{mean}} \tag{6.10}$$

where F_x and F_y are the drag and lift forces while f and D is the vortex shedding frequency and diameter of the cylinder. The C_D and C_L are determined from the direct forcing Lagrangian body force $\mathbf{f}(\mathbf{X},t)$ as

$$C_D = \left(\frac{2ds\ \mathrm{dx}}{\rho U_{mean}^2 D} \right) f_x(\mathbf{X},t) \tag{6.11}$$

$$C_L = \left(\frac{2ds\ \mathrm{dx}}{\rho U_{mean}^2 D} \right) f_y(\mathbf{X},t) \tag{6.12}$$

$$\mathbf{f}(\mathbf{X},t) = f_x(\mathbf{X},t)\ \mathbf{i} + f_y(\mathbf{X},t)\ \mathbf{j} \tag{6.13}$$

Tables 6.2 and 6.3 show the quantitative comparison between the current results and the benchmark results. There was good agreement between the current results from the IB-LBM code when compared to the published results. Figure 6.8 shows the x-axis velocity U contour and the recirculation zone behind the immersed cylinder for the case of Re = 20.

Table 6.2 Results for flow around a circular cylinder for Re =20

	Current Work	Turek et al. 1996
C_D	5.59	5.57 (lower bound) 5.59 (upper bound)
C_L	0.0108	0.0104 (lower bound) 0.011(upper bound)
L	0.0855	0.0842 (lower bound) 0.0852 (upper bound)

The lift coefficient C_L variation with the iteration number (lattice time units) for Re= 100 is shown in Figure 6.9, the periodicity of the C_L is due to the formation of the von Kármán vortex street as shown in the U-velocity contour plots in Figures 6.10 and 6.11.

Table 6.3 Results for flow around a circular cylinder for Re =100

	Current Work	Turek et al. 1996
C_D	3.25	3.22 (lower bound) 3.24 (upper bound)
C_L	1.02	0.99 (lower bound) 1.01 (upper bound)
St	0.3	0.295 (lower bound) 0.305 (upper bound)

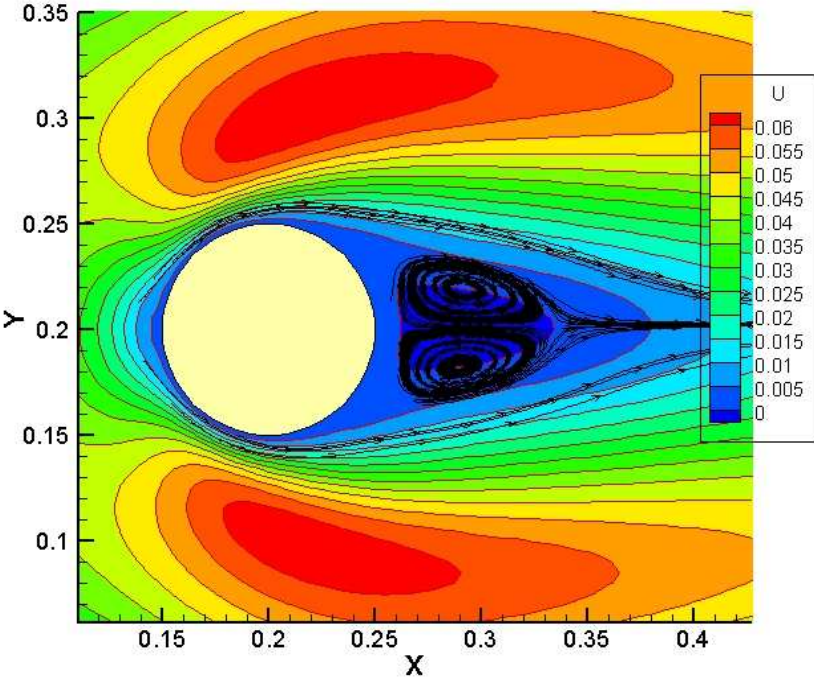

Figure 6.8 U velocity contour plot and recirculation zone for Re=20.

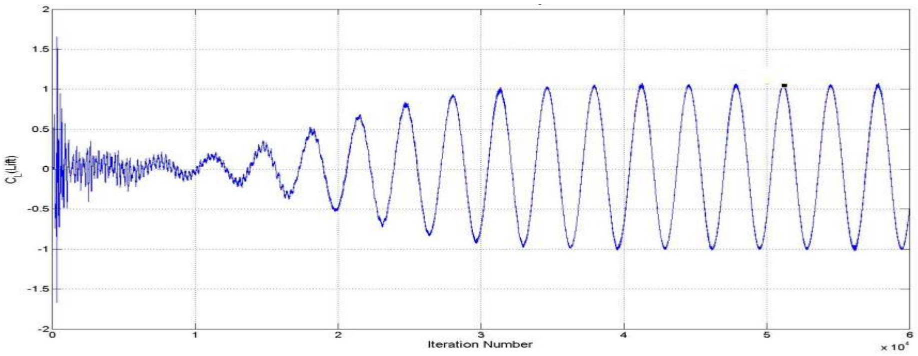

Figure 6.9 C_L values variation with iteration number (lattice units time) for Re =100.

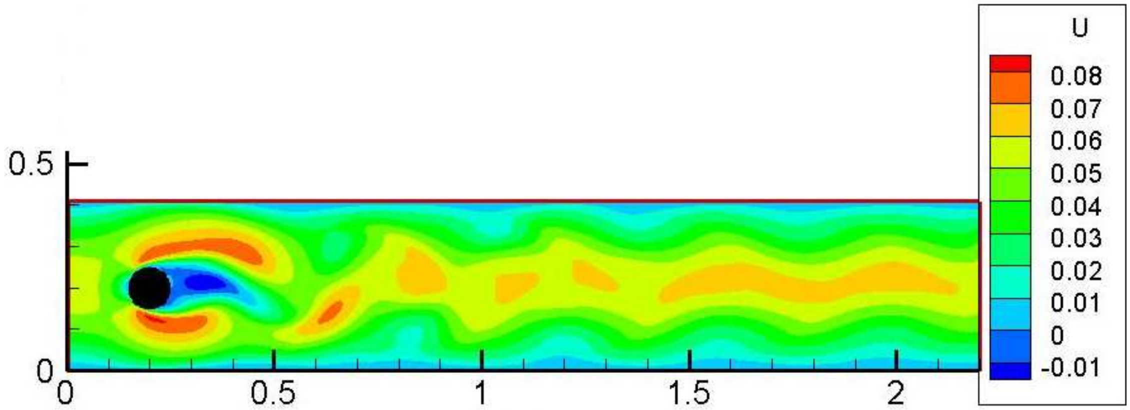

Figure 6.10 U- velocity contour plot at 58000 iteration step.

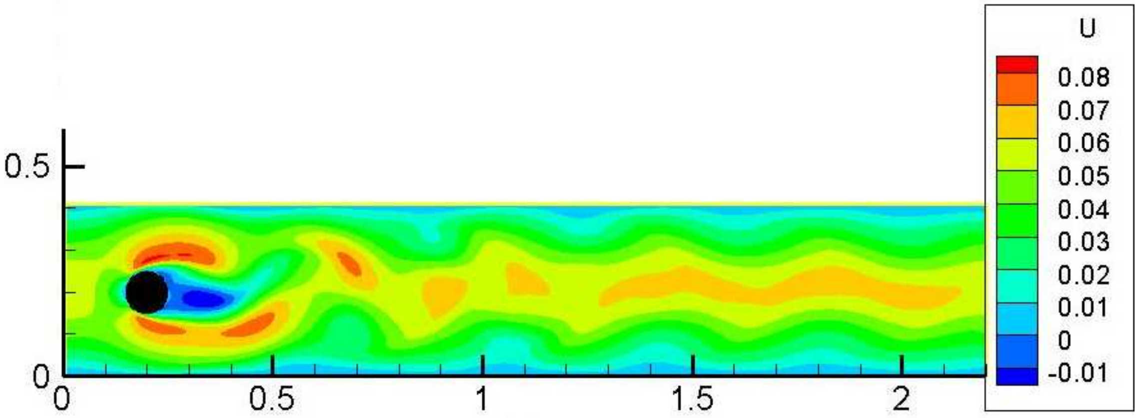

Figure 6.11 U- velocity contour plot at 60000 iteration step.

6.2.2 Flow Over a NACA0012 Airfoil

The second numerical experiment to assess the accuracy of the direct forcing IB-LBM code was the flow over the NACA0012 airfoil. The computation was conducted for Re=500. The multi-block LBM was used for mesh refinement around the airfoil as shown in Figure 6.12a-b. Figure 6.12a shows the airfoil within the finer grid while Figure 6.12b shows a zoomed view into the fine grid. The D2Q9 lattice model was used for the discretization of the fluid domain. The airfoil was placed sufficiently away from the outer boundary of the computational domain. The far field boundary conditions were implemented in LBM by setting the particle distribution function to its equilibrium distribution function. The resulting flow field in the whole computational domain is shown in Figure 6.13a while the flow field in the neighborhood of the airfoil is shown in Figure 6.13b. The comparison between the drag coefficient obtained from the current work using the direct forcing IB-LBM and that published in literature (Lockard et al. 2002) is shown in Table 6.4.

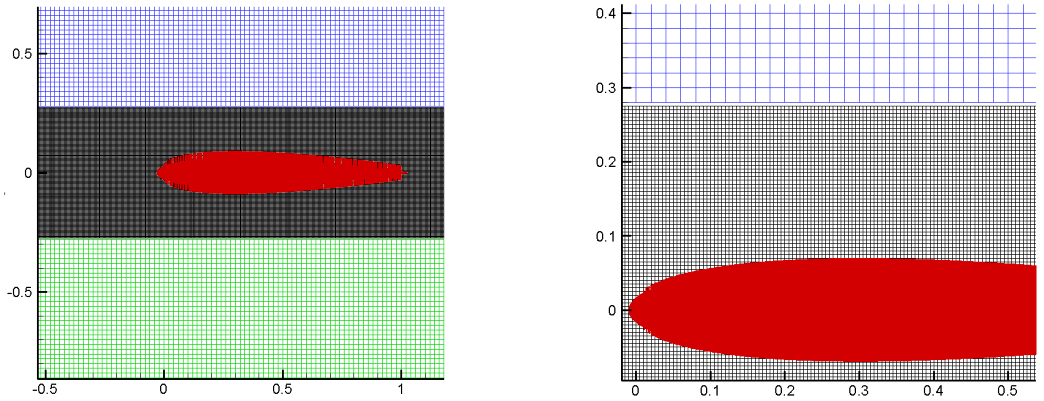

(a) (b)

Figure 6.12 Multi-block meshing for NACA0012 airfoil.

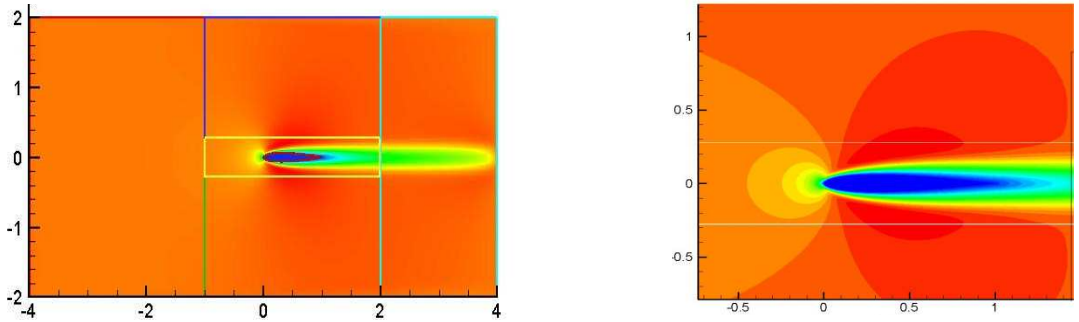

(a) (b)

Figure 6.13 U-velocity contour plot for flow over NACA0012.

Table 6.4 Drag coefficient for NACA 0012 using the direct forcing IB-LBM for Re=500

	Current Work	Lockard et al. 2002
C_D	0.1781	0.1762

6.3 Validation of the Direct Forcing IB-LBM Code for Flexible/Elastic Bodies

The current section is used to validate the direct forcing IB-LBM for the simulation of flows with flexible and elastic boundaries. The current section also serves the purpose of validating the proposed partitioned multiphysics coupling scheme within the LBM computational framework.

6.3.1 FSI Over an Idealized Heart Valve Leaflet Using Direct Forcing IB-LBM

The transient FSI numerical benchmark case is the flow over an aortic heart valve leaflet. The heart valve leaflet is idealized by the computational geometry shown in Figure 6.14. The idealized geometry shown in Figure 6.14 have been used by a couple of authors to assess the validity of their FSI algorithm using the Fictitious Domain Method (Baaijens 2001 and Yu 2005) and Immersed Finite Element Method (Zhang et al. 2007) and also in understanding the opening and closing of the aortic valve. The heart valve leaflet is modeled as a thin structure with a thickness of 0.0212cm and height of 0.8cm. The Young's modulus of the leaflet was 10^7 dyne/cm^2. The density and Poisson's ratio of the leaflet was 6g/cm^3 and 0.5. The density of the fluid was 1 g/cm^3 with a kinematic viscosity of 1 Stoke, or 1 cm^2/s. The leaflet was clamped at midpoint of the flow channel. The flow channel height was 1 cm, while the channel length is 4 cm. No-slip boundary conditions was applied to lower wall Γ_2 while symmetry boundary conditions was applied along the top wall Γ_4.

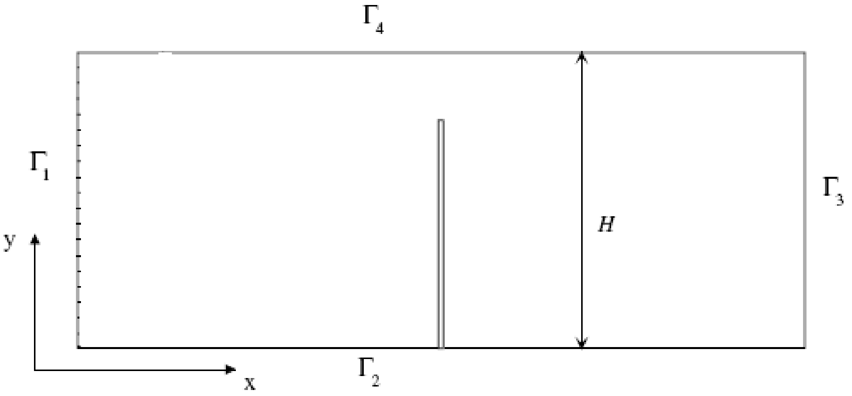

Figure 6.14 Schematic of the flow domain for the idealized aortic valve leaflet.

A sinusoidal axial velocity profile was prescribed at the inlet boundary Γ_1 as shown in Eq. (6.14)

$$U = U_o \sin(2\pi ft + 0.5\pi) \tag{6.14}$$

where t, f and U_o denote the time, frequency and amplitude of the sinusoidal velocity input, respectively. The fluid domain was discretized using a D2Q9 lattice model. The 8 noded plane strain hybrid element with reduced integration (CPE8RH) element was used in ABAQUS for the solid discretization. Direct integration was used for the time integration of the equation of motion (Eq. 5.42) for the solid using the HHT integrator (Hilber et al. 1998) integrator with α =-0.05. Numerical computations were conducted for St = 1.0 and 0.5, Re =1 and 10, where Re and St are as defined in Eq. (6.15) and Eq. (6.16) respectively.

$$\mathrm{Re} = \frac{U_o H}{\nu} \tag{6.15}$$

$$St = \frac{fH}{U_o} \tag{6.16}$$

The plot of leaflet tip position versus normalized time is shown on Figure 6.15, the time is normalized by the period T of sinusoidal velocity input. Figure 6.15 also helps to assess the quantitative agreement between the current work and the published results of Zhang et al. 2007. Figure 6.16 gives a qualitative assessment of the current results by looking at the effects of Re and St on the tip position (or displacement). The leaflet is deformed or displaced more for lower frequency (St =0.5) than higher frequency (St=1). This is because there is more time for the leaflet to reach its fully flexed position for lower frequency than the higher frequency velocity as shown in Figure 6.16. There is a slight increase in displacement with increasing Re but the dominant effect on the displacement is the St number for the parameter ranges that were tested. The same qualitative assessment was observed in published results of Zhang et al. Figures 6.17a-d shows the x-velocity contour plot superimposed upon the velocity vector at different times for the case of Re=10, St=0.5. The same qualitative assessment was observed in published results of Zhang et al. Figures 6.17a-d shows the x-velocity contour plot superimposed upon the velocity vector at different times for the case of Re=10, St=0.5.

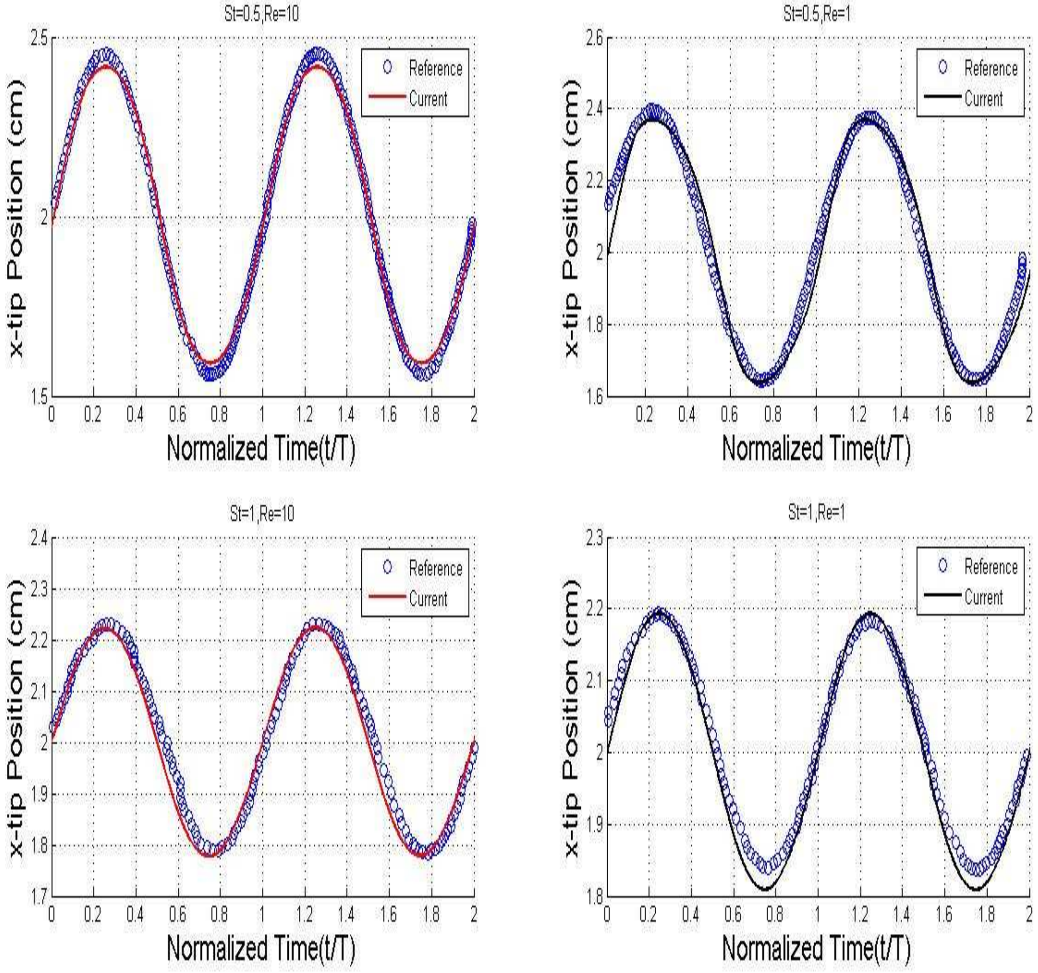

Figure 6.15 Comparison between the leaflet tip position using Direct Forcing IB-LBM and the results of Zhang et al. 2007.

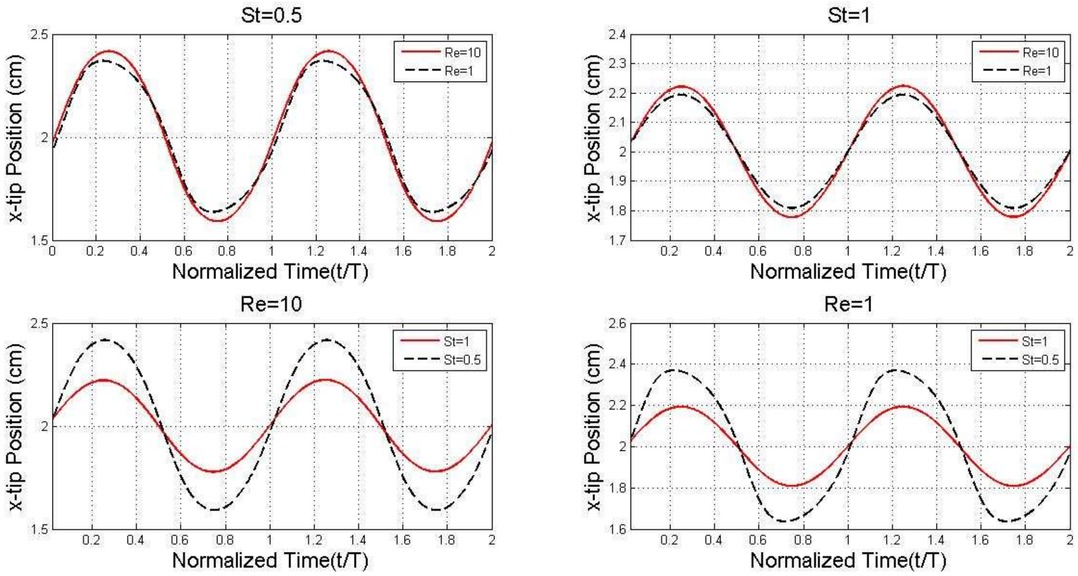

Figure 6.16 Effects of Re and St on the leaflet tip position or displacement.

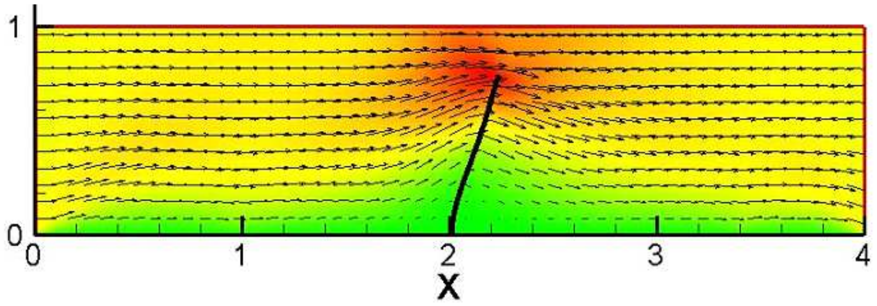

Figure 6.17a Leaflet at t=0.1T for Re=10, St=0.5.

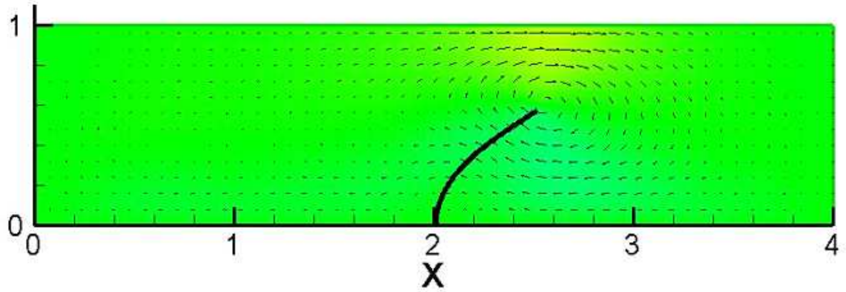

Figure 6.17b Leaflet at t=0.25T for Re=10, St=0.5.

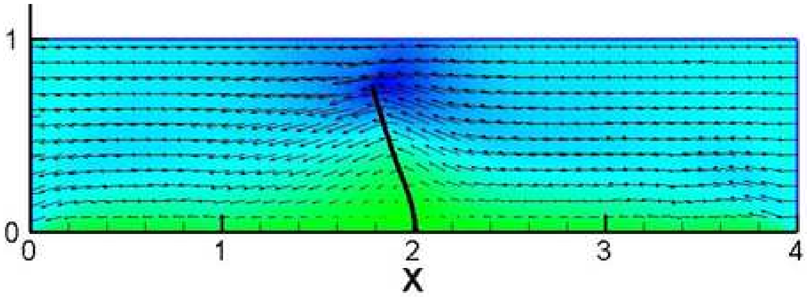

Figure 6.17c Leaflet at t=0.6T for Re=10, St=0.5.

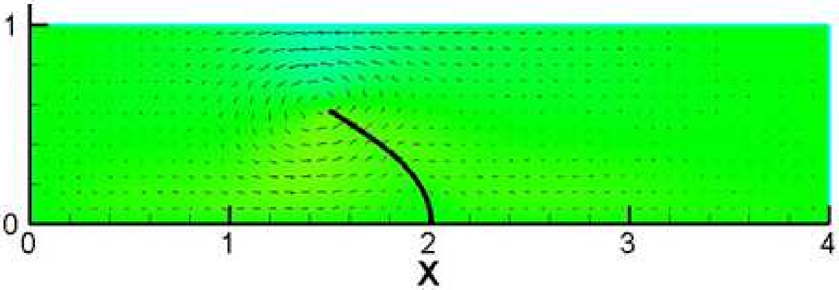

Figure 6.17d Leaflet at t=0.75T for Re=10, St=0.5.

6.4 Validation of the New Direct Heating IB-LBM

The major contribution of the current work is the development of the direct heating IBM within the Lattice Boltzmann computational framework and also a new method of handling the constant heat flux boundary condition for immersed boundary method problems with heat transfer. The current section seeks to validate the accuracy of the direct heating IB-LBM. The accuracy and the validity of the proposed approach were evaluated by comprehensive comparisons of the results obtained by the direct heating IB-LBM code with existing published flow cases and their results. The validated numerical tool was then applied to natural and forced convection flows of immersed bodies.

6.4.1 Natural Convection in a Square Enclosure with an Immersed Circular Cylinder

The first numerical experiment conducted to evaluate the direct heating IB-LBM method is the natural convection in a square cavity with an immersed circular cylinder. This problem has been investigated by several authors (Jeong et al. 2010; Kim et al. 2007; Shu et al. 2002; Peng et al. 2003 and Moukalled et al. 1996). Figure 6.18 shows a schematic of the geometry and flow domain. The cylinder with radius 0.2 length unit is centrally located in the cavity with unit length. The walls of the cavity and cylinder are stationary; the cavity walls are at a lower temperature T_{cold} than the cylinder temperature T_{hot}. The gravity **g** acts along the negative y- direction. The IB-LBM was used for implementation of both the no-slip and isothermal boundary conditions on the circular cylinder while the conventional bounce-back condition was used for the cavity walls.

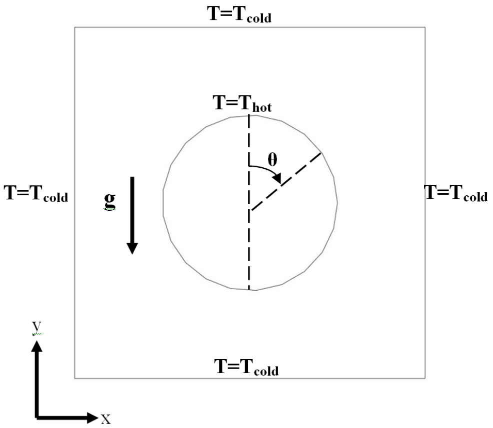

Figure 6.18 Schematic of the flow domain and geometry for natural convection test case.

The fluid flow in the square cavity is natural convection dominated. Numerical experiments were performed for Rayleigh numbers *Ra* of 10^4, 10^5 and 10^6, Prandtl number Pr =0.7, and the corresponding Re of 119, 375 and 1187 as defined in Eq. (6.17)

$$Ra = \mathrm{Re}^2\,\mathrm{Pr} = \frac{g\beta\left(T_{hot} - T_{cold}\right)L^3}{\nu\alpha} \tag{6.17}$$

where β and L denote the expansion coefficient and cavity height, respectively. The Boussinesq approximation was used to account for the buoyancy effects. The buoyancy force $\mathbf{F_b}$ in Eq. (6.18) is included in the momentum equations as a body force.

$$\mathbf{F_b} = \rho\mathbf{g}\beta\left(T - T_{cold}\right) \tag{6.18}$$

The results provided below are those obtained by using a 201 X 201 lattice grids of the D2Q9 lattice structure. Cases with three different Rayleigh numbers were simulated. Table 1 compares the calculated surface averaged Nusselt number Nu with the previously published results that used the feedback IB-LBM (Jeong et al. 2010), finite volume methods(Kim et al. 2007; Shu et al. 2002 and Moukalled et al. 1996) and least-squares-based LBM methods (Peng et al. 2003). The results of the present work are in a good agreement with the data. The comparison provides a quantitative assessment of the present formulation and numerical tools. Figures 6.19-6.21 shows, respectively, the isotherms, the streamlines and the velocity components contours at the various Rayleigh numbers.

Table 6.5 Comparison of the Nusselt number for natural convection flow with a square cavity using direct heating IB-LBM with existing published data

Ra	Present Work	Jeong et al	Kim et al	Shu et al	Peng et al	Moukalled et al
10^4	3.287	3.412	3.414	3.24	3.24	3.331
10^5	5.081	5.176	5.138	4.86	4.84	5.08
10^6	9.278	9.171	9.39	8.9	8.75	9.374

For the lowest Rayleigh number case calculated ($Ra=10^4$), the heat transfers via diffusion is evidenced by the rather uniform distribution of the temperature gradient around the cylinder. The fluid, heated by the cylinder, convects upward to the top wall and flows back down along the side wall, setting up a convective flow pattern. Figure 6.19(b) shows that the circulatory nature of the flow produces a pair of vortical flows that are symmetric with respect to the major meridian of the cylinder. The strength of the convective flow, in terms of the velocity magnitudes, increases with the increasing Ra. As shown in Figure 6.22a, the maximum local Nusselt number Nu_l occurs at the top of the cylinder ($\theta=0$) for $Ra=10^4$. At $Ra=10^5$, flow convection is more significant and the thermal boundary layer on the surface of the cylinder becomes thinner. This leads to a wider region of higher temperature in the upper portion of the enclosure, compared with that in the lower portion (Figure 6.20). There is only a single core in the vertical flow pattern, as opposed to the double core pattern observed in the case of $Ra=10^4$. A thermal plume occurs above the top of the cylinder as shown in Figure 6.20a. The thermal plume at the top of the cylinder changes the Nu_l profile on the surface of the cylinder for $Ra=10^5$ when compared to the profile at $Ra=10^4$. Nu_l is the lowest at $\theta=0$ for $Ra=10^5$. Nu_l increases with increasing θ until it reaches a peak at the bottom of the cylinder ($\theta=\pi$). Convective heat transfer plays a dominant role at Ra=10^6 with the thinning of the boundary layer on a large portion of the surface of the cylinder. Compared to the Ra=10^5 case, there is a formation of a stronger plume as shown in Figure 6.21a, consequently, resulting in further reduction of Nu_l at $\theta=0$ as shown in Figure 6.22a. The case with Ra=10^6 exhibits a Nu_l profile that is similar to that with Ra=10^5. The surface heat transfer, however, is further enhanced at Ra=10^6. The stronger plume impinges on the top wall of the enclosure, thereby reducing the thermal boundary layer on the top wall and consequently leading to increased heat transfer in this region. The stronger convective flow present also leads to the boundary later separation near the center of the bottom wall(X=0.35 to 0.65) as shown in Figure 6.22b. Figure 6.22b shows the plot of the wall shear stress in LBM units along the bottom wall, the boundary layer separation in the region X=0.35 to 0.65 leads to the formation of two symmetric vortices as shown on the embedded streamlines in Figure 6.22b. The changes of the flow patterns with the Rayleigh number observed and discussed here have also been reported in literature (Jeong et al. 2010; Kim et al. 2007,; Shu et al. 2002; Peng et al. 2003 and Moukalled et al. 1996). It should also be noted that results of the current simulation show steady flow pattern for all three cases, which also is in agreement with the observation made in the previous studies.

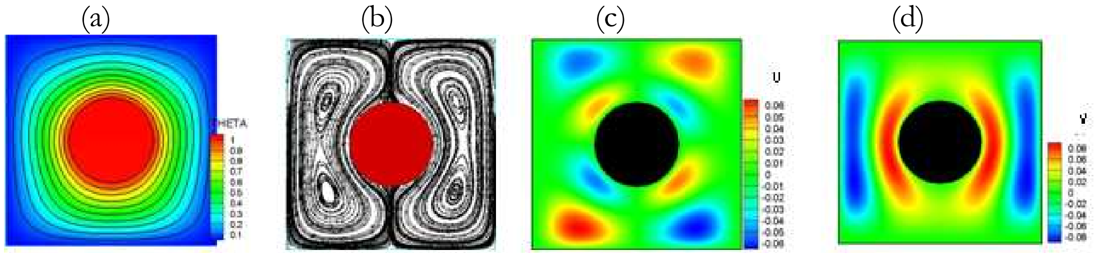

Figure 6.19 Ra=10^4 (a) isotherms; (b) streamlines; (c) velocity component U; (d) velocity component V.

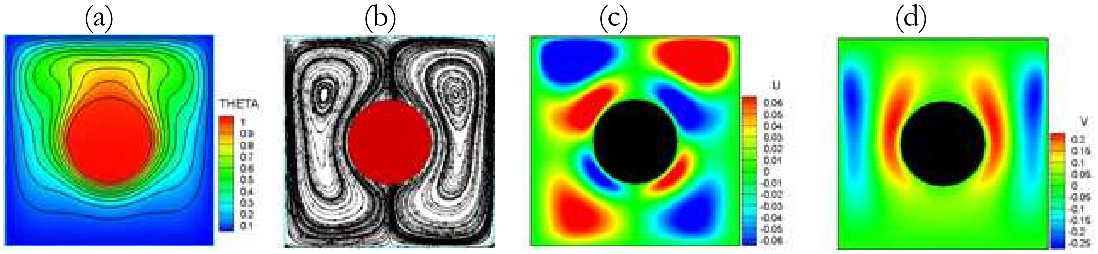

Figure 6.20 Ra=10^5 (a) isotherms; (b) streamlines; (c) velocity component U; (d) velocity component V.

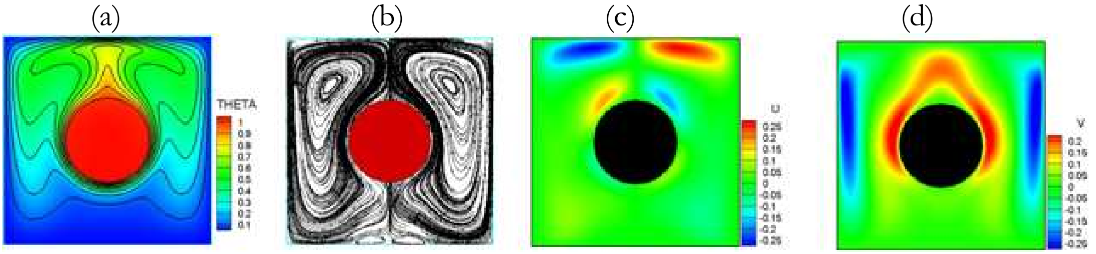

Figure 6.21 Ra=10^6 (a) isotherms; (b) streamlines; (c) velocity component U; (d) velocity component V.

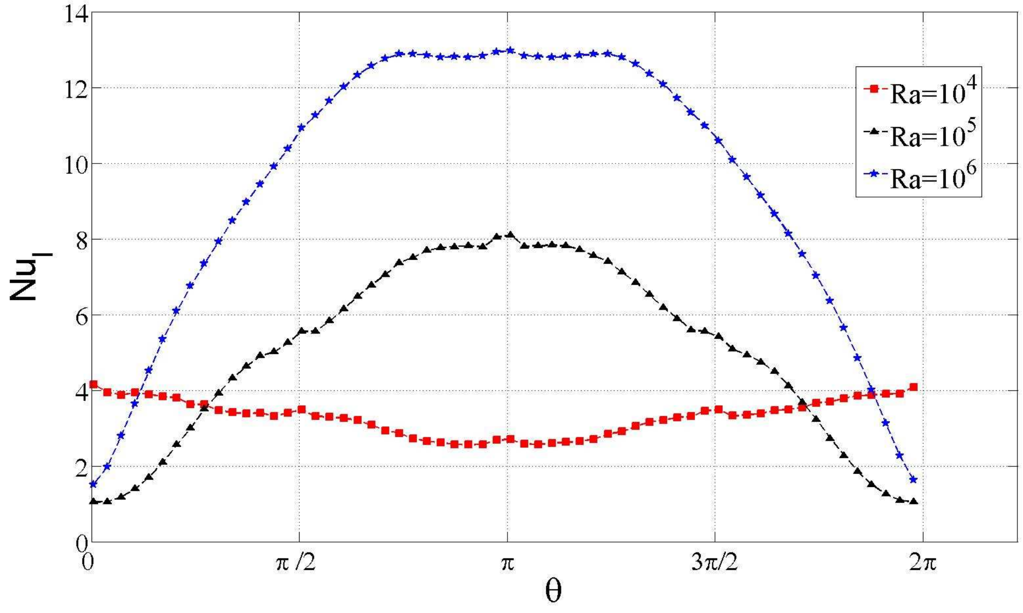

Figure 6.22a Variation of the local Nusselt number on the surface of the cylinder.

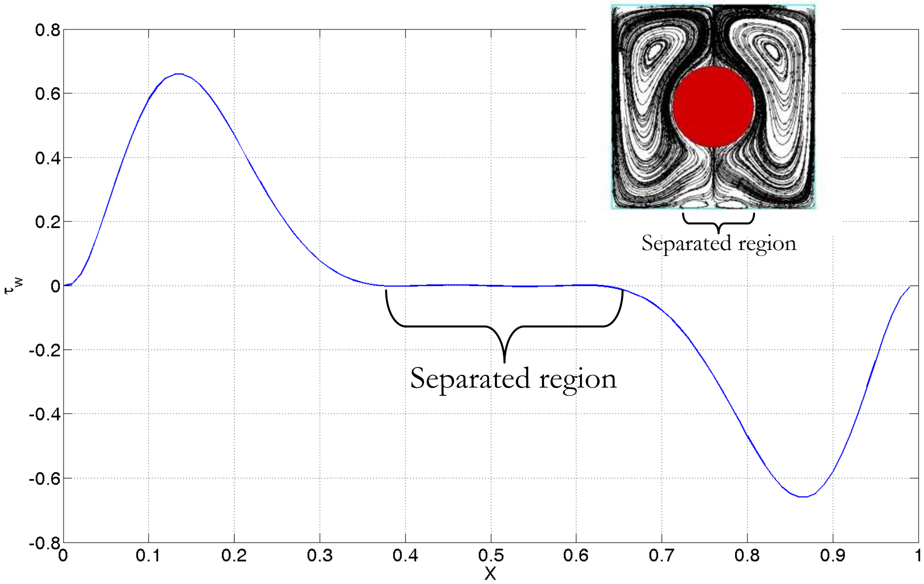

Figure 6.22b Wall shear stress plot at the lower wall showing the separated region.

6.4.2 Forced Convection in a Channel with Immersed Boundaries

The two simulations shown in this section are for incompressible flows in a confined channel with a heated immersed square and triangular cylinder, respectively. The Reynolds number of the flow studied here allows the flow to exhibit from small to massive flow separation. At the highest Reynolds number calculated for the flow over the triangular cylinder, the flow becomes unsteady and periodic vortex shedding was captured. The cases are similar to the case of blockage ratio $\beta = 0.25$ in Dhiman et al. 2005 and Srikanth et al. 2010. Figure 6.23 shows the flow domain and the boundary conditions for the square cylinder and Figure 6.24 for the triangular cylinder. A parabolic velocity profile was prescribed at the inlet. No-slip velocity and adiabatic thermal boundary conditions were applied to the top and bottom walls. Convective boundary conditions were applied for velocity and temperature at the outlet to allow the flow to freely convect out of the computational domain. All simulations were performed for Pr =0.7 and the inlet temperature T_i =0.

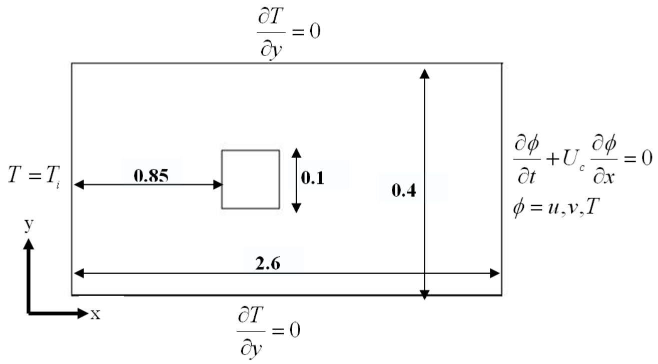

Figure 6.23 Schematic of the square configuration.

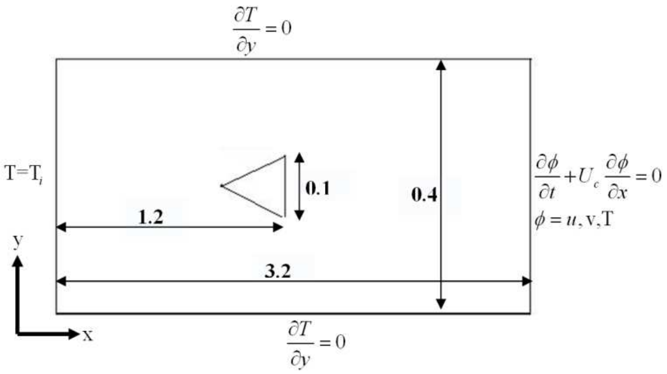

Figure 6.24 Schematic of the triangle configuration.

6.4.2.1 Immersed Square

The Reynolds number of the flow simulated ranges between 5 and 45, with an increment of 5. Cases with constant temperature (CT) and cases with constant heat flux (CHF) boundary conditions at the boundary surface of the immersed square were studied. For the constant surface temperature cases, the surface temperature was set at T_h =1. For the constant surface heat flux case, the heat flux was set at $q''=0.1$

Constant Surface Temperature

Figure 6.25 shows the isotherms for different Re while Figure 6.26 shows the contour plot of the velocity components and streamlines. The variation of the local Nusselt number along the surface of the square is shown in Figure 6.27, only the upper half of the geometry was considered in Figure 6.27 due to symmetry about the y-axis. The point A corresponds to the midpoint of the square on the front surface, the line A-B represents half of the front surface, line B-C represents the top surface while line C-D represents the half of the trailing edge. The thermal boundary layer on the square cylinder is thinnest at the front surface, as indicated by the crowding of the isotherms in Figure 6.25, hence the heat transfer is highest at the front surface as indicated by the higher Nu_l number on face A-B on Figure 6.27 relative to other surfaces. The crowding of the isotherms or thermal gradient decreases as the flow moves along the side surfaces and the thermal boundary layer grows, consequently the heat transfer reduces as the flow moves along the top surface (line B-C) towards the trailing edge as shown in Figure 6.27. Flow separation occurs at the trailing edge and leads to the formation of recirculation zone with two symmetric vortices as shown in Figure 6.26. The length of the recirculation zone increases with increasing Re. The heat transfer is minimum at the trailing edge (line C-D) due flow separation. The heat transfer on the faces of the square cylinder increases with increasing Re as shown in Figure 6.27, the influence of Re on the heat transfer is minimal at the trailing edge for the constant temperature boundary condition case.

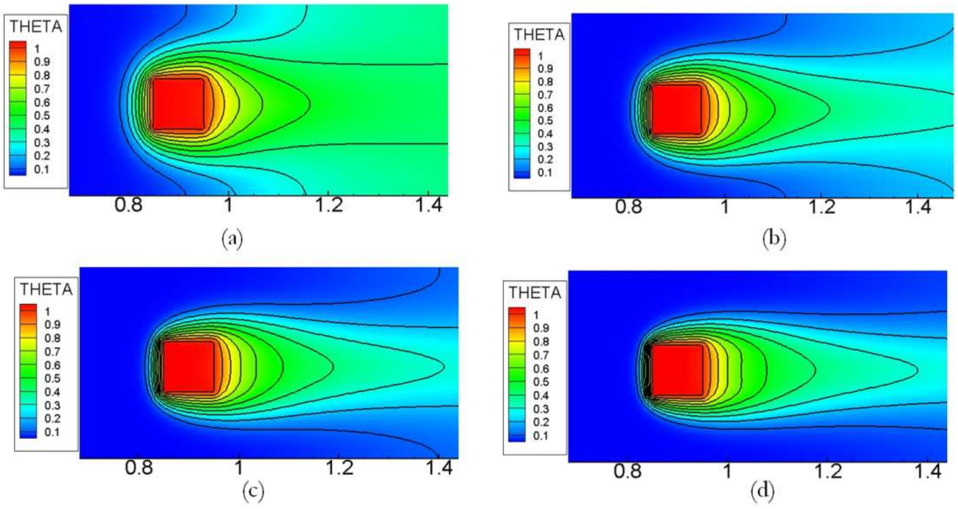

(a) (b) (c) (d)

Figure 6.25 Isotherms for flow over a square cylinder. (a) Re=10; (b) Re=20; (c) Re=30; (d) Re=40.

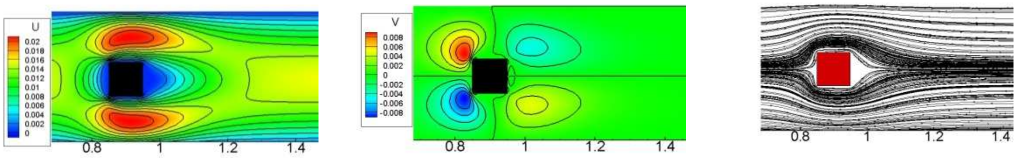

Figure 6.26a Contours of velocity components U and V, streamlines for Re=10.

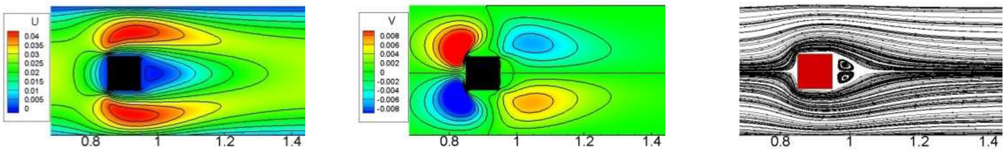

Figure 6.26b Contours of velocity components U and V, streamlines for Re=20.

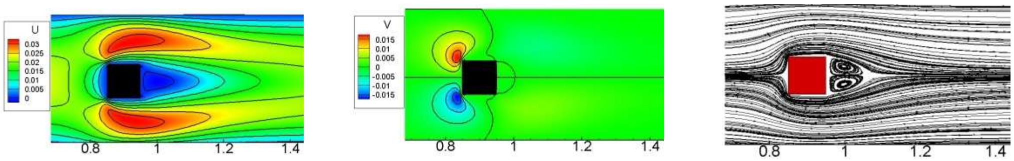

Figure 6.26c Contours of velocity components U and V, streamlines for Re=30.

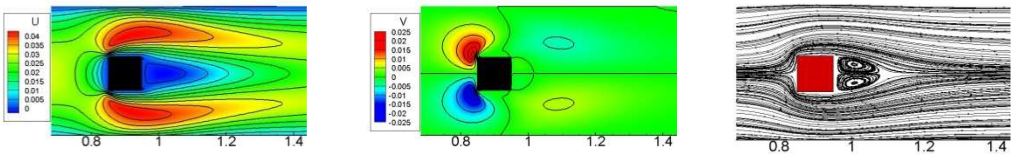

Figure 6.26d Contours of velocity components U and V, streamlines for Re=40.

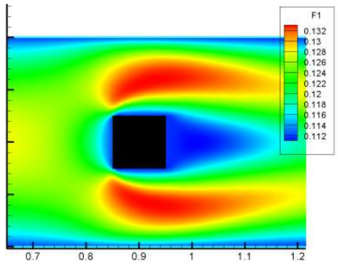

Figure 6.26e f_1 contour plot.

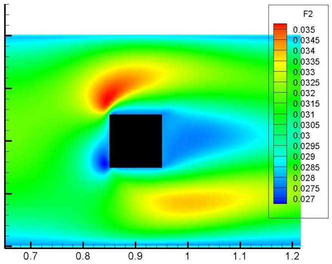

Figure 6.26f f_2 contour plot.

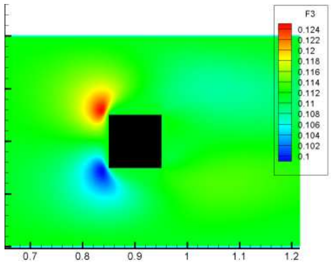

Figure 6.26g f_3 contour plot.

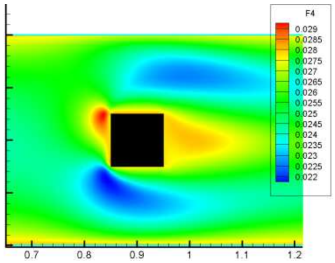

Figure 6.26h f_4 contour plot.

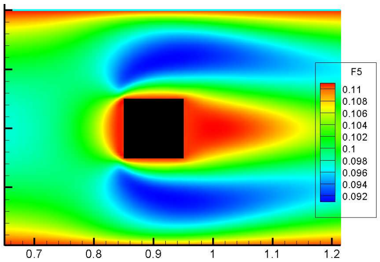

Figure 6.26i f_5 contour plot.

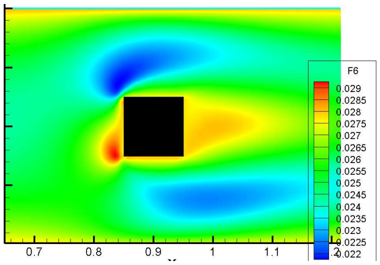

Figure 6.26j f_6 contour plot.

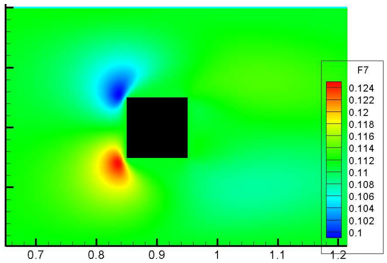

Figure 6.26k f_7 contour plot.

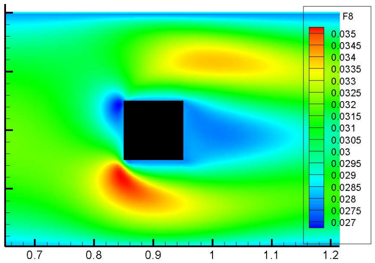

Figure 6.26l f_8 contour plot.

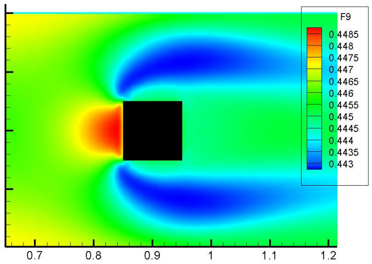

Figure 6.26m f_9 contour plot.

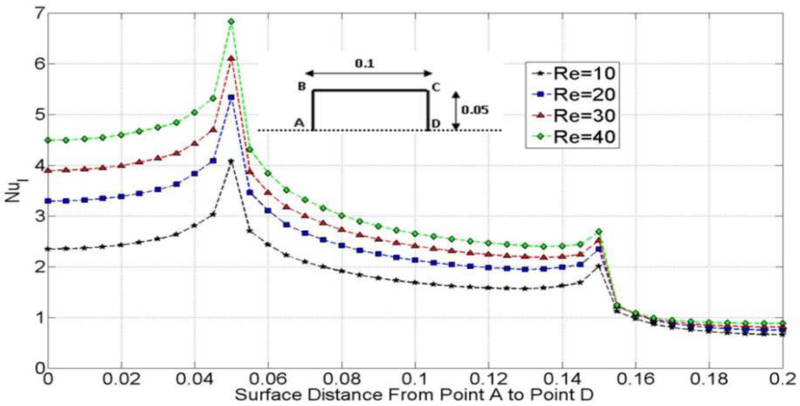

Figure 6.27 Local Nusselt number variation along the surface of square cylinder at constant temperature boundary condition.

Constant Surface Heat Flux

The new constant heat flux boundary condition implementation introduced by the author (section 4.2.1) will be validated with current test case. Figure 6.28-6.29 shows Nu_l

and the temperature variation along the surface of the square cylinder for the CHF. Qualitatively, the variation of Nu_l with CHF is similar to that with CT boundary condition, as shown in Figure 6.28. There is an inverse relationship between the surface temperatures and Nu_l as shown in Figure 6.28-6.29,; that is, the higher the heat transfer the lower the surface temperatures. The surface temperatures are highest at the trailing edge due to flow separation at this location. Comparison of the heat transfer characteristic for both the CHF and CT boundary conditions for Re=10 and Re=40 is shown in Figure 6.30. The CT boundary condition has a better heat transfer at the front surface than the CHF boundary condition while CHT has a higher heat transfer rate on the top and rear surfaces. The reduction in the Nu_l at the trailing edge due to flow separation is less severe for the CHT when compared to the CT boundary condition, as shown in Figure 6.30. Figure 6.31 shows the quantitative comparison of Nu obtained in the present study with the published results (Dhiman et al. 2005). There was good agreement between the present results and the published results. The CHF boundary condition has a higher heat transfer than the CT, as signified by the higher surface averaged Nusselt number shown in Figure 6.31 and the superior performance increases with increasing Re. As discussed earlier, this is due to the relative small reduction of the local Nu_l at the trailing edge for CHF compared with those with the CT boundary condition.

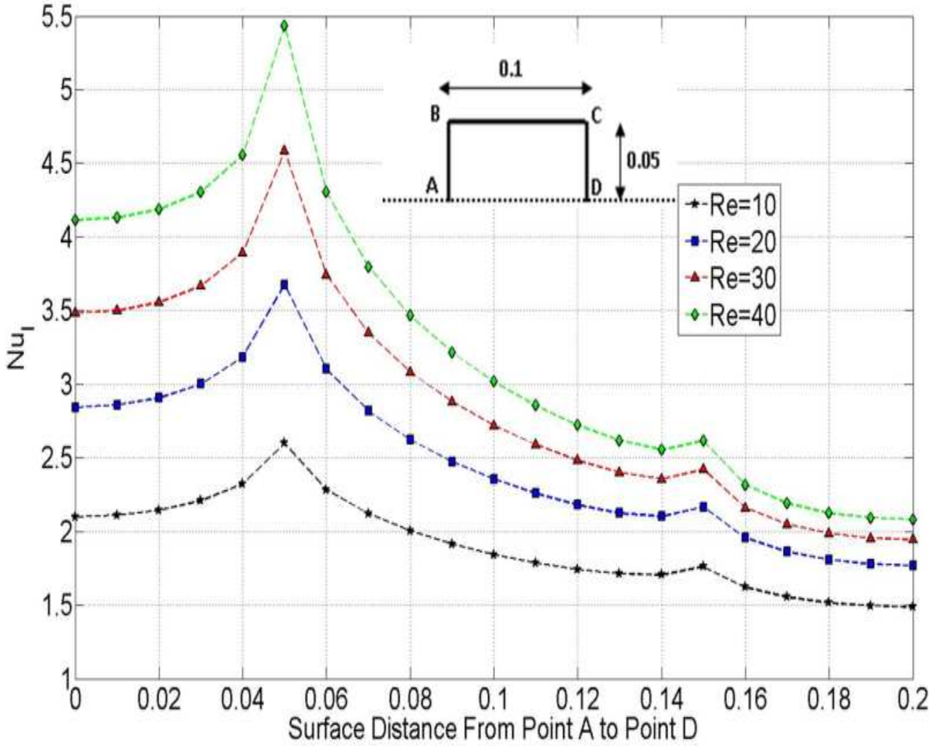

Figure 6.28 Local Nusselt number variation along the surface of square cylinder at constant heat flux boundary condition.

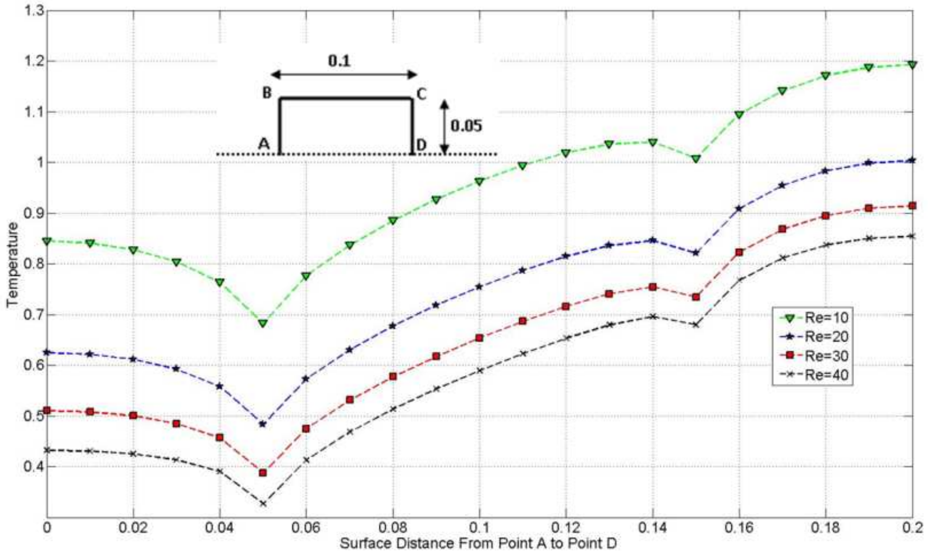

Figure 6.29 Temperature variation along the surface of square cylinder at constant heat flux boundary condition.

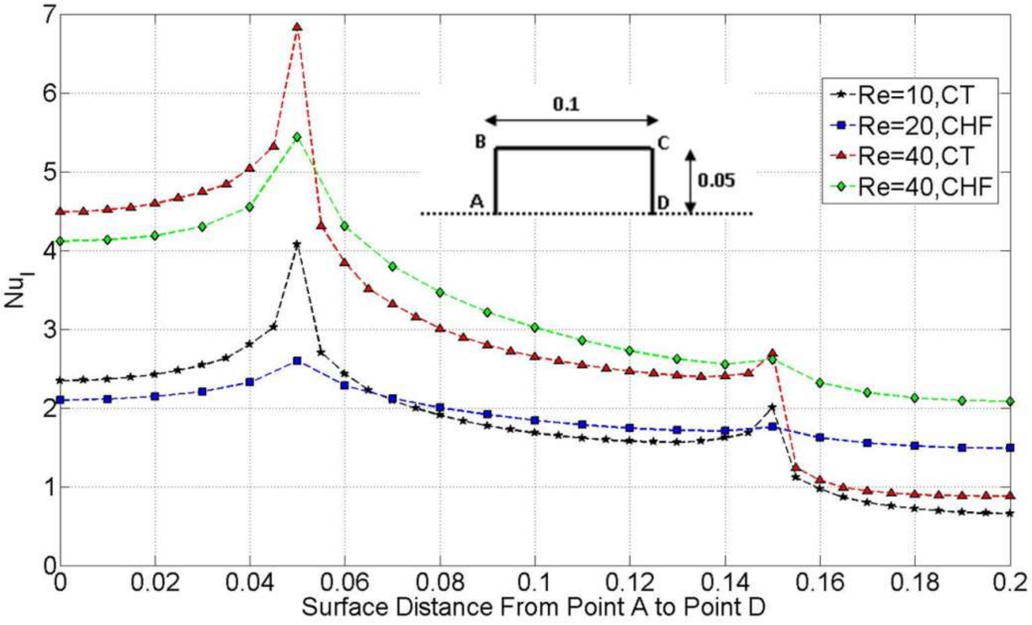

Figure 6.30 Comparison of the local Nusselt number variation along the surface of square cylinder for constant heat and temperature boundary conditions.

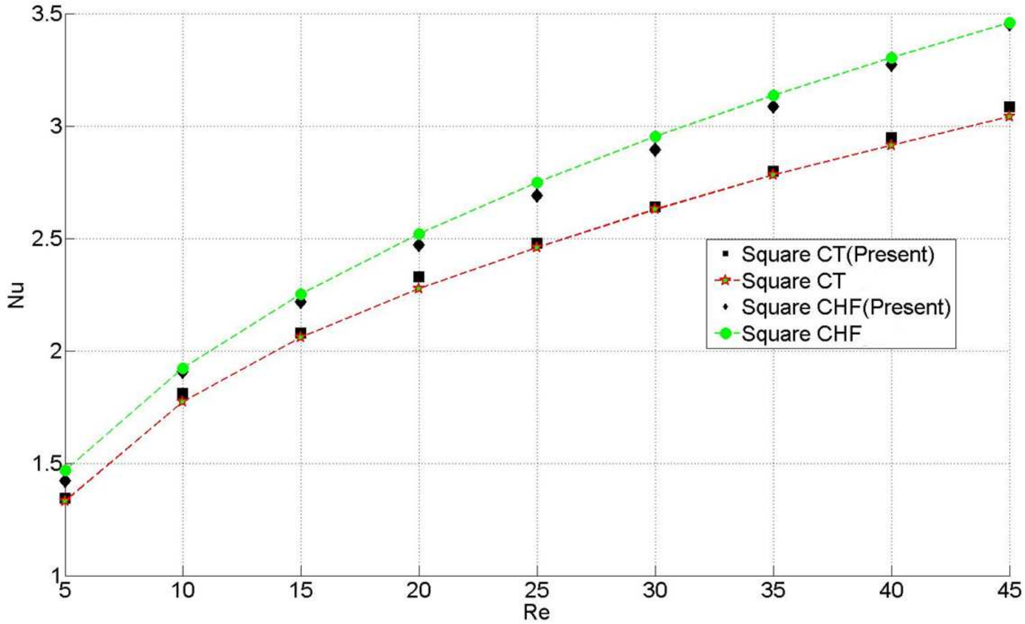

Figure 6.31 Variation of Nu with Re for square cylinder and comparison of present results with benchmark results of Dhiman et al. 2005.

6.4.2.2 Immersed Triangle

The Reynolds number of the thermal flow calculated ranges from 10 to 80. At the surface of the triangular cylinder, a constant temperature boundary condition was applied. For Reynolds number below 59, the flow is steady. Beyond Re=59, temperature and von Kármán vortex streets are formed behind the triangular cylinder with a shedding frequency ω and period T. Figure 6.32a-b shows the variation in the lift coefficient C_L with time for unsteady cases at Re=70 and 80. The period T was determined from two successive peaks of the lift coefficient while the frequency ω is obtained as the inverse of the period T. Figure 6.33a-f shows the isotherms for different Re. The isotherms indicate that the thermal boundary layer grows along the side surfaces in the flow direction. The maximum heat transfer occurs at the apex or leading of the triangle. Flow separation occurs at the trailing as shown on the streamlines in Figure 6.34. Similar to the square cylinder, two symmetric vortices forms in the recirculation zone when Re<59 with recirculation length increasing with Re. Figure 6.35a-f shows the velocity contour and streamline at Re=80 which shows characteristics features of an unsteady flow. The surface averaged Nusselt numbers Nu for the triangle and circular cylinder are shown in Figure 6.35g. The Nu increases with increasing Re number due to the thinning of the thermal boundary layer. The present Nu results agree well with the Nu reported in f Srikanth et al. 2010. Table 6.6 and Table 6.7 show the variation of the RMS (root mean square) values of the lift coefficient and the Strouhal number with Re and their comparison with existing published data.

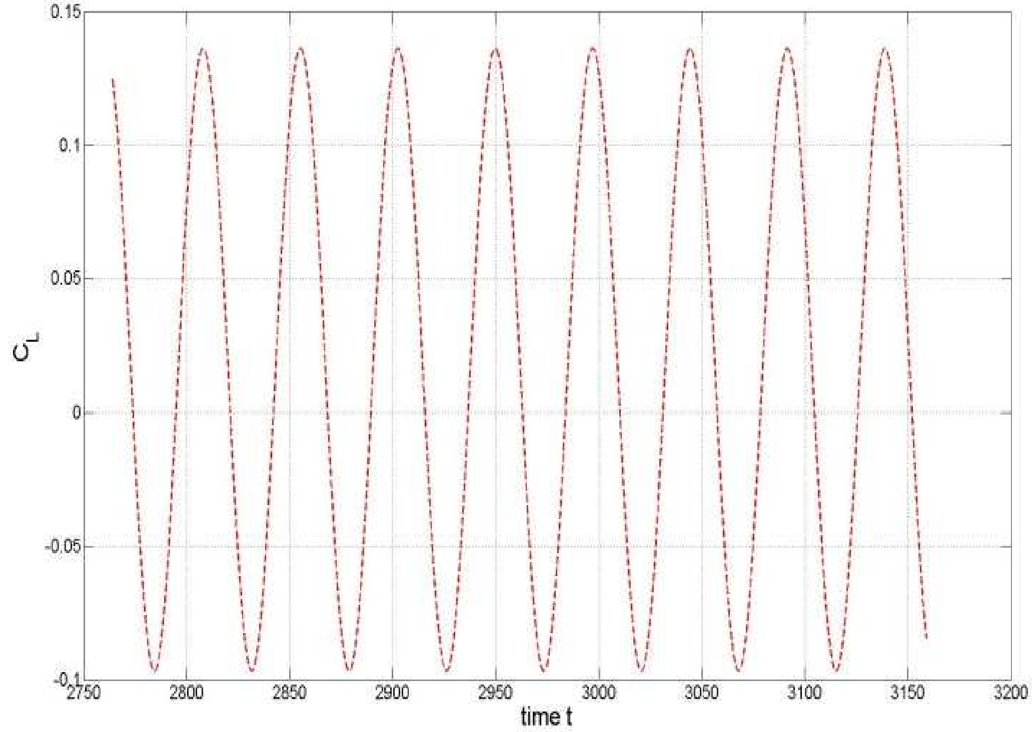

Figure 6.32a Lift coefficient for Re=70.

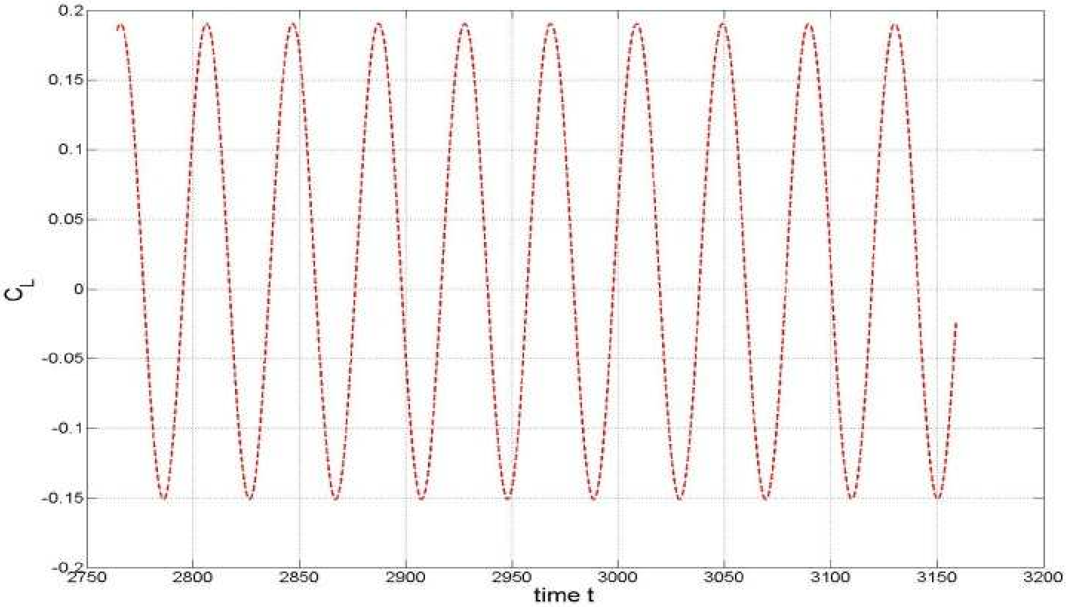

Figure 6.32b Lift coefficient for Re=80.

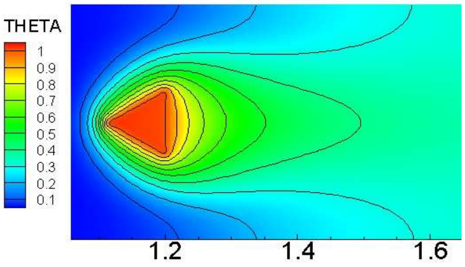

Figure 6.33a Isotherms at Re=10.

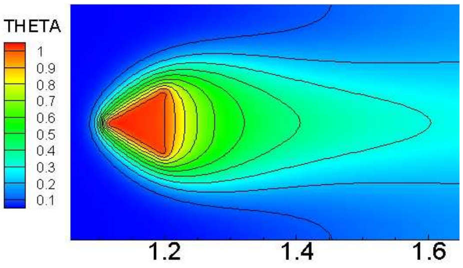

Figure 6.33b Isotherms at Re=20.

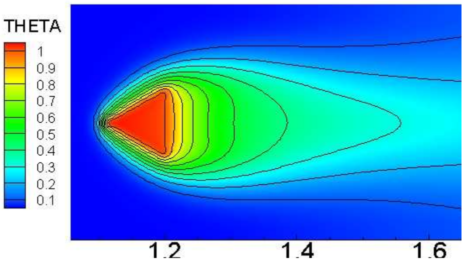

Figure 6.33c Isotherms at Re=30.

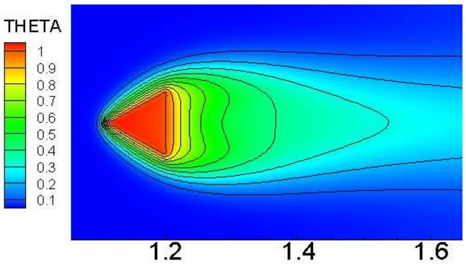

Figure 6.33d Isotherms at Re=40.

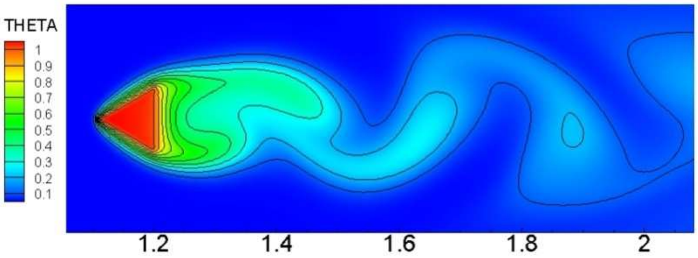

Figure 6.33e Isotherms at Re=80, t=T.

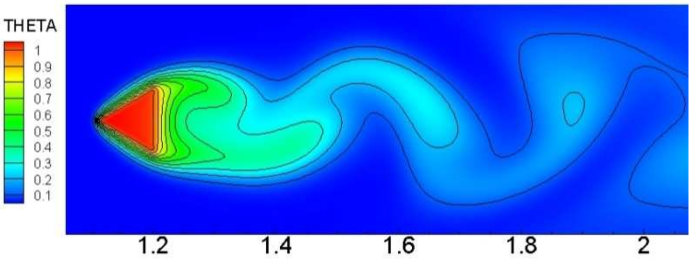

Figure 6.33f Isotherms at Re=80, t=0.5T.

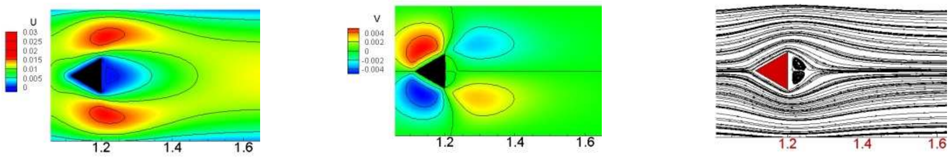

Figure 6.34a Contours of velocity components U and V, streamlines for Re=10.

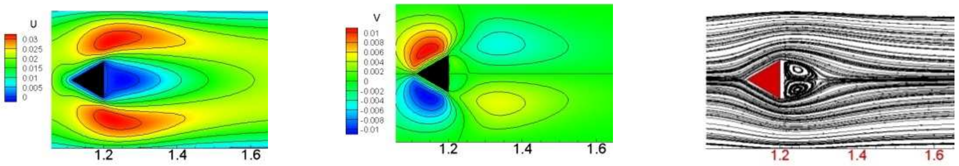

Figure 6.34b Contours of velocity components U and V, streamlines for Re=20.

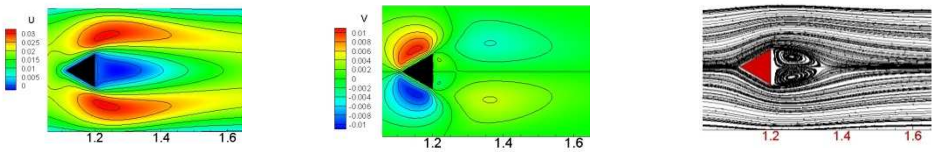

Figure 6.34c Contours of velocity components U and V, streamlines for Re=30.

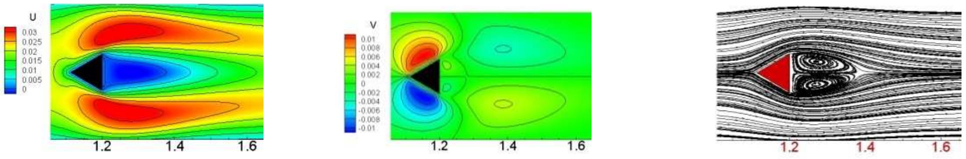

Figure 6.34d Contours of velocity components U and V, streamlines for Re=40.

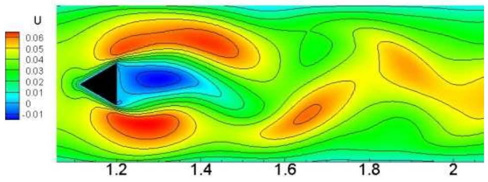

Figure 6.35a U contour at Re=80, t=T.

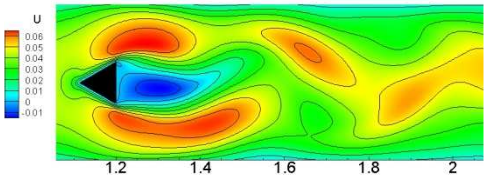

Figure 6.35b U contour at Re=80, t=0.5T.

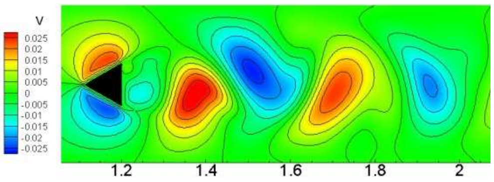

Figure 6.35c V contour at Re=80, t=T.

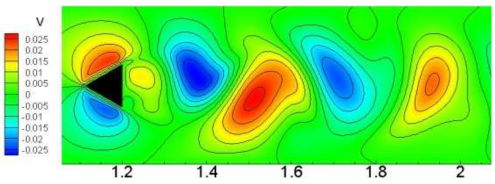

Figure 6.35d V contour at Re=80, t=0.5T.

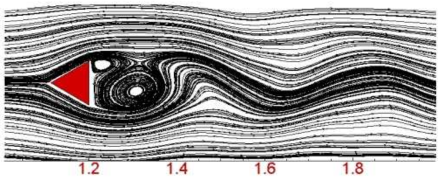

Figure 6.35e Streamlines at Re=80, t=T.

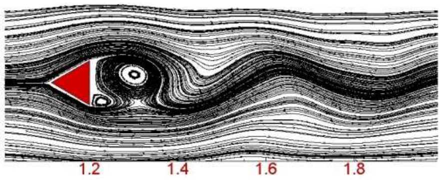

Figure 6.35f   Streamlines at Re=80, t=0.5T.

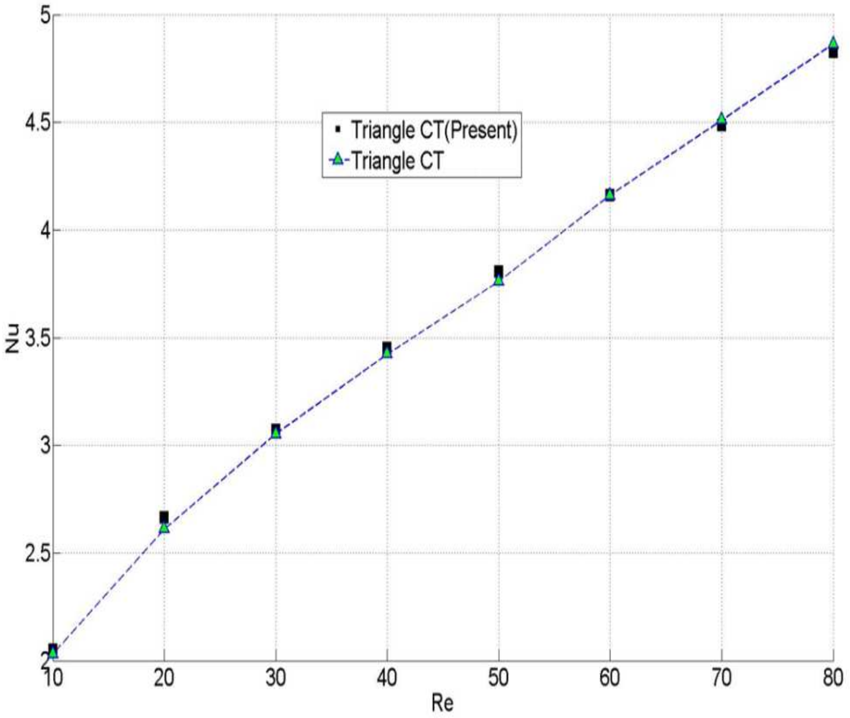

Figure 6.35g Variation of Nu with Re for triangle cylinder and comparison of present results with benchmark results of Srikanth et al. 2010.

Table 6.6 Variation of the RMS C_L with Re for triangle cylinder and comparison with published results

Re	RMS Lift Coefficient (C_L)	
	Present Work	Srikanth et al. 2010
60	0.026	0.027
70	0.084	0.085
80	0.123	0.121

Table 6.7 Variation of St with Re for triangle cylinder and comparison with published results

Re	Strouhal (St)	
	Present Work	Srikanth et al. 2010
60	0.176	0.1808
70	0.185	0.187
80	0.194	0.192

6.5 A Direct Forcing and Heating IB-LBM for Arterial Wall Thermography

The extensively validated direct forcing and heating IB-LBM method developed is applied to arterial wall thermography modeling. The proposed method is used to study the effect of plaque geometric parameters, degree of stenosis and the macrophage metabolic rate on the arterial wall temperature. The arterial geometry is assumed to be a straight wall artery. Straight wall artery can typically be seen in the human abdominal aorta. The geometry of the computational domain is shown in Figure 6.36. The geometric dimension H in Figure 6.36 is the height from the inner wall of the lumen to its centerline (that is the inner radius of the artery), H_1 is the reduced inner radius due to the presence of the stenotic plaque as shown in Figure 6.36. L is the length of the artery and L_1 is the upstream location of the plaque

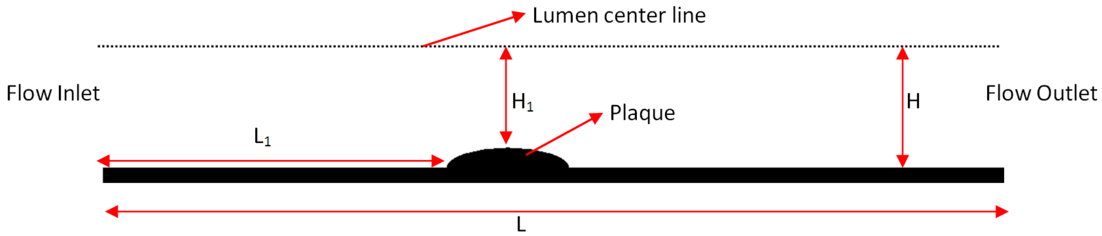

Figure 6.36 Schematic of the straight artery used for computational simulation.

The plaque geometry was assumed to be semi-elliptical in shape with the geometric parameters shown in Figure 6.37. The geometric parameters a_1 and b_1 is the length of the major axis and minor axis of the semi-elliptical plaque. Embedded within the plaque is the macrophage layer with major axis length a_2 and minor axis length of b_2. The fibrous cap is the region internal to the plaque but exterior to the macrophage layer. Vulnerable atherosclerotic plaques are characterized by thin fibrous cap layer.

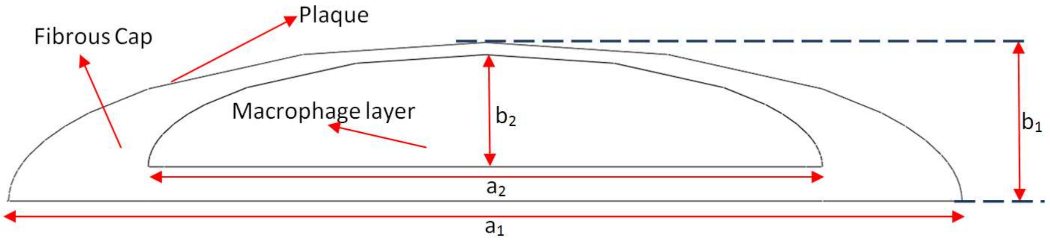

Figure 6.37 Schematic of the plaque geometry used for computational simulation.

The radius H in the current work was 1.5mm while the length L of the computational domain for the artery was set at 31mm. The wall thickness consisting of the intima, media and adventitia was 0.31mm. The intima, media and adventitia thickness were 3%, 67% and 30% of the total wall thickness. The distance L_1 was 6.58mm from the inlet to the artery. The major axis length a_1 and a_2 of the plaque and macrophage layer were assumed to be six times the minor axis length b_1 and b_2. The following geometric non-dimensional parameters Φ_h, Φ_V and Φ_S are introduced as shown in Eq. (6.19)-(6.21). Φ_h was used to characterize the nearness or distance of the macrophage layer to the arterial wall where the distance b_3 is the minimum fibrous cap thickness. The higher the value of Φ_h means that the macrophage layer is further away from the arterial wall while a lower value means a thin fibrous cap and the macrophage layer is closer to the wall.

$$\Phi_h = \frac{b_3}{b_1} \tag{6.19}$$

$$\Phi_V = \frac{\pi a_2 b_2}{\pi a_1 b_1} = \frac{a_2 b_2}{a_1 b_1} \tag{6.20}$$

$$\Phi_S = \frac{H - H_1}{H} \tag{6.21}$$

Φ_V was used to characterize the cell density of the macrophage layer and in the current study was approximated by the ratio of the areas of the macrophage layer to that of the plaque. Φ_S was used to characterize the degree of stenosis induced by the plaque. In the current study, Φ_V values of 0.25 and 0.5, Φ_h values of 0.1 and 0.3, and Φ_S values of 0.125 and 0.25 were used. The D2Q9 lattice model was used for the discretization of the computational fluid domain. Steady state computations were performed and a parabolic velocity profile was prescribed at the inlet to the flow domain. The Reynolds number Re for flow was 100. The Re=100 is close to the mean Re encountered in physiological conditions. Symmetry boundary conditions were used for the upper wall due to symmetry of the geometry, outflow boundary conditions were used at the outlet. Temperature and convective thermal boundary conditions were used at the inlet and outlet of the computational fluid domain. The inlet temperature was assumed to equal to the blood temperature of 37°C under normal physiological conditions. Adiabatic thermal boundary condition was used at the centerline due to symmetry. The direct heating IB-LBM was used for enforcing the thermal interface conditions between the lower wall and plaque while the direct forcing IB-LBM was used for enforcing the no-slip boundary condition at the lower wall. The thermal interface condition at the lower is a conjugate heat transfer problem; there is a cooling and convective effect due to blood flow and a heating effect by the macrophage layer in the solid with the heat transfer to the surface occurring via conduction. The thermal interface condition on the fluid side was a temperature boundary condition with the set temperature coming from the solid solver. The heat transfer in the solid was solved by ABAQUS. Temperature thermal boundary conditions of 37°C were used for all walls of the artery except at the interface with the lumen wall. The interface condition at the solid side was a convective boundary condition with the heat transfer coefficient and fluid sink temperature coming from the fluid solver. The multiphysics coupling scheme discussed in section 5.4 was used for the coupling between IB-LBM and ABAQUS. The blood was assumed to be Newtonian with fluid properties shown in Table. 6.8. The assumption of Newtonian fluid for blood is justifiable in medium to large arteries where the dimensions of the components of blood (erythrocytes, leucocytes and thrombocytes) are small relative to characteristic size (diameter) of the arterial vessel. There is currently no consensus on the volumetric heat

q''' by the macrophage layer, typical values that have been suggested in literature ranges from $2\text{x}10^4 \text{W/m}^3$ to $0.4 \text{ x } 10^9 \text{W/m}^3$. In the current work, q''' of $2\text{x}10^6$ W/m^3 , $8\text{x}10^6$ W/m^3 and $15\text{x}10^6$ W/m^3 were used.

Table 6.8 Thermophysical parameters used for blood, arterial wall, plaque and macrophage layer adapted from Duck 1990

Thermophysical Property	Macrophage Layer	Plaque	Arterial Wall	Blood
κ (W/m K)	0.484	0.484	0.476	0.549
ρ (kg/m^3)	920	920	1075	1050
C_p (J/kg K)	4080	4080	3490	4390
μ (Pa s)				0.0033

6.5.1 Effects of Fibrous Cap Thickness Φ_h, Macrophage Cell Density Φ_V and Heat Generation Rate q''' on the Temperature Profile of Plaque

The effect of the location of the macrophage layer and the cell density of the macrophage layer are shown in Figures 6.38-6.40 for different macrophage heat generation rate q'''. The temperature change variable ΔT is relative to the normal blood temperature. ΔT occurs due to the heat generating active cells in the macrophage layer. The value of ΔT increases as the fibrous cap thickness reduces (that is reducing value of Φ_h) as shown in Figure 6.38- 6.40 which is in agreement with experimental observations in both in-vivo and ex-vivo studies. The closeness of the macrophage layer to the arterial lumen surface increases the likelihood of detecting the vulnerable plaque using arterial wall thermography techniques. The maximum temperature ΔT increases proportionally with increasing macrophage cell density Φ_V and there is a wider spread of the temperature along the plaque as opposed to the narrow spread at lower macrophage content. Based on this observation, vulnerable plaques with higher macrophage content are more likely to be detected than macrophages with lower macrophage content. The macrophage cell density Φ_V was a more dominant factor on ΔT than the fibrous cap thickness Φ_h within the parameters chosen in the current study. The heat generation rate q''' of the macrophage layer has a proportional or increasing influence on ΔT as shown in Figures 6.38-6.40.

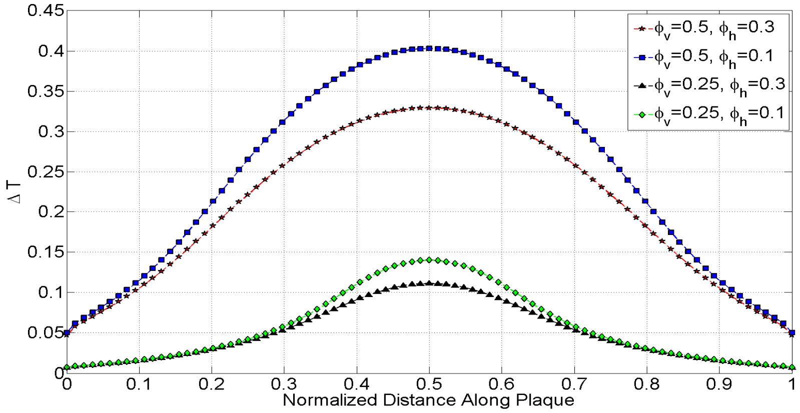

Figure 6.38 Temperature profile along the plaque for q''' =2x10^{6}W/m^3.

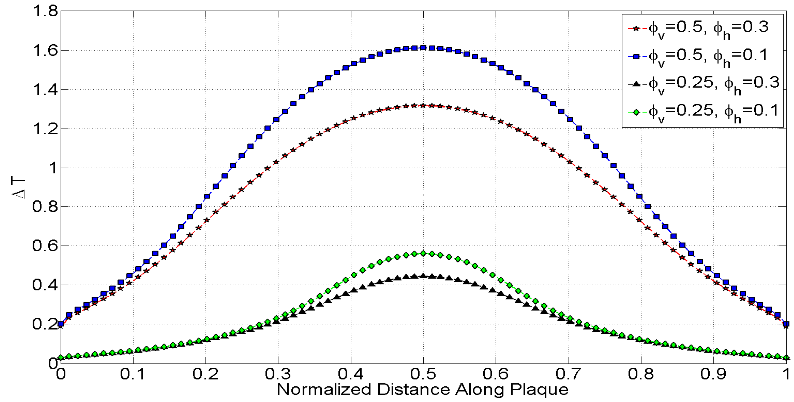

Figure 6.39 Temperature profile along the plaque for q''' =8x10^{6}W/m^3.

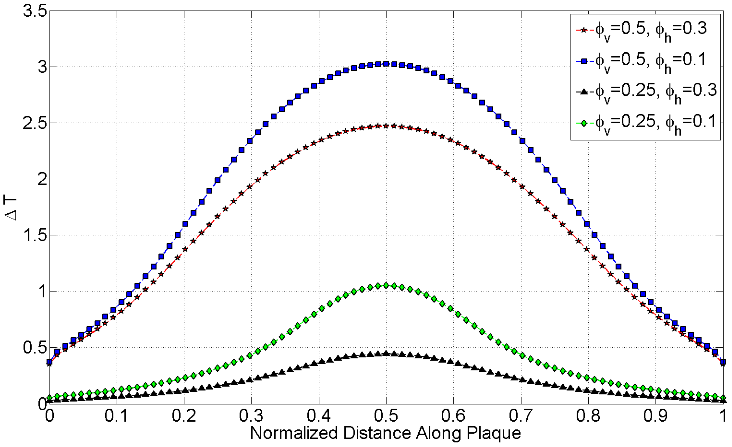

Figure 6.40 Temperature profile along the plaque for q''' =15x10^6W/m^3.

6.5.2 Effects of Re on the Temperature Profile of Plaque

The Reynolds number Re was increased from Re=100 to Re=200 to the impact of the cooling effect due to the blood flow. Two cases were considered, the first case is when the fibrous cap is thin with high macrophage content ($\Phi_V = 0.5, \Phi_h = 0.1$) and the second case is case with a low macrophage content that is deeper within the plaque ($\Phi_V = 0.5, \Phi_h = 0.1$). The effects of Re is shown in Figure 6.41. Increasing the Re number produces more cooling effect thereby lowering the temperature along the plaque as shown in Figure 6.41. The cooling effect makes detection of vulnerable plaque much difficult during in-vivo measurements. The cooling effect due to Re increase is not as severe to the temperature measurements when the fibrous cap is thin and also have a high macrophage content ($\Phi_V = 0.5, \Phi_h = 0.1$) due to already elevated temperatures at this condition. Cooling effects of the arterial wall temperature are more severe when the macrophage content is lower.

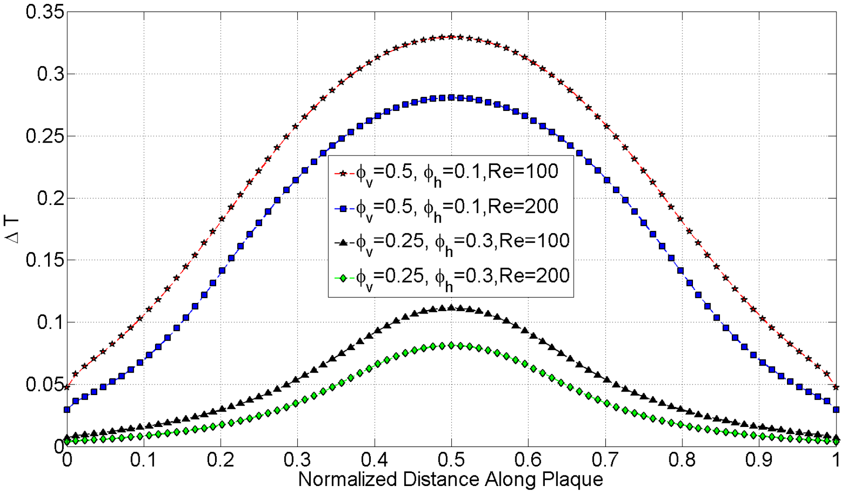

Figure 6.41 Effect of Re on the temperature profile along plaque for q''' =2x10^{6}W/m^3.

Based on these observations, balloon type catheter that temporarily interrupts blood flow during temperature measurements will be ideal for plaques that have lower macrophage content. The use of balloon type catheter will not be ideal for plaques with high macrophage content because obstruction of flow will result in much higher and elevated temperatures that might be detrimental to the arterial wall tissues.

6.5.3 Effects of Stenosis Degree Φ_S on the Temperature Profile of Plaque

The effect of stenosis was investigated by varying the parameter Φ_S in Eq. 6.21 while keeping the Re number the same. Previous results were evaluated with $\Phi_S = 0.25$ (that is 25% stenosis). In order to investigate the effect of stenosis on the temperature profile, the parameter Φ_S was reduced to a value of 0.125 (12.5% stenosis). Reducing the degree of stenosis from 25% to 12.5% causes a slight increase in the temperature ΔT as shown in a representative case in Figure 6.42. Majority of the temperature difference occurs at the normalized distance interval of between 0.4 to 0.6 as shown in Figure 6.42. This distance interval corresponds to the top region of the plaque as shown in Figure 6.43.

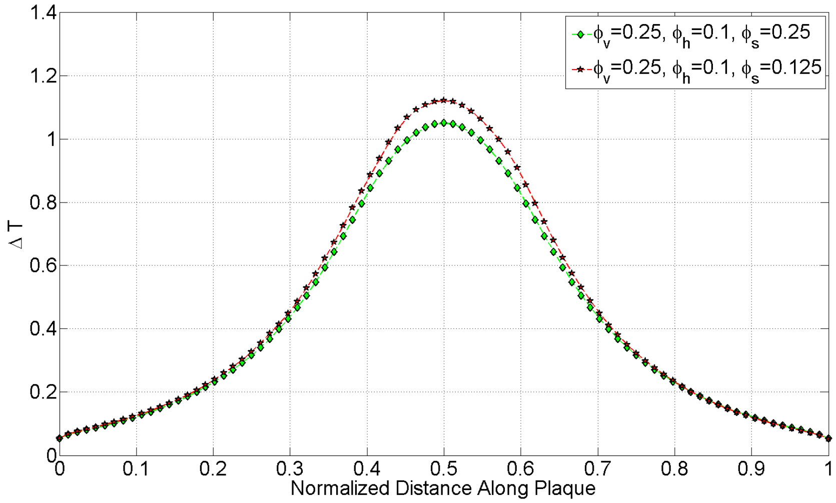

Figure 6.42 Effect of Φ_S on the temperature profile along plaque for q''' =15x10^{6}W/m^3.

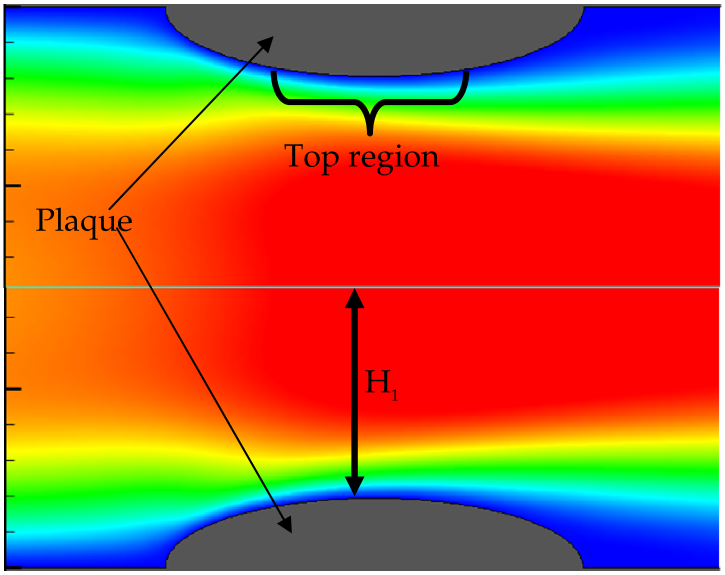

Figure 6.43 U velocity contour plot.

As the degree of stenosis increases (that is the distance H_1 reducing) there is an increase in velocity and velocity gradient at the throat formed by the upper and lower throat shown in Figure 6.43. The increase in velocity and velocity gradient at the throat reduces the boundary layer and enhances heat transfer at this location. The throat location coincides with the top region. The enhanced heat transfer at this location is responsible for the apparent slight reduction in the temperature at the top region for $\mathbf{\Phi}_S = 0.25$ when compared with the case of $\mathbf{\Phi}_S = 0.125$

CHAPTER 7

CONCLUSION AND FUTURE DIRECTIONS

In this thesis a new approach to handle thermal incompressible flows with immersed bodies within the lattice Boltzmann method (LBM) computational framework was developed and implemented. The new approach uses the immersed boundary method (IBM) to account for the presence of arbitrary or complex boundary shape within the Cartesian grid based LBM. The direct forcing variant of IBM was extended to handle heat transfer applications within LBM. The new approach is called direct forcing and heating immersed boundary lattice Boltzmann method (IB-LBM). A new implementation method for enforcing the constant heat flux boundary conditions and also in determining the local Nusselt number was introduced. The new implementation method for the constant heat flux (CHF) boundary condition is easier to implement when compared to existing thermal IBM implementation available in the literature because it eliminates the tracking or determination of the surface normal at each IBM Lagrangian point. The new implementation method also eliminates the computational step of interpolating for temperature at an interior point in the calculation of the surface temperature at the IBM Lagrangian node. The present method will be beneficial particularly for problems that contain deforming boundary, since the surface normal will change as the boundary deforms. A Multiphysics coupling scheme to couple multidomain and multiphysics problems between LBM and external solid domain solver was developed with emphasis on the conjugate heat transfer and fluid structure interaction problems.

The direct forcing and heating IB-LBM was implemented in a Fortran 90 code. The direct forcing and heating IB-LBM code was validated with classical benchmarks in four phases. The first phase validated the core LBM using classical fluid flow benchmarks such as the Couette flow (with and without slip boundary), Rayleigh flow, micro-Couette flow and lid driven cavity flow with slip boundary conditions. The ensuing velocity profile and vortex center location (for lid driven cavity) was compared with analytical or results from literature and good agreement were obtained both quantitatively and qualitatively. The second phase validated the direct forcing IB-LBM ability to enforce the no-slip boundary condition for immersed rigid or non deforming bodies. In the second phase, the direct forcing IB-LBM was validated with flow over bluff bodies such as circular cylinder and NACA 0012 airfoil. The drag and lift coefficients calculated by the direct forcing IB-LBM and Strouhal number (for cases with vortex shedding) were used for quantitative comparison with results from literature with good agreements obtained between current work and existing results. The third phase validated the proposed multiphysics interface coupling scheme between the external solid solver ABAQUS and the direct forcing IB-LBM for a fluid structure interaction (FSI) numerical benchmark. The FSI numerical benchmark was the flow over an idealized aortic heart valve leaflet. The periodic tip position was compared with results in literature for different Strouhal and Reynolds number. The last phase was used to validate the direct forcing and heating IB-LBM, the new method of enforcing CHF boundary condition and new method of calculating the local Nusselt number. The numerical benchmark test cases were for immersed bodies in forced and natural convection cases with either constant temperature or heat flux boundary condition. The temperature and local Nusselt number profile was used for qualitative comparison while the surface averaged Nusselt number was used for quantitative comparison with existing results in literature. There was good agreement both qualitatively and quantitatively with existing results thereby validating the accuracy of the direct forcing and heating IB-LBM and new proposed methods of enforcing the CHF boundary condition and local Nusselt number calculation.

The extensively validated direct forcing and heating IB-LBM with the multiphysics interface coupling scheme was applied to a conjugate heat transfer problem of arterial wall thermography in a straight artery with a vulnerable plaque. The effect of vulnerable plaque geometric parameters, blood flow Reynolds number, arterial wall stenosis and macrophage heat generation rate on the temperature profile on the surface of the plaque was investigated using the new approach. The plaque geometric parameters investigated were the fibrous cap thickness and macrophage cell density. The maximum temperature ΔT increases with decreasing fibrous cap thickness where ΔT is the temperature difference between the plaque surface temperature and the normal blood temperature. The clinical significance of this is that ΔT correlates with vulnerable plaque severity (reducing fibrous cap thickness) which is in good agreement with clinical observations in practice. The macrophage cell density and heat generation rate had the most pronounced or significant effect on the temperature ΔT. The pronounced impact of the macrophage heat generation rate on the temperature ΔT elucidates the significance of obtaining clinical relevant metabolic generation rate for the macrophages. The cooling effect of blood on the temperature ΔT was observed for increasing

Reynolds number. Despite the cooling effect of blood, plaques with high macrophage content have a high peak value of ΔT that can easily be detected by non flow interrupting catheter thermography techniques. Consequently the use of blood flow interruption techniques such as balloon type catheter will not be ideal for plaques with high macrophage content because obstruction of flow will result in much higher peak value of ΔT that might be deleterious to the plaque. Balloon type catheter will be ideal for plaques with moderate or low macrophage cell density. Increasing the degree of arterial lumen stenosis reduces the temperature ΔT slightly near the apex of the plaque due to increased velocity near the apex for increasing stenosis.

A future direction for the current research is to extend the direct forcing and heating IB-LBM to 3D. Extension of the direct forcing and heating IB-LBM to 3D will facilitate the ability to use patient specific arterial and plaque geometry that can be obtained using image reconstruction methods from methods such as MRI. The extension to 3D will increase the computational cost, the added cost can be alleviated or reduced by using more efficient code parallelization methods as opposed to the OpenMP method that is currently used. The current OpenMP parallelization method is limited to shared memory architecture and does not leverage the full advantage of the computational power available in a cluster computing environment. Another future direction is to parallelize the 3D direct forcing and heating IB-LBM using the message passing interface (MPI). MPI is ideal for cluster computing environment. Other future direction is to implement the already validated fluid/thermal/structure interaction coupling scheme to arterial wall thermography in order to evaluate the effects of wall elasticity and plaque deformation on the temperature profile.

BIBLIOGRAPHY

ABAQUS 6.8, (2008), Dassault Systèmes S.A

Abramowitz, M. and Stegun, I. A., (1972), "Handbook of mathematical functions with formulas, graphs, and mathematical Tables", 9th edition, Dover Publications, New York.

Alawi, A., Alshelkh-Ali, Kitsios, G.D., Balk, E.M., Lau, J., and Ip, S., (2010), "The Vulnerable atherosclerotic plaque: scope of the literature", Annals of Internal Medicine, Vol. 153, pp. 387-395.

Alexander, F.J., Chen, S., and Sterling, J.D., (1993), "Lattice Boltzmann thermohydrodynamics", Physical Review E, Vol. 47, pp. R2249-R2252.

Baaijens, F.P.T., (2001), "A fictitious domain/mortar element method for fluid–structure interaction", International Journal for Numerical Methods in Fluids, Vol. 35, pp. 743–761.

Bertrand, F., Tanguy, P. A. and Thibault, F., (1997),"A three-dimensional fictitious domain method for incompressible fluid flow problems", International Journal for Numerical Methods in Fluids, Vol. 25, pp. 719-736.

Bhatnagar, P.L., Gross, E. P. and Krook, M., (1954), "A model for collision processes in gases. Small amplitude processes in charged and neutral one-component systems", Physical Review, Vol. 94, pp. 511-525.

Casscells, W., Hathorn, B., David, M., (1996), "Thermal detection of cellular infiltrates in living atherosclerotic plaques: possible implications for plaque rupture and thrombosis", Lancet, Vol. 347, pp. 1447–1451.

Casscells, W., Naghavi, M. and Willerson, J. T., (2003), "Vulnerable atherosclerotic plaque: a multifocal disease", Circulation, Vol. 107, pp. 2072-2075.

Chapman, S. and Cowling, T.G. ,(1970), "The mathematical theory of non-uniform Gases", 3rd edition, Cambridge University Press, Cambridge.

Chen, S., and Doolen, G., (1998), "Lattice Boltzmann Method for fluid flows", Annual Review of Fluid Mechanics, Vol. 30, pp.329-364.

Chen, Y., Ohashi, H., and Akiyama, H., (1994), "Thermal lattice Bhatnagar–Gross–Krook model without nonlinear deviations in macrodynamic equations", Physical Review E, Vol. 50, pp. 2776-2783.

Chen, Y., Ohashi, H., and Akiyama, H., (1997), "Two-parameter thermal lattice BGK model with a controllable Prandtl number", Journal of Scientific Computing, Vol. 12, pp. 169-185.

Chuong, C.J. and Fung, Y.C., (1983), "Three-dimensional stress distribution in arteries", Journal of Biomechanical Engineering, Vol. 105, pp. 268–274.

Cuisset, T., Christophe, B., Narbeh, M., Melikian, M., Hamilos, Sarma, J.,Sarno, G., Naslund, M., Smith, L., Van de Vosse, F., Pijls, N.H., and De Bruyne, B., (2009), "In Vitro and In Vivo Studies on thermistor-based intracoronary temperature measurements: effect of pressure and flow", Catheterization and Cardiovascular Interventions, Vol. 73, pp. 224–230.

D'Orazio, A. and Succi, S., (2004),"Simulating two-dimensional thermal channel flows by means of a lattice Boltzmann method with new boundary conditions", Future Generation Computer Systems, Vol. 20, pp. 935 – 944.

De Hart, J., Peters, G.W.M., Schreurs, P.J.G., Baaijens, F.P.T., (2003), "A three-dimensional computational analysis of fluid–structure interaction in the aortic valve", Journal of Biomechanics, Vol. 36, pp. 103-112.

Delfino, A., Stergiopulos, N., Moore, J.E., and Meister, J.J., (1997), "Residual strain effects on the stress field in a thick wall finite element model of the human carotid bifurcation", Journal of Biomechanics, Vol. 30, pp. 777–786.

Dhiman, A., Chhabra, R. and Eswaran, V., (2005), "Flow and heat transfer across a confined square cylinder in the steady flow regime: Effect of Peclet number" International Journal of Heat and Mass Transfer, Vol. 48, pp. 4598-4614.

Duck, F.A., (1990), "Physical Properties of Tissue: A Comprehensive Reference Book", Academic Press, New York.

Ethier, C.R., (2002) "Computational modeling of mass transfer and links to atherosclerosis", Annals of Biomedical Engineering, Vol. 30, pp. 461–471.

Falk, E., Shah, P. K. and Fuster, V., (1995), "Coronary plaque disruption", Circulation, Vol.92, pp. 657-671.

Fu, Y.B. and Ogden, R.W., (2001), "Nonlinear elasticity theory and applications", London Mathematical Society Lecture Note Series 203, Cambridge University.

Fung, Y.C., Liu, S.Q. and Zhou, J.B., (1993), "Remodeling of the constitutive equation while a blood vessel remodels itself under stress", Journal of Biomechanical Engineering Vol. 115, pp. 453–459.

Gad-el-Hak, M., (1999), "The Fluid Mechanics of Microdevices", The Freeman scholar lecture, ASME Journal of Fluids Engineering, Vol. 121, pp. 5-33.

Gasser, T.C., Ogden, R.W. and Holzapfel, G.A., (2006), "Hyperelastic modeling of arterial layers with distributed collagen fibre orientations", Journal of the Royal Society Interface, Vol. 3, pp. 15–35.

Ge, L. and Sotiropoulos, F., (2007), "A numerical method for solving the 3D unsteady incompressible Navier-Stokes equations in curvilinear domains with complex immersed boundaries", Journal of Computational Physics, Vol. 225, pp. 1782–1809.

Gervaso, F., Capelli, C., Petrini, L., Lattanzio, P.S., Virgilio, L.D. and Migliavacca, F., (2008), "On the effects of different strategies in modeling ballon-expandable stenting by means of finite element method", Journal of Biomechanics, Vol. 41, pp. 1206-1212.

Glimm, J. and McBryan, O., (1985), "A Computational model for Interfaces", Advances in Applied Mathematics, Vol. 6, pp. 422-435.

Goldstein, D., Handler, R. and Sirovich, L., (1993), "Modeling a no-slip flow boundary with an external force field", Journal of Computational Physics, Vol. 105, pp.354-366.

Guo, Z., Zheng, C. and Shi, B., (2002), "Discrete lattice effects on the forcing term in the lattice Boltzmann method", Physical Review E, Vol. 65, pp. 046308-046316.

Harlow, F. and Amsden, F., (1970), "A Simplified MAC technique for incompressible fluid flow calculations", Journal of Computational Physics, Vol. 6, pp. 322-325.

He, X. and Luo, L. (1997). "Theory of the lattice Boltzmann method: from the Boltzmann equation to the lattice Boltzmann equation", Vol. 56, pp. 6811-6817.

He, X., Chen, S., and Doolen, G. D., (1998) "A novel thermal model for the lattice boltzmann method in incompressible limit", Journal of Computational Physics, Vol. 146, pp. 282-300.

Heijs, A. W. J. and Lowe, C. P., (1995), "Numerical evaluation of the permeability and the Kozeny constant for two types of porous media", Physical Review E, Vol. 51, pp. 4346-4352.

Heil, M., Walhorn, E. and Dinkler, D., (2004), "An efficient solver for the fully coupled solution of large-displacement fluid–structure interaction problems", Computer Methods in Applied Mechanics and Engineering, Vol. 193, pp. 1-23.

Hilber, H. M., Hughes, T. J. R. and Taylor, R. L., (1978), "Collocation, Dissipation and Overshoot for Time Integration Schemes in Structural Dynamics", Earthquake Engineering and Structural Dynamics, Vol. 6, pp. 99–117.

Hirt, C., and Nichols,B., (1981), "Volume of Fluid (VOF) Method for the Dynamics of Free Boundaries", Journal of Computational Physics, Vol. 39, pp. 201-225.

Hokanson, J. and Yazdani, S., (1997), "A constitutive model of the artery with damage", Mechanics Research Communications, Vol. 24, pp. 151–159.

Holzapfel, G.A. and Ogden, R.W., (2010), "Constitutive modeling of arteries", Proceedings of the Royal Society A, Vol. 466, pp. 1551-1597.

Horgan, C.O. and Saccomandi, G., (2003), "A description of arterial wall mechanics using limiting chain extensibility constitutive models", Biomechanics and Modeling in Mechanobiology, Vol. 1, pp. 251–266.

Hubner, B., Walhorn, E. and Dinkler, D., (2004), "A monolithic approach to fluid–structure interaction using space–time finite elements mechanical models of artery walls", Computer Methods in Applied Mechanics and Engineering, Vol. 193, pp. 2087-2104.

Jeong, H.K., Yoon, H.S., Ha, M.Y. and Tsutahara, M. (2010), "An immersed boundary-thermal lattice Boltzmann method using an equilibrium internal energy density approach for the simulation of flows with heat transfer", Vol. 229, pp. 2526-2543.

Kang, S.K. and Hassan, Y.A., (2011), "A direct-forcing immersed boundary method for the thermal lattice Boltzmann method", Computers & Fluids, Vol. 49, pp. 36-45.

Kalita, P., and Schaefer, R., (2008), "Mechanical models of artery walls", Archives of Computational Methods in Engineering, Vol. 15, pp. 1-36.

Khakpour, M., and Vafai, K., (2008), "Critical assessment of arterial transport models", International Journal of Heat and Mass Transfer, Vol. 51, pp. 807-822.

Kim, B.S., Lee, D.S., Ha, M.Y. and Yoon, H.S., (2007), "A numerical study of natural convection in a square enclosure with a circular cylinder at different vertical locations", International Journal of Heat and Mass Transfer, Vol. 51, pp. 1888-1898.

Kim, J. and Choi, H., (2004), “An Immersed-Boundary Finite-Volume Method for Simulation of Heat Transfer in Complex Geometries”. KSME International Journal, Vol. 18, pp. 1026-1035.

Kolodgie, F.D., Virmani, R., Burke, A.P., Farb, A., Weber, D.K., Kutys, R., (2004), “Pathologic assessment of the vulnerable human coronary plaque”, Heart, Vol. 90, pp. 1385-1391.

Kuksenok O., Yeomans, J.M. and Balazs, A.C., (2002), “ Using patterned substrates to promote mixing in microchannels”, Physical Review E, Vol. 65, pp. 031502-031509.

Leveque, R.J. and Li, Z., (1994), “The immersed interface method for elliptic equations with discontinuous coefficients and singular sources”, SIAM Journal of Numerical. Analysis, Vol. 31, pp.1019

Lim, C.Y., Shu, C., Niu, X.D. and Chew, Y.T., (2002), “Application of lattice Boltzmann method to simulate microchannel flows”, Physics of Fluids, Vol. 14, pp. 2299–2308.

Liou, W.W and Fang, Y., (2006), “Microfluid mechanics: principles and modeling”, McGraw Hill Nanoscience and Technology Series.

Liou, W.W and Bamiro, O.O., (2008), “Non continuous approaches”, Encyclopedia of Micro- and Nanofluidics, Springer-Verlag, New York.

Liu, W.K., Liu, Y., Farrell, D., Zhang, L.T., Wang, S., Fukui, Y., Patankar, N., Zhang, Y., Bajaj, C., Lee, J., Hong, J., Chen, X. and Hsu, H., (2006). “Immersed finite element method and its applications to biological systems”, Computer Methods in Applied Mechanics and Engineering, Vol. 195, pp. 1722–1749.

Lockard, D.P., Luo, L.S., Milder, S.D. and Singer, B.A., (2002) “Evaluation of power flow for aerodynamic applications” Journal of Statistical Physics, Vol. 107, pp. 423–478.

Mai, H.C., Lin, K.H., Yang, C.H. and Lin, C.A, (2010) “A thermal lattice Boltzmann model for flows with viscous heat dissipation”, Computer Modeling in Engineering and Sciences, Vol. 16, pp. 45-60.

Martys, N. S. and Chen, H., (1996), “Simulation of multicomponent fluids in complex three- dimensional geometries by the lattice Boltzmann method”, Physical Review E, Vol. 53, pp. 743-750.

McNamara, G. and Alder, B., (1993), “Analysis of the lattice Boltzmann treatment of hydrodynamics”, Physica A, Vol. 194, pp. 218-228.

McNamara, G., Garcia, A., and Alder, B., (1995), "Stabilization of thermal lattice boltzmann models", Journal of Statistical Physics, Vol. 81, pp. 395-408.

McNamara, G., Garcia, A., and Alder, B., (1997) "A hydrodynamically correct thermal lattice boltzmann model", Journal of Statistical Physics, Vol. 87, pp. 1111-1121.

McNamara, G. and Zanetti, G., (1988), "Use of the Boltzmann equation to simulate lattice-gas automata", Physical Review Letters, Vol. 61, pp. 2332–2335.

Mittal, R. and Iaccarino, G., (2005), "Immersed boundary methods", Annual Review of Fluid Mechanics, Vol. 37, pp. 239-261.

Mohd-Yusof, J., (1997), "Combined immersed-boundary/B-spline methods for simulations of flow in complex geometries", Annual Research Briefs, Center for Turbulence Research, NASA/AMES Stanford University, pp. 317–327.

Moukalled, F. and Acharya, S., (1996), "Natural convection in the annulus between concentric horizontal circular and square cylinders", Journal of Thermophysics Heat Transfer, Vol. 10, pp. 524

Muller, J.E, Tofler, G.H, Stone, P.H., (1989), "Circadian variation and triggers of onset of acute cardiovascular disease", Circulation, Vol. 79, pp. 733-743.

Nagano, N., Sugiyama, K., Takeuchi, S., Satoshi, Takagi, S. and Matsumoto,Y., (2010), "Full-Eulerian Finite-Difference Simulation of Fluid Flow in Hyperelastic Wavy Channel", Journal of Fluid Science and Technology, Vol. 5, No. 3, pp. 475-490.

Naghavi, M., Madjid, M., Gul, K., Siadaty, M.S., Litovsky, S., Willerson, J.T. and Casscells, S.W., (2003), "Thermography basket catheter: In vivo measurement of the temperature of atherosclerotic plaques for detection of vulnerable plaques", Catheterization and Cardiovascular Interventions, Vol. 59, pp. 52–59.

Naqvi, T.Z., Hachamovitch, R., Berman, D., Buchbinder, N., Kiat, H. and Shah, P.K., (1997), "Does the presence and site of myocardial ischemia on perfusion scintigraphy predict the occurrence and site of future myocardial infarction in patients with stable coronary artery disease?", American Journal of Cardiology, Vol. 79, pp.521-524.

Narula, J., Garg, P., Achenbach, S., Motoyama, S., Virmani, R. and Strauss, H.W., (2008), "Arithmetic of vulnerable plaques for noninvasive imaging", Nature Reviews Cardiology, Vol. 5, pp. S2-S10.

Nemirovsky, D., (2003),"Imaging of high-risk plaque", Cardiology, Vol. 100, pp. 160–175, Oran, E.S., Oh,C.K., and Cybyk, B.Z., (1998), "Direct Simulation Monte Carlo: Recent advances and applications", Annual Review of Fluid Mechanics, Vol. 30, pp.403-441.

Panton, R.L., (2005), "Incompressible fluid flow", John Willey and Sons.

Peng, Y., Shu, C., and Chew, Y. T., (2003), "Simplified thermal lattice Boltzmann model for incompressible thermal flows", Physical Review E, Vol. 68, pp. 026701.

Peng, Y., Chew, Y.T. and Shu, C., (2003), "Numerical simulation of natural convection in a concentric annulus between a square outer cylinder and a circular inner cylinder using the Taylor-series-expansion and least-squares-based lattice Boltzmann method", Physical Review E, Vol. 67, pp. 026701.

Peskin, C.S., (1972), "Flow patterns around heart valves: a numerical method", Journal of Computational Physics, Vol. 10, pp. 252-271.

Peskin, C.S., (1977), "Numerical analysis of blood flow in the heart", Journal of Computational Physics, Vol. 25, pp. 221-249.

Peskin, C.S., (2002), "The immersed boundary method", Acta Numerica, Vol. 11, pp. 479-517.

Peskin, C.S. and Kim, Y., (2007), "Penalty immersed boundary method for an elastic boundary with mass", Physics of Fluids, Vol. 19, pp. 053103-1-18.

Qian, Y. H., d'Humieres, D. and Lallemand, P., (1992), "Lattice BGK models for Navier-Stokes equation", Europhysics Letters, Vol. 17, pp. 479–484.

Raiskinmäki, P., Koponen, A., Merikoski, J. and Timonen, J., (2000), "Spreading dynamics of three-dimensional droplets by the lattice-Boltzmann method", Computational Materials Science, Vol. 18, pp. 7-12.

Saiki, E.M. and Biringen, S., (1996), "Numerical simulation of a cylinder in uniform flow: application of a virtual boundary method", Journal of Computational Physics, Vol. 123, pp. 450-465.

Schelkle, M. and Frohn, A., (1995), "Three-dimensional lattice Boltzmann simulations of binary collisions between equal droplets", Journal of Aerosol Science, Vol. 26, pp. 145-146.

Sethian, J.A., (1996), "A Review of the Theory, Algorithms, and Applications of Level Set Methods for Propagating Interfaces", Acta Numerica, Vol. 5, pp. 309-395.

Sethian, J.A. and Osher, S., (1988), "Fronts Propagating with Curvature-Dependent Speed: Algorithms Based on the Hamilton-Jacobi Formulation", Journal of Computational Physics, Vol. 79, pp. 12-49.

Shan, X., (1997), "Simulation of Rayleigh-Benard convection using a lattice Boltzmann Method", Physical Review E, Vol. 55, pp. 2780-2788.

Shan, X. and Chen, H., (1993), "Lattice Boltzmann model for simulating flows with multiple phases and components", Physical Review E, Vol. 47, pp. 1815-1820.

Shu, C. and Zhu, Y., (2002), "Efficient computation of natural convection in a concentric annulus between an outer square cylinder and an inner circular cylinder", International Journal of Numerical Methods in Fluids, Vol. 38, pp. 429-439.

Solomon E.P, Schmidt R,, and Ardragna, P., (1990), "Human anatomy and physiology", Saunders College Publishing, Philadelphia.

Spaid, M.A.A. and Phelan F.R. Jr., (1997), "Lattice Boltzmann methods for modeling microscale flow in fibrous porous media", Physics of Fluids, Vol. 9, pp. 2468–2474.

Srikanth, S., Dhiman, A.K. and Bijjam, S., (2010), "Confined flow and heat transfer across a triangular cylinder in a channel", International Journal of Thermal Sciences, Vol. 49, pp. 2191-2200.

Stary, H.C., Chandler, A.B., Dinsmore, R.E., Fuster, V., Glagov, S., Insull, W., Rosenfield, M. E., Schwartz, C. J., Wagner, W. D. and Wissler, R.W., (1995), "A definition of advanced types of atherosclerotic lesions and a histological classification of atherosclerosis : a report from the committee on vascular lesions of the council on arteriosclerosis, American Heart Association", Circulation, Vol. 95, pp. 1355-1374.

Stefanadis, C., Diamantopoulos, L., Vlachopoulos, C., Tsiamis, E., Dernellis, J., Toutouzas, K., Stefanadi, E. and Toutouzas, P., (1999)," Thermal heterogeneity within human atherosclerotic coronary arteries detected in vivo: a new method of detection by application of a special thermography catheter", Circulation, Vol. 99, pp:1965–1971.

Stefanadis, C., Toutouzas, K., Tsiamis, E., Stratos, C., Vavuranakis, M., Kallikazaros, I., Panagiotakos, D. and Toutouzas, P., (2001), " Increased local temperature in human coronary atherosclerotic plaques: an independent predictor of clinical outcome in patients undergoing a percutaneous coronary intervention", Journal of American College of Cardiology, Vol. 37, pp. 1277–1283.

Stefanadis, C., Toutouzas, K., Vavuranakis, M., Tsiamis, E., Vaina, S. and Toutouzas, P., (2003), "New balloon-thermography catheter for in vivo temperature measurements in human coronary atherosclerotic plaques: A novel approach for thermography?", Catheterization and Cardiovascular Interventions, Vol. 58, pp. 344–350.

Succi, S., (2001), "The lattice Boltzmann equation for fluid dynamics and beyond", Numerical Mathematics and Scientific Computation. Oxford University Press Inc., Oxford.

Succi, S. and Sbragaglia, M., (2005), "Analytical calculation of slip flow in lattice boltzmann models with kinetic boundary conditions", Physics of Fluids, Vol. 17, pp. 093602-1- 093602-8.

Suppa, D., Kuksenok, O., Balazs, A. C. and Yeomans, J. M., (2002), "Phase separation of a binary fluid in the presence of immobile particles: A lattice Boltzmann approach", Journal of Chemical Physics, Vol. 116, pp. 6305-6310.

Succi, S., Foti, E. and Higuera F., (1989), "Simulation of three-dimensional flows in porous media with the lattice Boltzmann method", Europhysics Letters., Vol. 10, pp. 433-440.

Swift, M.R., Orlandini, S.E., Osborn, W.R., and Yeomans, J.M., (1996), "Lattice Boltzmann simulations of liquid-gas binary-fluid systems", Physical Review E, Vol. 54, pp. 5041-5052.

Taber, L., (2004), "Nonlinear theory of elasticity applications in biomechanics", 1st edition, World Scientific Publishing, Singapore.

Takamizawa, K. and Hayashi, K., (1987), "Strain energy density function and uniform strain hypothesis for arterial mechanics", Journal of Biomechanics, Vol. 20, pp. 7–17.

Tang, G.H., Tao, W.Q., and He, Y.L., (2005), "Lattice Boltzmann method for gaseous microflows using kinetic boundary conditions", Physics of Fluids. Vol. 17, pp. 058101-058104.

Teixeira, C., Chen, H. and Freed, D., (2000), "Multi-speed thermal lattice Boltzmann method stabilization via equilibrium under-relaxation", Computer Physics Communications. Vol. 129, pp. 207–226.

Thamida, S.K. and Chang H.C., (2002), "Nonlinear electrokinetic ejection and entrainment due to polarization at nearly insulated wedges", Physics of Fluids, Vol. 14, pp. 4315–28.

Toutouzas, K., Drakopoulou, M., Synetos, A. and Stefanadis, C., (2010), "Intravascular thermography for assessing vulnerable plaques", Current Cardiovascular Imaging Report, Vol. 3, pp. 207-210.

Turek, S. and Schafer, M., (1996), "Benchmark Computations of Laminar Flow Around a Cylinder", Flow Simulation With High-Performance Computers II, Vol. 52 of Notes on Numerical Fluid Dynamics, pp. 546-566.

Udaykumar, H.S., Mittal, R., Rampunggoon, P. and Khanna, A., (2001) "A sharp interface Cartesian grid method for simulating flows with complex moving boundaries", Journal of Computational Physics, Vol. 174, pp. 345–380.

Van de Vosse, F., Hart, J. D., Oijen, C. V., Bessems, D., Gunther, T., Segal, A., Wolters, B., Stijnen, J., and Baaijens, F., (2003), "Finite-element-based computational methods for cardiovascular fluid-structure interaction", Journal of Engineering Mathematics, Vol. 47, pp.335–368

Virmani, R., Burke, A.P., Farb, A. and Kolodgie, F.D., (2006), "Pathology of the vulnerable plaque", Journal of American Cardiology, Vol. 47, pp. C13-C18.

Rosamond, W., Flegal, K., Furie, K., Go, A., Greenlund, K., Haase, N., Hailpern, S. M., Ho, M., Howard, V., Kissela, B., Kittner, S., Lloyd□Jones, D., McDermott, M., Meigs, J., Moy, C., Nichol, G., O'Donnell, C., Roger, V., Sorlie, J., Steinberger, J., Thom, T., Wilson, M., and Hong, Y., "Heart disease and stroke statistics 2008 update. A report

from the American Heart Association statistics committee and stroke Statistics subcommittee," Circulation, Dec 17 2007

Wang, X. and Liu, W.K., (2004) "Extended immersed boundary method using FEM and RKPM", Computer Methods in Applied Mechanics and Engineering, Vol.193, pp. 1305-1321.

World Health Organization, (2006), "World Health Statistics 2006"

Xi, H.W. and Duncan, C., (1999), "Lattice Boltzmann simulations of three-dimensional single droplet deformation and breakup under simple shear flow", Physical Review E, Vol. 59, pp. 3022–3026.

Yoon, H. S., Lee, J. B., Seo, J. H., and Park, H. S., (2010), "Characteristics for flow and heat transfer around a circular cylinder near a moving wall in wide range of low Reynolds number", International Journal of Heat and Mass Transfer, Vol. 53, pp. 5111-5120.

Yu, D., Mei, R., Luo, L.S. and Shyy,W., (2003), "Viscous flow computations with the method of lattice Boltzmann equation", Progress in Aerospace Sciences, Vol. 39, pp. 329-327.

Yu, D., Mei, R. and Shyy,W., (2002), "A multi-block lattice Boltzmann method for viscous fluid flows", International Journal of Numerical Methods in Fluids, Vol. 39, pp. 99-120.

Yu, Z., (2005), "A DLM/FD method for fluid/flexible-body interactions", Journal of Computational Physics, Vol. 207, pp. 1–27.

Zhang, L.T. and Gay, M., (2007), " Immersed finite element method for fluid-structure interactions", Journal of Fluids and Structures, Vol. 23, pp. 839-857

Zhang, Y., Qin, R. and Emerson, D.R., (2005), "Lattice Boltzmann simulation of rarefied gas flows in microchannels", Physical Review E, Vol. 71, pp. 047702-1 - 047702-4.

Zou, Q., and He, X., (1997), "On pressure and velocity boundary conditions for the lattice Boltzmann BGK model", Physics of Fluids, Vol. 9, pp. 1591-1598.

Zunino, P., D'Angelo, C., Petrini, L., Vergara, C., Capelli, C. and Migliavacca, F., (2009), "Numerical simulation of drug eluting coronary stents: Mechanics, fluid dynamics and drug release", Computer Methods in Applied Mechanics and Engineering,Vol. 198, pp. 3633-3644.